Theses and dissertations

1-1-2012

Biomechanical Evaluation of a Carbon Fibre Epoxy Composite Plate in an Injured and Healed Femur Using Infrared Thermography and Finite Element Analysis

Faisal Sharaf Siddiqui
Ryerson University

Follow this and additional works at: http://digitalcommons.ryerson.ca/dissertations

Part of the Biomechanical Engineering Commons

**BIOMECHANICAL EVALUATION OF A CARBON FIBRE EPOXY COMPOSITE
PLATE IN AN INJURED AND HEALED FEMUR USING INFRARED
THERMOGRAPHY AND FINITE ELEMENT ANALYSIS**

by

Faisal Sharaf Siddiqui

B.E. (Mechanical Engineering)

Mehran University of Engineering & Technology, Jamshoro, Pakistan

A thesis

presented to Ryerson University

in partial fulfillment of the

requirements for the degree of

Master of Applied Science

in the Program of

Mechanical Engineering

Toronto, Ontario, Canada, 2012

AUTHOR'S DECLARATION FOR ELECTRONIC SUBMISSION OF A THESIS

I hereby declare that I am the sole author of this thesis. This is a true copy of the thesis, including any required final revisions, as accepted by my examiners.

I authorize Ryerson University to lend this thesis to other institutions or individuals for the purpose of scholarly research.

I further authorize Ryerson University to reproduce this thesis by photocopying or by other means, in total or in part, at the request of other institutions or individuals for the purpose of scholarly research.

I understand that my thesis may be made electronically available to the public.

Acknowledgements

I am highly indebted to my colleagues, friends and instructors who provided me all the help I needed to complete this thesis.

First, I wish to express my deep sense of gratitude to my supervisor Dr. Habiba Bougherara for her guidance and support throughout this effort and the honour given to me to work on this project. In addition, Dr. Habiba Bougherara must be credited for sparking my interest in research and also has been a wonderful influence on my career. I am thankful for her much-needed encouragement that helped me see this thesis through.

Dr. Rad Zdero, for his invaluable technical knowledge and expertise in the field of biomechanics, as well as his guidance and knowledge during the laboratory phase of this study and the use of the laboratory at St. Michael's Hospital, Toronto.

Mr. Suraj Shah, M.A.Sc., provided his precious time and expertise in experimental work of infrared thermography. His cooperation and guidance was necessary to this study which would be not possible otherwise. Mr. Suraj Shah provided me with useful input that enriched my understanding and enthusiasm on the field.

I am grateful to Ms. Mimi Lam and the School of Graduate Studies at Ryerson University, for their assistance throughout the course of my post-graduate studies.

Last, but certainly not least, I recognize my parents and wife for their selfless and absolute support in good times and bad.

Abstract

BIOMECHANICAL EVALUATION OF A CARBON FIBRE EPOXY COMPOSITE PLATE IN AN INJURED AND HEALED FEMUR USING INFRARED THERMOGRAPHY AND FINITE ELEMENT ANALYSIS

Master of Applied Science, 2012

Faisal Sharaf Siddiqui,

Mechanical Engineering,

Ryerson University

Femur fractures are caused by high energy trauma or by musculoskeletal impairments, such as osteoporosis. The presence of total hip replacement (THR) superior to a femoral mid-shaft fracture greatly complicates fixation and treatment. The most conventional fracture fixation method is internal fixation by metal plate and screws. However, metal being stiffer than bone, causes stress shielding and bone resorption. The goal of this study was to evaluate the performance of a less stiff carbon fibre epoxy plate as fracture fixation in an injured and healed femur. IR thermography validated by finite element analysis (FEA) was used to investigate the stress patterns of an injured and healed femur under an average cyclic loading of 800 N at an adduction angle of 7 degrees to simulate the single-legged stance phase of walking. The average stiffness of an injured femur with carbon/epoxy plate was 532.1 N/mm (static) and 625.3 N/mm (dynamic) respectively, that increased to 597.6 N/mm (static) and 697.9 N/mm (dynamic) for the metal plate. For the healed femur, the average stiffness increased from 1660.3 N/mm (static) and 2010.0 N/mm (dynamic) for the carbon/epoxy plate to 1704.4 N/mm (static) and 2070.4 N/mm (dynamic) for the metal plate. IR stress maps for carbon/epoxy and metal plate (injured femur) showed an overall difference of 29.2% for the anterior and posterior sides. This is the first study to assess experimentally and computationally the biomechanical behavior of injured and healed synthetic femur with two different plates construct.

Table of Contents

List of Figures

List of Tables

Units Used

MPa	Mega Pascal
GPa	Giga Pascal
g/m^3	Surface density
W/mK	Thermal conductivity
kg	Kilogram
kW	Kilowatt
N	Newton
g/cm^3	Density
Hz	Hertz (One cycle per second)

Commonly used Terminology

Abduction   moving of a body part away from the central axis of the body

Acetabulum   the cup-shaped cavity on the lateral surface of the hip bone, receiving the head of the femur

Adduction   moving of a body part toward the central axis of the body

Anterior   towards the front of the body

Arthroplasty   the surgical repair of a joint or the fashioning of a movable joint, using the patient's own tissue or an artificial replacement

Biocompatibility   the property of being biologically compatible by not producing a toxic, injurious, or immunological response in living tissue

Cancellous bone   sponge bone tissue contained in inner space of bone

Condyle   a rounded prominence at the end of a bone, most often for articulation with another bone

Contralateral   taking place or originating in a corresponding part on an opposite side

Cortical bone   the compact bone of the shaft of a bone that surrounds the marrow cavity

Diaphysis   the shaft of a long bone, between the epiphyses

Distal   situated farthest from the centre, median line, or point of attachment or origin

Epiphysis   the expanded articular end of a long bone, developed from a secondary ossification center, which during the period of growth is either entirely cartilaginous or is separated from the shaft by a cartilaginous disk

Femur   the longest thickest bone of the human skeleton, articulating with the pelvis above and the knee below

Intercondylar   between two condyles

Lateral   situated or extending away from the median plane of the body

Medial   situated toward the median plane or midline of the body or a structure

Metaphysis   the wider part at the end of a long bone, adjacent to the epiphyseal disk

Osteopenia	reduced bone mass due to a decrease in the rate of osteoid synthesis to a level insufficient to compensate for normal bone lysis
Osteoporosis	A disease characterized by decrease in bone mass and density
Patella	a triangular bone, about 5 cm in diameter, situated at the front of the knee in the tendon of insertion of the quadriceps muscle. Called also knee cap.
Physiologic	relating to the way that living things function, rather than to their shape or structure
Posterior	towards the rear of the body
Prosthesis	an artificial substitute for a missing body part, such as an arm, leg, eye, or tooth; used for functional or cosmetic reasons or both
Proximal	nearest to a point of reference, as to a center or median line or to the point of attachment or origin
Resorption	the loss of substance or bone by physiologic or pathologic means, such as the reduction of the volume and size of the residual ridge of the mandible or maxillae
Sagittal	situated in the direction of the sagittal suture; said of an anteroposterior plane or section parallel to the median plane of the body
Supracondylar	above a condyle
Trochanter	a broad, flat process on the femur, at the upper end of its lateral surface, or a short conical process on the posterior border of the base of its neck

List of Abbreviations

BW   Body Weight

FEA   Finite Element Analysis

IR   Infrared

IRT   Infrared Thermography

TSA   Thermoelastic Stress Analysis

CHAPTER 1. INTRODUCTION

1.1   Background Motivation

In orthopaedic trauma, femur fractures are an important subject of investigation, because femurs are the strongest, longest and heaviest bone in the human body. In young people, injury to normal healthy femurs can be caused by high-energy incidents, such as the 5500,000 accidents, occurring yearly in the United States [1]. It can also be fractured by a low energy force applied to an elderly person, suffering from musculoskeletal impairments, such as osteoporosis or osteopenia [2]. Osteoporosis is a type of bone disease, related with age and characterized by the loss of bone due to aging. It is often called as *silent disease,* because of its symptomless development, until a fracture occurs. Bones are easier to fracture, even from simple routine activities or fall from low heights. Regardless of the causes, symptoms of fracture are very serious leading to severe pain and inability to move leg [2]. The impact of femoral fractures is not only severe long term pain, but also it could impact quality of life, like inability to perform daily routine activities, immobility, economic burden of inpatient, outpatient and long term care expenses, indirect costs related with morbidity and mortality [3].

Osteoporosis, often considered as a disease of women, however, has been recently found to affect men as well. According to the National Osteoporosis Foundation, in United States, approximately 29.5 million women and 11.7 million men were suffering from osteoporosis. By 2020, in total, it may increase to 61 million, if effective treatments are not found widely or implemented [3, 4]. Osteoporosis also results in hip and knee implants replacement, the most common joint replacements conducted worldwide, and the number of primary surgeries continues to increase with every year. According to Canadian institute for health information, between 1996-97 and 2006-2007, in Canada, hip and knee replacements increased from 59% to 140%, respectively [5, 6].

A fractured femur normally takes about 3 to 6 months to heal; however, the process of healing begins as early as 6 weeks. Such a long healing time, may result in misalignment. Therefore the femur fracture requires an aid to enhance its healing process and to provide proper alignment. Treatment of femur fractures gets complicated in the presence of a pre-existence total hip replacement (THR). Periprosthetic femoral fractures usually occur in estimated 0.1% to 6% of all patients, mostly occurring in elderly women with osteopenia or in patients with loosened hip stem [7, 8]. Patients with periprosthetic fractures are associated with most complications, such as,

nonunion in 25% to 42% of all such fractures treated non-operatively, therefore treatment of such fractures are still a point of controversy [7, 8]. Though there is no "gold standard" approach, the most frequently used extramedullary strategy involves placing of a metal plate across the fracture line on the lateral femur surface, with proximal fixation with cables/screws and distal fixation with bicortical screws [9].

Bone plate fixation is one of the methods for treating femoral fractures. The major benefit of this method is that it can be used for the patients with hip or knee implants. The other benefits include, that it can be used when the bone has been fragmented at the site of fracture, the chances of shortening of the injured femur are smaller compared to other methods [9, 10] and this method does not require reaming or cutting of the epiphyses and nearby growth plates. This is particularly advantageous in pediatric patients [11].

Most of the commercially available bone plates are made of metallic materials such as titanium, titanium alloys, cobalt alloys or stainless steel [12]. An advantage of using metal alloys in biological applications is that, they have been extensively studied and therefore their mechanical properties and bio-compatibility have been well documented.

Practical experience, however, has revealed that metallic bone fixation devices do not adequately match the stiffness properties of human bones. In fact, the elastic modulus of metal is about 7 to 12 times higher than that for human bones. The high rigidity of metal plates can result in an unbalanced load distribution between the bone and implants with the bone plate carrying most of the load. This phenomenon is called *stress shielding* or stress protection [12].

Stress shielding can cause the compressive stresses in the affected bone to be about 28-45% lower than they were pre-operatively [13]. Since compressive stress is required to maintain healthy bone density, stress-shielding often results in a lower bone density and higher porosity compared to the pre-operative bone. The weakened bone suffers an increased risk of re-fracture once the bone plate implant is removed [14, 15]. In one study, about 3% of patients re-fractured their femurs after the bone plate was removed following a visible re-union of the injured femur [16]. This carries a high societal cost both in terms of burdening the healthcare system as well as pain and suffering caused to the patient. Bone fixation methods must be mindfully selected in order to minimize the risk of re-fracture by optimizing the compressive stresses transferred to the femur in order to maintain healthy bone density.

In order to reduce stress shielding, an ideal situation is to reduce stiffness of plates while maintaining their structural strength. But other than stiffness, factors like material selection and strength are also to be considered in bone plate design. Strength of a plate depends on the cross section and material properties. The thicker the plate the stronger it will be, however, an overly thick plate is unreasonable for human body. High stiffness is required in the initial healing process of the fracture to provide stability. However, towards the end of the healing process less stiffness is required from the plate in order for the bone to absorb some physiological stress allowing it to strengthen and prevent re-fracture [10].

Orthopaedic pioneering researchers and surgeons have encouraged material scientists and engineers for many years to develop implants and devices to cure diseases and injuries involving the skeleton. The surgical technique to relieve the pain and to restore the function by creating an artificial joint is known as replacement.

The biocompatibility and low rigidity of carbon fibre reinforced composite is comparable to that of cortical bone, which makes it a candidate material for use in orthopaedic applications. For total hip replacement and internal fixation, Christel *et al.* suggested these composites and polymers as candidate biomaterials [17, 18].

1.2 Current Thesis Outline

The thesis is comprised of six main chapters. This manuscript provides the motivation behind the need for this study and research goals this thesis sets out to accomplish.

Chapter 2 provides a comprehensive literature review consisting of introduction to the anatomy of the human limb, clinical aspects of femur fracture, biomechanics, biomechanical aspects of femur fracture, thermography, finite element analysis and the role thermography and finite element analysis plays in current research.

Chapter 3 explains the methodology of the current study. Specifically, it describes each component, the specimen preparation process, mechanical tests and infrared thermography conducted in the experiment. It also describes the development of the finite element model.

Chapter 4 provides the results from the experimental investigation and the finite element study. Chapter 5 critically analyzes the results, and discusses the limitations of the study. This chapter also provides direction for future work.

Chapter 6 concludes with the summary, highlighting the biomechanical evaluation of carbon/epoxy composite laminate as a material for bone plate.

1.3   Research Question and Goals

The aim of this study was the biomechanical evaluation of carbon/epoxy plate as a fracture fixation method to reduce stress shielding and bone resorption in the presence of hip stem. The investigation was carried out using large left synthetic femurs, with two different constructs, one using titanium as material for bone plate and the other using carbon/epoxy composite laminate, undergoing dynamic axial conditions, to examine the biomechanics of surgical repair method for femoral shaft fracture in the presence of total hip replacement, which is a real-world challenge for clinical management.

By showing the viability of using infrared thermography as an alternative to strain gauge measurements, this will allow a better understanding of the stress patterns along the surface of the bone and, in the long term, assist in improving current orthopaedic implants to speed up patient recovery times.

The finite element model of the periprosthetic femurs with bone plate combinations was designed and developed to predict stiffness and stress patterns for 4 different constructs. Studies have revealed that, finite element analysis is a useful tool for implant design purposes, particularly for determining load sharing between implant and bone [19-24].

No study to date has systematically tracked the changes, and compared two different fixation methods in the femur for the stiffness and stress that occur starting from an intact femur, to initial total hip replacement, to surgical fracture repair using a plate, and then to complete fracture healing for a periprosthetic femur fracture.

CHAPTER 2. LITERATURE REVIEW

2.1   Co-ordinate planes of the Human body

The human body can be described into three major planes, which run through the body, and are used to specify the orientation and position of parts of the body, as shown in Figure 2.1. The *sagittal plane* divides the human body longitudinally into right and left halves. The *coronal plane,* or the *frontal plane,* passes through the body from head to the feet, and divides the body into anterior and posterior sections. The *transverse plane,* alternatively called the *axial plane,* runs through the body longitudinally, and divides the body into superior and inferior halves [25, 26].
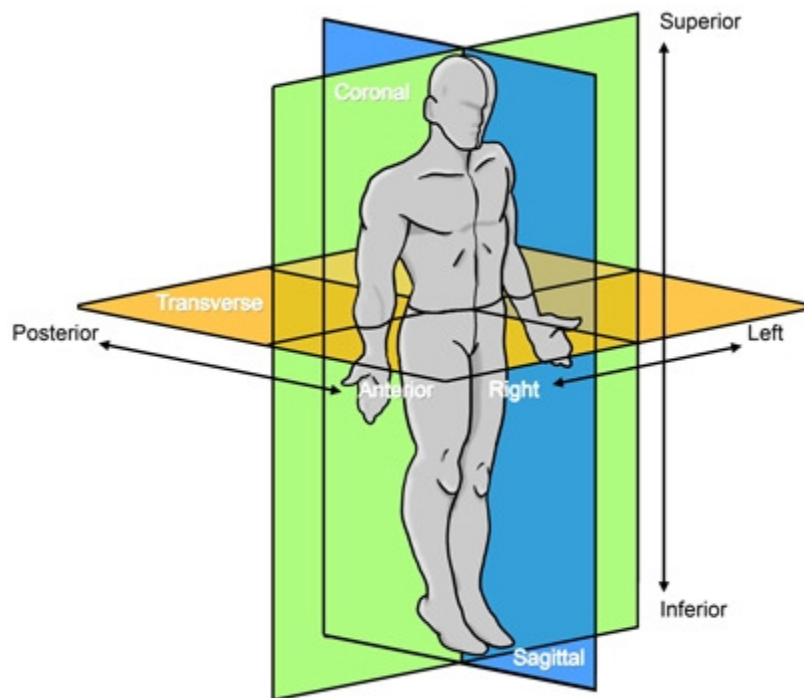
Figure 2.1 Anatomical planes of the human body [25]

2.2   Human Femur

The femur, alternatively known as the thigh bone, is the strongest and the longest bone in human body. There are two femurs in the human body and are positioned as left and right in a mirror image with respect to the coronal plane. The femur supports the major weight of the body during actions like walking, running and climbing. Each femur is subjected to a typical loading of up to 2 times the weight of an adult body. In human anatomy, it is the most proximal bone of the lower limb. Figure 2.2 is the labeled diagram of the lower limb. The location of the femur is inferior to the pelvis and superior to the tibia and fibula. At its distal end, the femur forms part of the knee

joint, whereas at the proximal end, femur forms part of the hip joint [25, 27].
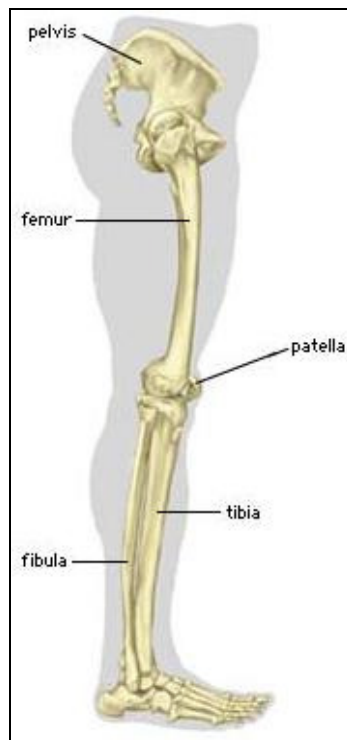
Figure 2.2 Anatomy of the lower limb [28]

2.2.1 Anatomy of the Human Femur

The femur is characterized by its long shaft and 5 bony protuberances. The protuberances are head, greater trochanter, lesser trochanter, lateral condyle and medial condyle, as shown in Figure 2.3 [28, 29]. At its proximal end, the head and greater trochanter are located medially and laterally. The lateral and medial condyles are located at the distal end of the femur and are distinguished in the coronal view. The lesser trochanter is located below the head and greater trochanter.

The ends of femur are covered with articular cartilage, which protects and cushions the bone during movement of joints. The protuberances, at both ends are called the epiphysis as shown in Figure 2.4. The femoral shaft is called the diaphysis. The transitional zone between epiphysis and diaphysis is called the metaphysis. The epiphyses are comprised of sponge bone in the interior of the femur. The sponge bone, or cancellous bone, is softer, weaker, less dense and less stiff than the compact bone. It is noted that the compact bone forms the structure of the bone, and it is exterior to the sponge bone. The femoral shaft, or diaphysis, is comprised of compact bone, and contains the medullary cavity indicating the interior empty space [30].

6
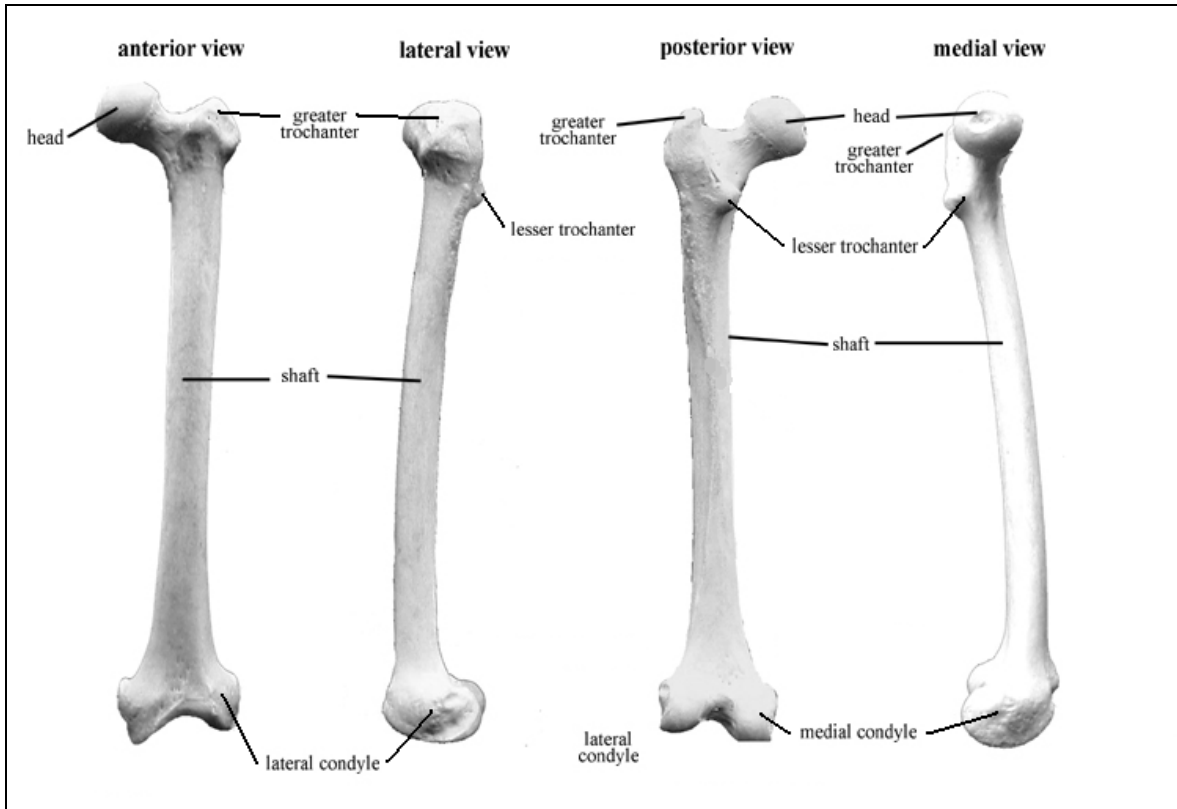
Figure 2.3 Different views of human femur [29]

Hip Joint

The hip joint, primarily works as a ball bearing due to the presence of a rigid ball and socket system. The acetabulum of the pelvis acts as a hip socket, and forms a deep cup that surrounds the ball of the femoral head. The acetabulum has an ability to deform elastically, as the joint in loaded it deforms readily around the femoral head [31, 32]. The hip joint supports the weight of body due to its complex design and allows the hip to flex, extend and move from side to side, also called abduction and adduction and rotates around the femoral head. As such body is able to engage in dynamic motion such as running or walking. [33, 34]. Hip joint is shown in Figure 2.5.

Femoral Head

The femoral head is part of the hip joint, and is oriented at an angle with respect to the median plane. This angle varies from static posture to dynamic posture, resulting in change of load applied to the femur in a cyclic manner during gait.

Knee Joint

The knee joint consists of the distal end of femur and the proximal end of tibia and fibula. The patella or knee cap, usually slides on a groove at the femur end and gives protection in the front

[36]. It is the largest, strongest, and heaviest joint in the human body, and like hip joint, during static postures; it supports almost half of the body's weight. It also provides mobility to the body, by allowing femur to rotate on the proximal end of tibia and fibula [37]. Figure 2.6 indicates the ligaments, cartilage and menisci as the soft tissues that form the knee joint as an assembly. The ligaments and cartilage allows smooth movement of the lower extremities [13]. They also prevent the knee from moving too far from side to side such that femur, tibia and fibula are kept in place to allow for continuous motion [37]. Centering of the knee is ensured by ligaments essential to minimizing wear and tear on the cartilage [38]. The meniscus functions as a shock absorber and provides a cushion to the tibia and fibula [13]. It also minimizes the amount of stress carried by the femur on to the articular cartilage [38].
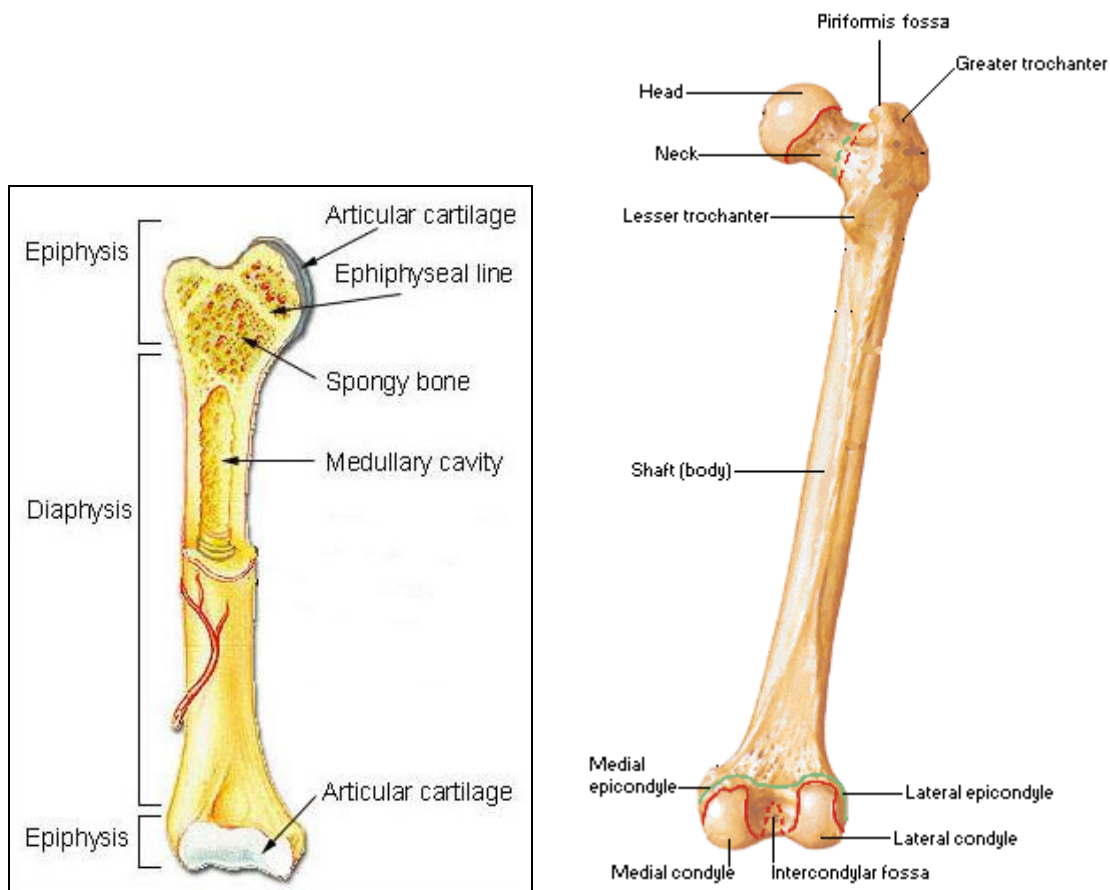
Figure 2.4 Bone anatomy of (a) long bone and (b) femur (posterior view) [30]

8
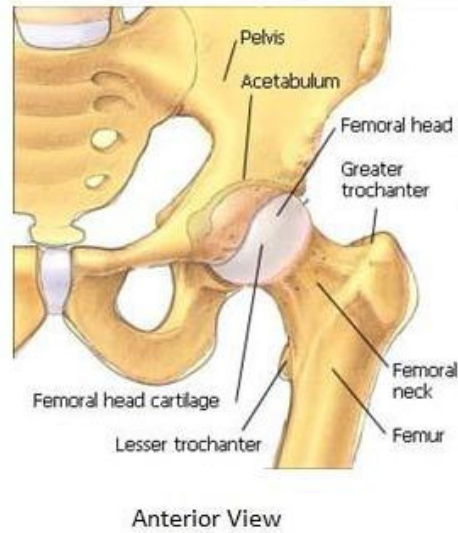
Figure 2.5 Anatomy of hip joint [35]
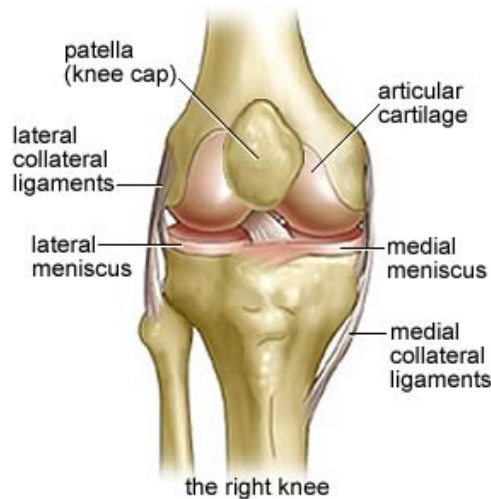
Figure 2.6 Anatomy of the human right knee [38]

2.3   Gait Cycle

Gait, alternatively called as bipedal locomotion, is a process by which humans are able to perform everyday physical tasks such as walking, running and jumping. Hip and knee joints provide an integral mechanism to perform these activities by supporting half of the body's weight and providing equilibrium. Gait is defined as the type of locomotion carried out by limbs. Depending on the type of activity, joints experience different types of biomechanical load patterns, kinetic and potential energy cycles. Walking, the simplest form of activity is a product of repeated cycles of gait. [39]. A typical human gait cycle is shown in Figure 2.7.

9
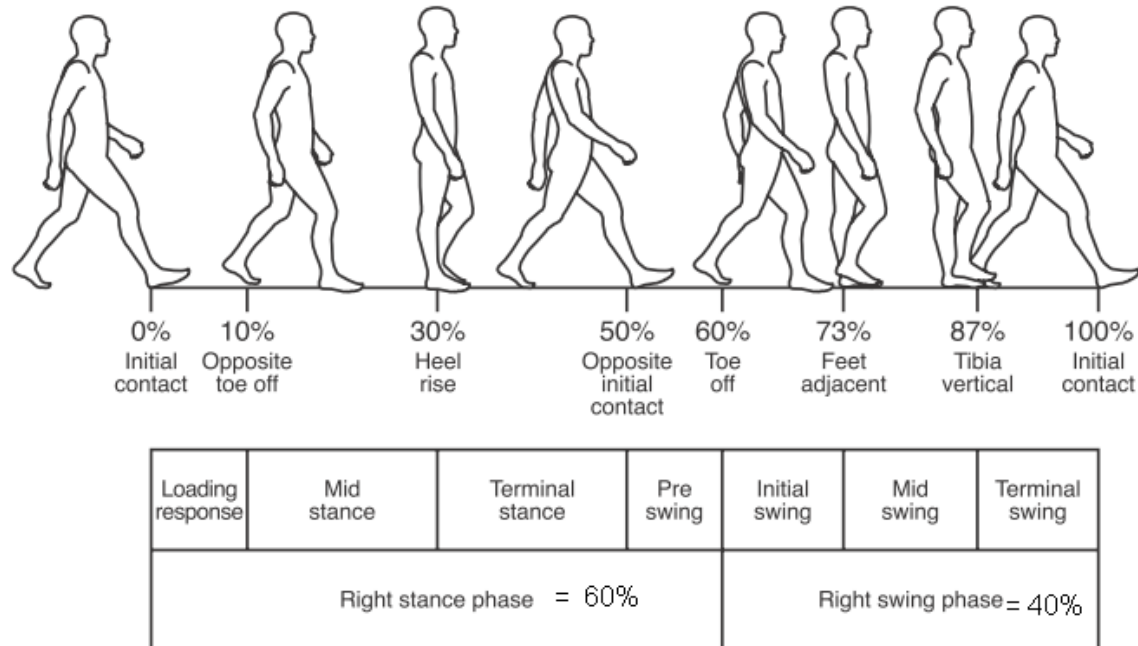
Figure 2.7 Human Gait Cycle [40]

An average adult takes some 0.9-1.5 million steps annually. Researchers have divided the gait into two primary phases – the stance phase, which is about 60% of the gait cycle, and the swing phase which constitutes the remaining 40% [41].

The stance phase is further divided into the loading response, midstance, terminal stance and pre swing. The loading response begins the instant when the right heel comes in contact with the ground, termed as initial contact or heel strike. The loading response stage ends, once the toes of the left foot leave the ground (contralateral toe-off). In the loading response phase, the body experiences the double limb stance [42]. The midstance follows the loading response and begins with the contralateral toe-off and ends when the body's centre of gravity is shifted directly over the right foot. The terminal stance follows the midstance and ends when the left foot contacts the ground (contralateral initial contact). During the terminal stance, after weight loading at around 35% of the gait cycle, the heel of the right foot rises from the ground. Note that weight loading period of the right leg corresponds with weight unloading period of the left leg. Preswing begins at the contralateral initial contact, and ends when the toes of the right leg leave the ground (toe-off). The preswing is also performed with a double limb stance.

The swing phase is further divided into 3 stages the initial swing, midswing and terminal swing. The initial swing stage begins at right toe-off, and ends when the right knee reaches a maximum

10

flexion of approximately 60 degrees. Midswing begins from the maximum knee flexion to until the tibia is perpendicular to the ground. Lastly, terminal swing begins when the tibia is perpendicular to the ground and ends at initial contact, at which point the gait cycle resumes again. The knee reaches its maximum extension just before initial contact [41, 42].

In the above example for gait cycle, the single limb stance, during the stance phase is carried out by the right leg and the weight is then transferred to the left leg during the swing phase. Table 2.1 summarizes the gait cycle.

2.3.1 Motion of the Hip Joint

The femoral shaft is engaged to the hip joint by an angle with respect to the median plane. During gait cycle, motion of the hip joint is three dimensional. Flexion- extension occurs in saggital plane about mediolateral axis, adduction-abduction occurs in frontal plane about anteroposterior axis and internal-external rotation occurs in the transverse plane about longitudinal axis [43]. These angles change throughout the gait cycle, in the saggital plane, range is from $0 - 140^{o}$ for flexion and $0 -15^{o}$ for extension, in the frontal plane, abduction ranges from $0 – 30^{o}$ and adduction from $0 – 25^{o}$. In the transverse plane, internal rotation ranges from $0 – 70^{o}$ and external rotation ranges from $0 – 90^{o}$.

2.4 Clinical aspects: Femur Fractures

Femur as the longest and strongest bone in the human body will handle a large amount of compressive force or extensive trauma before it fractures. Femur fractures are often associated with multisystem trauma, resulting in potentially life threatening injuries to its related systems [2]. In addition, an injured femur may cause further injury or complications, as it may disrupt blood supply by cutting or tearing surrounding blood vessels or nerves, it may also expose bone to outside environment causing bone infection. Clinically, the most common causes of femur fracture are bone diseases or a physical impact.

Accidents such as motor vehicle collisions, falling from high elevations, taking a hit during sport activites are another cause of femur fractures. Motor vehicle collisions are a source of high-energy trauma resulting in serious injuries to the bone. Pediatric femur fractures are mostly due to physical abuse [45].

			% of Gait Cycle	Weight Loaded by	
Gait Cycle	Stance Phase	Loading Response	0 – 10%	Double Limb Stance	
		Mid-stance	10 – 35%	Single Limb Stance	Initially responded leg
		Terminal Stance	35 – 52 %	Single Limb Stance	
		Pre-swing	52 – 62%	Double Limb Stance	
	Swing Phase	Initial Swing	62 – 100%	Single Limb Stance	Contralateral leg
		Mid-swing		Single Limb Stance	
		Terminal Swing		Single Limb Stance	

Table 2.1 Summary of stages in the gait cycle for walking [41, 42, 44]

2.5   Biomechanical Aspects: Femur Fractures

Femur fractures often occur to osteoporosis patients either due to high energy trauma or a low energy fall. However, femur fractures occur in 0.1 to 6% of total hip replacement (THR) cases [7, 8]. Femoral fracture patterns vary according to direction and amount of force applied. Depending on this femur fractures can be broadly categorized as proximal femur fractures, femoral shaft fractures and distal fractures. However, in this study main point of focus is femoral shaft fractures.

2.5.1 Femoral Shaft Fractures

Femoral shaft fractures are generally produced due to five main types of loadings: tension, compression, torsion, bending and a combination of bending and compression [10, 45]. High energy trauma or ill-fit orthopaedic implants are the causes of femoral shaft fractures [46-49]. As shown in

Figure 2.8.

When the tensile force is applied to the femoral shaft, a fracture pattern occurs normal to the direction of load assuming equal amount of forces being applied to both sides [45, 50]. This type of fracture is called *simple transverse fracture*. The fracture occurs along the planes where the tensile stresses are the highest. This type of fracture does not generate any small particles or bone debris [34, 50].

High compressive loading can result in a fracture along a plane that is at an oblique angle with respect to the direction of the applied load. Such a loading condition causes extensive shear stresses along the oblique plane [51]. In other words, the compressive force produces a fracture along the planes of high shear stresses.

Torsional forces generally result in a spiral type fracture. In these cases, a small crack on the surface of the shaft initiates a fracture which continues through the bone in a spiraling manner. The point of initiation occurs parallel to the axis of the specimen in a plane where the highest shear stresses are observed. The remainder of the fracture pattern occurs within planes where the tensile stresses exist. This type of the fracture pattern is called an oblique spiral fracture [50, 51].

Bending forces cause half of the femur to go into tension and the other half to go into compression. This results in a fracture pattern which is consistent with tensile and compressive forces. In other words, a simple transverse fracture will be present on the tension side of the femur whereas an oblique fracture will be seen on the compression side. Typically 2 oblique fracture patterns are observed on the compression side which causes comminution. This type of fracture is called a *butterfly fracture*, and the comminution is called the *butterfly fragment* [50, 51].

A femoral shaft subjected to a combination of bending and compressive forces demonstrates a similar fracture pattern to that of bending force only. In this mode of loading, however, the butterfly fragment will involve more than 50% of the cortex. Thus the cortical contact between the

proximal and distal fragments will be less than 50%. As the amount of the applied compressive force gets greater, the butterfly fragment consists of more than one piece [50].

Figure 2.8 Type of Forces that fracture femoral shaft: (a) tensile force, (b) compressive force, (c) torsional force, (d) bending force, (e) combination of bending and compressive forces [10]

2.6   Femur fracture fixation Methods

Femur fractures can be treated using non surgical or surgical methods, depending on number of factors including, medical condition, fracture location and age of patient. In the past several years, there have been significant developments in the treatment of femoral fractures. Non surgical methods like traction and casting are no longer preferred form of treatment, largely because of the advantages of early ambulation and decreased hospital stay [2].

In comparison, surgical methods provide a stable and secure means of healing fractured femurs. The most common methods are intramedullary nailing and plating [2, 46]. However, there are major disadvantages of using the intramedullary fixation method. First, the intramedullary fixation may result in a rotational deformity [2]. Second, the intramedullary fixation cannot be used in the case where many segments and comminutions are at the site of fracture. Third, a shortening of overall length of the femur upon union may be observed. Fourth, reaming of either the epiphysis up to an appropriate canal diameter may cause additional risk and serious complications such as fracture of the femoral neck [46] . Fifth, due to the nature of the intramedullary nailing the nutrient artery is damaged following the implantation [10].

2.6.1 Plating

Bone plate fixation, also known as plating, has been used as a method to repair fractures since 1800's. In this method, the healing of bone fractures can be assisted by placing a bone plate over the fractured site and securing it by screws and/or cables [52]. The role of bone plate fixation hardware is to hold the fractured bone segments in position without allowing tensile stress at the fractured surface and to provide the adequate amount of compressive stress at the fracture interface in order to accelerate bone healing. The bone plates available commercially are made from metallic materials such as stainless steel, cobalt, titanium or titanium alloys.

Bone plates are generally categorized into four main types: neutralization plate, compression plate, buttress plate and condylar plate as shown in Figure 2.9 [10]

Bone plate fixation has many benefits; one of the major benefits as compared to intramedullary nailing is that it can be used in several applications. For instance, femur fractures to the proximal end of the femur are relatively common following total hip or hip stem replacements. In these cases retrograde nailing cannot be used to fixate the fracture surface and antegrade nailing is generally considered to be too risky to be used in practice. In these cases practitioners generally use bone plates to fixate the fracture surface. The other benefit is that, in the place of multiple bone segments, bone plates are less likely to cause shortening of the injured femur. This is because unlike intramedullary nailing, bone plates can maintain an appropriate distance between segments. Upon full recovery, the length of femur is generally expected to be approximately equal to the contralateral femur [10, 50].

Bone plate fixation also eliminates the misalignment and deformity caused by lateral rotation. Since the bone plate is applied directly across the segments of a fractured bone, the alignment prevents rotation. Bone plate fixation can be directly applied on the fractured site, without reaming of the intramedullary canal or cutting of the epiphyses and nearby growth plates. This is particularly advantageous in pediatric patients [11].

Despite the benefits listed above, one of the problems arising from internal fixation involves the amount of stress being applied to the healing bone. When load is applied to the plate fixated bone, the metal plate receives majority of the transferred load. As a result, the bone weakens around the plate, and upon removal of the plate can cause re-fracture of the bone. This phenomenon is known as stress shielding. Stress shielding occurs when two or more components with different moduli

(a) Neutralization Plate

(b) Compression Plate

(c) Buttress Plate

(d) Condylar Plate
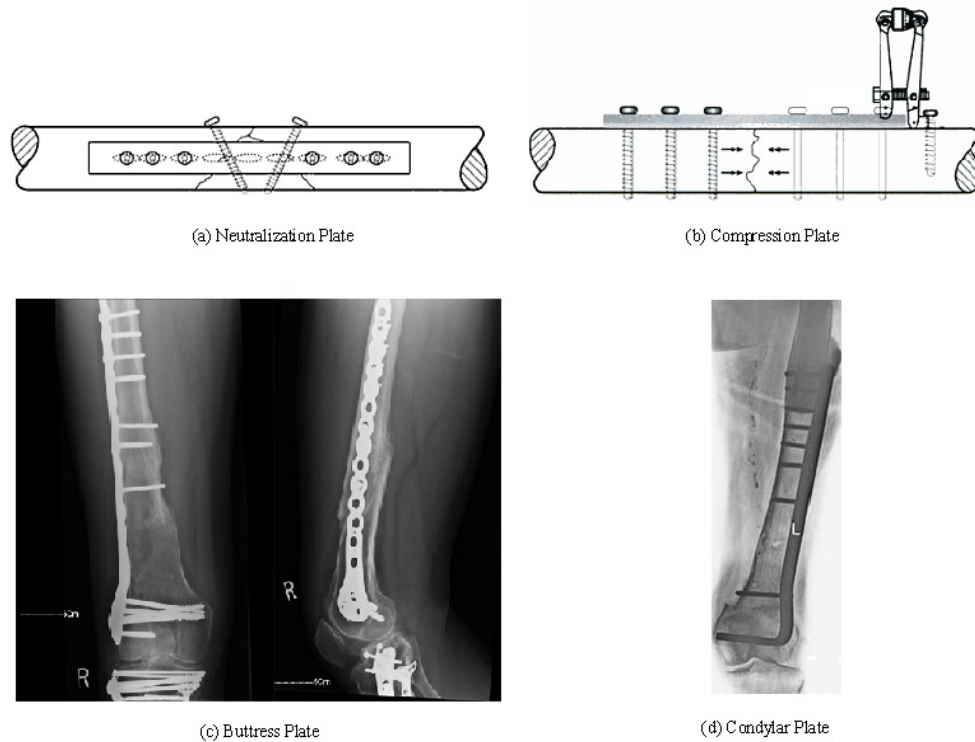
Figure 2.9 Major type of bone plates [10, 53]

form one mechanical system. The component with the highest stiffness will bear more loads while protecting the other, as is the case with the bone and plate system. According to Wolff's law of stress related bone remodeling, lower bone density and higher porosity in the healing bone is often observed when stress shielding has occurred, that phenomena is called bone resorption. Thus, the bone will remain weak and less dense even after the full union of the fracture site and is more prone to refracturing once the bone plate is removed [2, 10, 13]. As a result of bone resorption, a longer duration of bone plate fixation is required until the healing bone gains a sufficient amount of stiffness [50]. Therefore, the ideal bone plate must transfer a sufficiently large load to the femur in order to maintain healthy functionality; however it must also be stiff enough to maintain proper alignment of the fracture surface.

One of the other major disadvantages of bone plate is that a second surgery is required to remove the implant. This additional surgery can itself damage the bone and is an obvious inconvenience. It also has a high risk of infection also compared to intramedullary nailing. This is due to the large amount of hardware such as screws and cables used in this method. Therefore an extremely careful sanitization process is required during preparation prior to the operation, and the appropriate

16

antibiotics must be prescribed in order to prevent serious illness due to infection. Plating also has a high risk of nonunion due to hardware malfunction. The screws and cables used to fix the plate to the bone are more prone to failure compared to IM nailing. If the hardware fails to maintain proper alignment at the fracture surface then immediate corrective action (usually surgery) is required [50].

Considering the drawbacks of intramedullary nailing and metallic bone plate fixation methods, there have been many studies concerned with the development of methods and techniques with appropriate mechanical properties (Table 2.2) to improve fractured bone healing and reduce stress shielding.

In one study, Woo et al., proposed a tubular stainless steel plate, and compared its performance with a standard steel plate and a thin titanium plate. They observed similar results for the tubular plate and the titanium plate; however, the tubular plate had much higher bending and torsional stiffness than the thin titanium plate and would provide adequate fragment control in the pre-union phase of healing [54].

Beaupre et al. studied the factors influencing the bone plate such as screw tightness, sliding friction, and magnitude of load by using an FE model [55]. In the FE model frictional interface elements between the bone plate and the bone were employed while the screw head was separated from the surrounding surfaces in a way that it would not participate in any stress loading. The authors concluded that the factors contributing to the stress shielding effect were the material properties of the bone plate as well as the placement of the plate, rather than the amount of slippage between the plate and the bone.

It has been observed that the need for rigid support diminishes as the fracture starts healing. Ideally, the stiffness of the fixation device should decrease as the bone strength increases. It is not possible to achieve it with metal implants; however, to achieve this goal composite materials should be used in place of metal bone plates.

In one study on composite materials, Saidpour investigated the suitability of using a short carbon fibre- reinforced plastic composite as a bone-plate for fracture fixation. Based on his analytical results, the composite plate system is likely to reduce stress shielding effects at the fracture site when subjected to bending and torsional loads [56].

Fan et al. tried to achieve favorable conditions for bone fracture healing by inserting a type of soft biodegradable cushion between the fractured bone and the rigid plate, with the aim of reducing bone stress shielding and damage to the bone's blood supply [57].

2.7 Methods of Testing in Biomechanical Analysis

Biomechanical analysis uses two most frequently used methods, experimental and computational, to investigate strength and stiffness and in some cases material properties [58-60]. Experimental methods are carried out in-vivo and in-vitro. In-vivo, experiments have been performed on human subjects and have provided clinically accurate and relevant results. However, working with live subjects is not possible all the time and issues arise such as accessibility to joints to acquire relevant data. Though, mechanical in-vitro tests have been performed on human cadaveric bones and implants for almost a century. Researchers, however, have found it difficult in replicating real world physiological loading condition due to intricate interaction of hard and soft tissues. Therefore, researchers have come up with simple experimental approaches for biomechanical testing by carrying out axial compression, lateral bending, 3- point bending and 4- point bending tests independent of each other [57, 61-63].

	Type of Load	Density (g/cm^3)	Ultimate Strength (MPa)	Modulus of Elasticity (GPa)
Human Bone (Femoral Shaft)	Longitudinal Tension	1.85	133	17.7
	Longitudinal Compression	1.85	193	17.7
Titanium Alloy	Longitudinal Tension	4.50	220	116
Cobalt Alloy	Longitudinal Tension	8.80	225 (yield)	211
Stainless Steel	Longitudinal Tension	7.81	870	190
	Longitudinal Compression		1080	196

Table 2.2 Mechanical properties of human femur and metallic materials commonly used in orthopedic applications [45, 58-60]

There are many drawbacks associated with experimental testing of cadaveric bones. Availability, handling and preservation are major problems associated with the use of cadaveric bones. The other drawback is that, studies lasting several weeks can change mechanical properties of cadaveric bones as seen in previous studies, where axial stiffness was decreased by 30% over several months [63]. Furthermore, in cadaveric bones, there is inconsistency between inter specimen material and mechanical properties. As Papini et al., showed that between 25 cadaveric femurs the variation in axial and torsional stifnesses was 3.2 and 3.3 times respectively. This specimen to specimen discrepancy, makes virtually impossible for experimental results to be reproduced, thus makes difficult to draw useful conclusions from investigations [62].

Synthetic long bones are becoming popular due to their standardized geometry, similar material behavior to that of human bone and very small inter specimen variability, They are also easy to manufacture, non toxic, easy to store and readily available. Moreover, studies have revealed that synthetic bones have shown same mechanical behavior resembling to human bone in terms of axial stiffness, 4- point bending stiffness, torsional stiffness, cortical screw pullout strength, and cancellous pullout strength [62, 64-67, 67, 68].

In some studies, quasi-static loading tests have been performed to assess strength and stiffness, as well as strain gauges were used in analyzing strain and stress patterns, of long bones or long bone-implant constructs [61-64, 69-75]. Strain gauges have been commonly used by researchers, as they are easy to use, readily available and provide stable results. However, there are some drawbacks as well, like placement, as gauges have to be mounted on flat and smooth areas to ensure best possible planar strain detection. Curved surfaces of the bones tend to produce unstable results. The other drawback is that, it is impossible to predict the overall stress behavior of bones due to the limited amount of resolution obtained from strain gauges [75-77].

2.7.1 Finite Element Analysis (FEA)

FEA is another popular technique for design and evaluation of human bones and implants, often used to support biomechanical testing. As it is an inexpensive solution compared to clinical research and also can be done in short period of time. It also provides consistency between different specimens, this is ideal for comparison studies where identical testing conditions are required for all specimens. Given detailed information of the material properties of the components, a relatively high level of accuracy and repeatability can be achieved from finite

element (FE) modeling.

FEA has been used as a tool for biomechanical analysis of human whole bones since 1970s. However, the first model of human whole bone had some limitations; it incorporated only two-dimensional geometries and assumed homogenous, isotropic and elastic properties [78]. Although, models used later in the early 1980's were three-dimensional models, but they incorporated simple geometries and lacked in mimicking realistic human femurs or performing complex clinical investigations [79-81]. Nowadays, with the advancement in computer hardware and computer aided design (CAD) softwares, more accurate geometries of human whole bones can be developed. These geometries, lack in incorporating microstructure of bones, but are useful in design and assessment of human bones and implants [62, 82-86].

Studies suggest that the FEA models of synthetic femurs can provide a good comparison of stress distribution and load sharing between bones and implants; however these models assumed linear isotropic mechanical properties of bones to simplify the analysis. Clinically, the behavior of human femurs is non linear, anisotropic and viscoelastic, this might limit the models to predict the stiffness of real bones [75, 82, 83, 87].

However, on the whole biomechanical testing in tandem with FEA analysis can compensate for the complicated loading conditions that cannot be achieved experimentally and can show a good correlation of mechanical properties.

2.8   Infrared Thermography
2.8.1   Background

Infrared thermography (IRT) is a non contact optical method, a non destructive technique, where an accurate image of isothermal contours of steady or transient thermal effects is constructed from the measurement of infrared energy emitted by the target. The energy emitted by the body, can be in the form of irreversible applied mechanical load, direct heat source, ultrasonic stress waves, among others. It is widely used in various industrial applications such as aerospace, medical diagnostics, electronics, rubber, automotive and construction [88].

The first application of IR thermography was made in 1950 to measure temperature variations on the surface of the body [89], though early attempts in the implementation of thermography were qualitative. However, advancements, specifically in the development of cost-effective and high

density resolution imaging sensors, have enabled to acquire very small temperature changes, precisely and accurately.

Thermographic Stress Analysis (TSA) is a recently developed nondestructive IR technique, by which such small temperature changes induced by dynamic loading of materials are measured. The thermoelastic effect, as explained by Kelvin in 1885, is the conversion of mechanical energy into heat [90]. Thermoelasticity can best be explained by first law of thermodynamics, according to which an increase in volume under adiabatic conditions is related with decrease in temperature and vice versa.

2.8.2 Principle of IR Thermography

The principle of IR thermography when used as a nondestructive testing technique is that when heat travels through cracks, delaminations or other anomalies, the heat flow rate changes. Fourier's law describes the heat transfer by means of conduction within a material as well as from one material to another, which is described as:

$$Q = \frac{k\Delta T}{tA_h} \qquad (2.1)$$

where Q is heat flux, k is the thermal conductivity of material, Ah is the surface area on which the energy is incident, t is the thickness, and ΔT is temperature gradient [91]. The rate of conduction of heat is higher in materials with higher values of k, such as metals, than in an air gap (or vacuum) whose k value is nearly zero. The heat flow rate is dependent on the medium in which it is travelling and the presence of any anomalies in that medium. The thermal conductivity of fibre reinforced polymer composites is much lower compared to metals.

2.8.3 IR Thermography Techniques

IR thermography is effectively used for inspection of fibre reinforced polymer composites, insulation materials, composites bonded to metals, composite-concrete bonds, and flaws in concrete. As every material reacts differently to heat input, therefore, a variety of thermographic methods have been developed to suit individual material and geometric configurations. The energy sources can be broadly divided into distinct groups, namely, optical and mechanical. In optical excitation, the defects are stimulated externally, and energy is introduced to the surface of

the test material until it reaches a flaw or discontinuity from where it is reflected back to the surface as thermal wave. When mechanical excitation heats the imperfections internally, mechanical fluctuations injected to the specimen pass through in multiple directions, dispersing energy at the discontinuities in the form of heat, which then travels to the surface by conduction.

Three typical methods of thermography based on these two excitation modes are lock-in thermography, pulsed thermography and vibrothermography [92]. The thermal excitation for the detection of flaws, cracks or damaged zones is generally performed by three methods, which belong to the category of externally applied thermal field (EATF). The principle of EATF thermography is that heat is applied to the specimen surface, and the radiation emitted from the surface, as a thermal gradient, is studied. The thermal gradient will be uniform, and the isotherms will be straight lines if there is no defect in the specimen. In case there is a defect in the specimen, the isotherms will be curved and a non-uniform temperature will be observed due to disturbance in the heat flow [93].

EATF thermography can be divided into active and passive, depending upon the mode of thermal excitation. In passive IR thermography, thermal excitation is done by an environmental source of heating (the sun). Passive thermography is generally used to inspect large objects such as an entire building whose thermal diffusivity can be effectively measured by using the sun as heat input. However, it is a qualitative mode of inspection [94].

Active thermography is a better option for defect detection due to its capability for quantitative measurement and classification of the defects. In this mode of thermal inspection, the specimen is energised by an incandescent light bulb, heat gun, flash lamp or quartz lamp. The intensity and duration of heat pulses from these sources are easily adjusted.

On the basis of the orientation of flaws and discontinuities in the specimen, EATF is further divided into parallel and normal modes [95]. Subsurface defects, such as delaminations, are effectively detected by the normal mode of EATF, as the infrared radiation emitted from the specimen surface may be interrupted due to the flaw and result in hot spots. The flaws of the surface, such as cracks, disturb the heat flow parallel to the specimen surface producing convexities in the isotherms or changes in surface temperature, which are efficiently detected by the parallel EATF mode. The ability to detect a flaw in the parallel mode is governed by the temperature difference across the crack and the duration for which the thermal pattern exists.

2.8.4 Lock-in Thermography

Introduction

One of the most widely used thermographic techniques is lock-in thermography, which is a nondestructive examination method that uses the phenomenon of thermal waves. A thermal wave is the reaction of a medium to an intermittent heat supply. Thermal waves are produced by intermittent heating of the surface of an object. These waves transmit into the solid object, and some of them are reflected back at the interfaces. The interfaces are the boundaries between dissimilar materials. A pattern of harmonic oscillating radiation is created when the incident and reflected thermal waves interfere on the surface of the specimen which can be recorded by instruments. The detection of the heat waves can be done by various means. Infrared thermography is one of the best and fastest methods for examination and defect detection of a large region in field test. Lock-in thermography is a combination of IR thermography and the thermal wave technique which allows for fast and remote nondestructive testing [96].

Principle of Lock-in Thermography

Lock-in thermography (LT), a quantitative technique, is used quite often for rapid and remote recognition of subsurface structures. In addition, depth quantification by LT is performed simply through the diffusion length equation. The principle of LT is established on the propagation and reflection of thermal waves that are initiated from the surface into the examined component by absorption of modulated radiation. Phase images are acquired by superposition of the initial thermal wave and its internal reflection which display hidden thermal structures down to a certain depth below the surface. They are undisturbed by variation in emissivity of the surface and non-uniform distribution of heat emitted by the source [97].

In other words, in lock-in thermography, with adequate time for periodic heating, the surface temperature changes periodically in a sinusoidal pattern that develops from the transient state to the steady state. The heat source is used together with an adjusted intensity of a continuous sine wave source. The IR camera is utilized to detect the surface temperature of a thermal wave transmitting into materials and then produces a thermal image that displays the local variation of thermal waves in phase or amplitude [92].

Setup of Lock-in Thermography

The test specimen is exposed to sinusoidal thermal excitation, where input frequency controls its

magnitude and phase during lock-in thermography. A modulated laser beam is used to thermally excite a specimen for a point inspection whereas heating is done by a modulated heating beam for a surface area inspection. An oscillating thermal field is generated inside the specimen due to this thermal excitation which is recorded by IR thermal camera from a distance. The setup is shown in Figure 2.10. The input and output signals are synchronized by a lock-in amplifier and thus the magnitude and the phase of the input and output heat waves can be calculated with respect to reference modulation. With the advancement in technology of IR thermography, the digitized data can be used to acquire the output signal in the absence of an amplifier. The local optical and infrared surface feature is related to the magnitude of the signal, and the phase is proportional to the transmission time delay. Due to the difference in the magnitude and phase of the signals between defective and defect free areas of the specimen, the subsurface flaws can be easily identified by monitoring the signals [98].

Advantages and Disadvantages of Lock-in Thermography

Lock-in thermography is used for defect detection near the surface, determining material properties and measuring the thicknesses of coatings. It is advantageous in the detection of delamination and is a flexible tool for nondestructive examination. Unlike x-rays, it is not harmful for humans and requires lesser time for examination. The lock-in thermographic technique is able to conduct nondestructive testing over a large region in a small interval of time. It is a noncontact technique, and the equipment is portable so that it can be used in almost any field test. It is also used in the inspection of printed circuit boards, electric installations and quality control in arc welding [99, 100].
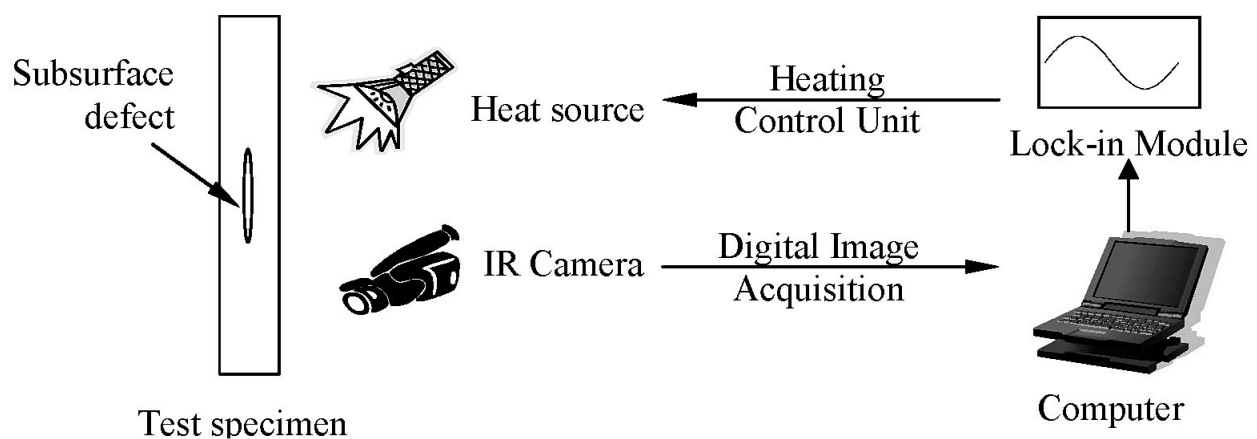
Figure 2.10 Typical of setup for lock-in thermographic inspection[91]

Lock-in thermography has better depth resolution than pulse thermography [101]. It gives better results for slow thermal response materials (such as carbon fibre reinforced polymers) as it uses significant power optical excitation sources using a long pulse mode, even though it takes a longer time than pulse thermography [91, 98]. This technique is still growing and offers some advantages over other nondestructive techniques.

The subsurface defects and discontinuities can be successfully found by lock-in thermography, which is more sensitive than pulse thermography. The sensitivity of lock-in thermography is inversely proportional to the depth of the defect. In a specimen, the depth of penetration of low frequency heat waves is higher than high frequency heat waves. As the frequency of heat waves changes, the sensitivity of lock-in thermography also changes. When the depth of penetration for both high frequency and low frequency thermal waves is the same, lock-in thermography responds more accurately to high frequency thermal waves. High detectivity is achieved in inspection when more than one frequency of waves is used. A defect at a certain depth produces a phase difference which is significantly influenced by inspection frequency. A very small, or no, difference at all may be produced by a defect at a certain frequency. The defect generates maximum positive and negative phase differences at two certain frequencies [102].

CHAPTER 3. METHODS AND MATERIALS

3.1   General Approach

In order to evaluate carbon /epoxy bone plate as a femoral fracture fixation method, two large left femurs, with two fracture fixation constructs (one specimen per group) were assessed. The investigation was performed using test conditions; (1) an injured femur with hip stem and a transverse mid-shaft fracture of 5 mm and (2) a healed femur with hip stem. The specimens were subjected to a dynamic axial load with average force of 800 N, to represent 1 times body weight (BW). The femurs were cycled between the ranges of 400 N to 1200 N to ensure that bone remained within the elastic range during the loading cycle. The temperature distributions on the femur due to varying loading regimes were recorded using an infra-red camera. The femurs were mounted in a mechanical tester, oriented at 7 degrees of adduction in the coronal plane and aligned vertically in the sagittal plane in order to mimic contralateral toe-off during mid stance phase of gait cycle and where maximum load bearing occurs, as shown in Figure 3.1 [71, 103, 104]. The difference in three dimensional surface stresses (sum of principal stresses) for both the constructs were obtained and compared to analyze the effect of stress shielding. The axial static and dynamic stiffness were also compared for both the constructs in a simulated femoral shaft fracture model in the presence of total hip replacement. Finite element analyses were also performed by modeling the femur fracture fixations using titanium as well as carbon epoxy plate. The models simulated identically resembled the specimens used in the experimental study and were validated by comparing with the experimental results.

3.2   Material Selection

3.2.1   Selection of Specimens

Two large left fourth-generation composite femurs (model 3406, Pacific Research Laboratories, Vashon, Washington, USA) manufactured with a special injected black dye, as shown in Figure 3.2 [105]. The black dye was used to ensure perfect infrared emission [106].

The fourth-generation composite femur specimens were specifically designed and developed to model natural cortical bone using a mixture of glass fibers and epoxy resin pressure injected around a foam core. The intramedullary canal located in the mid shaft area had a diameter of 16 mm.

Figure 3.1 Axial loading of femur at 7 degrees of adduction

Figure 3.2 Fourth generation large left femur

This design also limits the number of screws that can be applied to the femoral shaft and is meant to simulate a worst case scenario. The material for cancellous bone comprised of cellular rigid polyurethane foam. The mechanical properties for the specimens were obtained directly from the manufacturer and are summarized in Table 3.1 [105].

| | | | Compressive | |
Layer	Material	Density (g/cm^3)	Strength (MPa)	Modulus (GPa)
Cortical	Short glass fibre filled epoxy	1.64	157	16.7
Cancellous	Cellular rigid Polyurethane	0.2	3.9	0.155

Table 3.1 Material properties of composite femur specimens

The fourth generation composite femur specimens were specially designed with a larger canal diameter. The detailed geometry of the specimens is shown in Figure 3.3.

Dimension	
a	485 mm
b	52 mm
c	37 mm
d	120°
e	32 mm
f	93 mm
g	16 mm
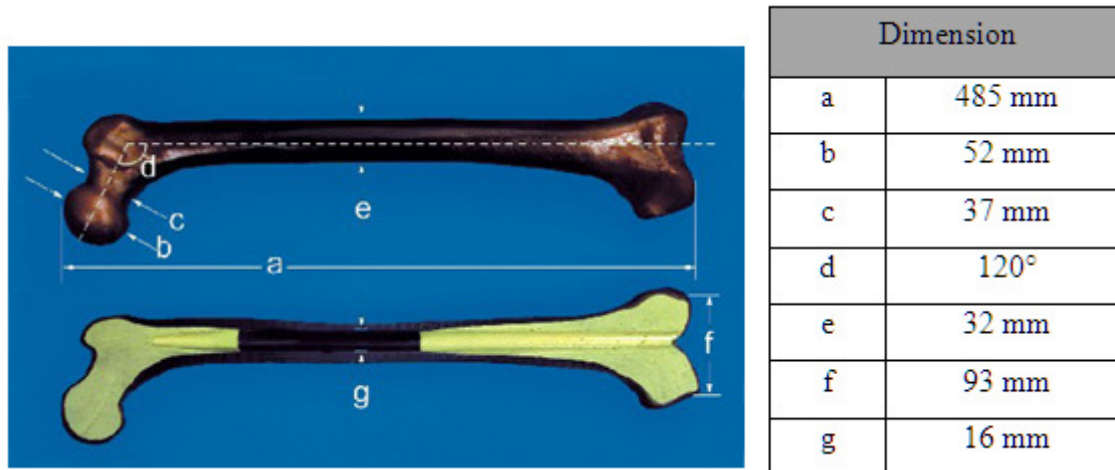
Figure 3.3 Detailed geometry of large left fourth generation femur [105]

Bone plate

Two different constructs for bone plate were used. Construct 1 was a Zimmer non-locking (eight hole) cable plate (Warsaw, IN, USA). The plate can be fixed with either unicortical or bicortical screws depending on the biological condition of the bone. The bone plate consists of 8 non-locking holes (i.e. non-threaded screw holes). Either a unicortical or a bicortical screw could be threaded through the screw hole depending on the biological condition of the bone. In this study, fixation was done by 4 bicortical and 4 unicortical screws. Construct 2 was a quasi isotropic laminate

composite, manufactured by autoclave technique. The material used was a pre-impregnated carbon fibre /epoxy commercially known as T700-M21 and manufactured by Hexcel Corporation, USA. The thickness of the UD plies was 0.26 mm and the total numbers of plies for the laminate were 16. Figure 3.4 shows the geometry of bone plates for both the constructs.

(a)   **(b)**
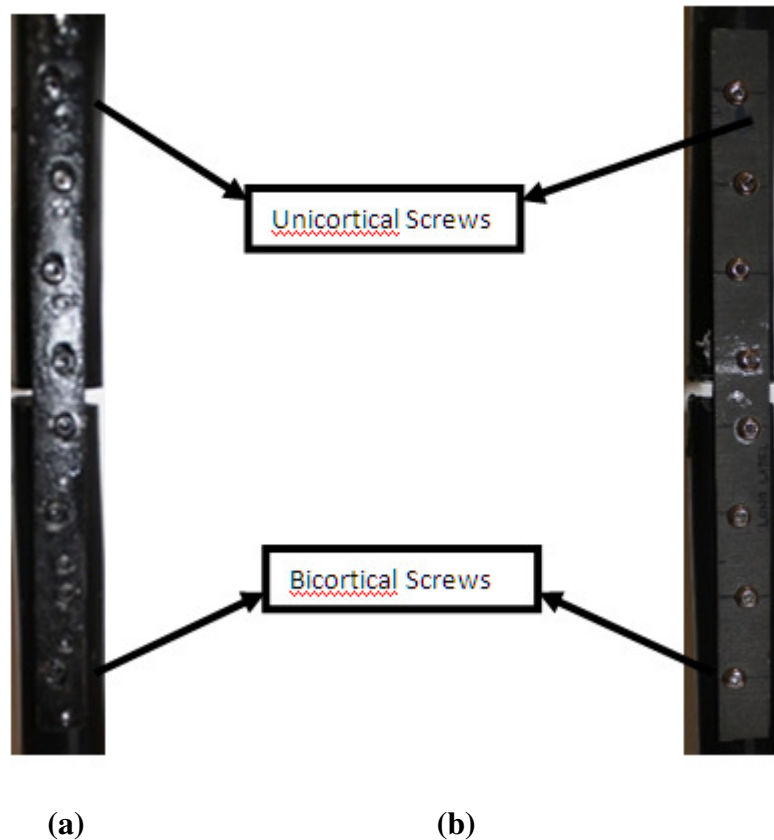
Figure 3.4 Zimmer Cable-Ready Bone Plate: (a) 8 non-locking hole bone plate (b) detail view of screw hole and cable insertion.

Bone screws

In this study, for constructs 1 and 2, both unicortical and bicortical pin head bone screws were used. The screws were made of 316L medical grade stainless steel (Synthes, Paoli, PA, USA). Proximal fixation was achieved with 4 unicortical screws, 4.5mm in diameter and 14mm in length. Distal fixation was achieved with 4 bicortical screws, 4.5mm in diameter and 50mm in length. The unicortical screws were used at the proximal end of femur, due to the presence of total hip replacement, to avoid crack initiation, whereas at distal end, bicortical screws were used. This was done as per common medical practices [107, 108].

Hip stem

Two Exeter™ Total Hip Systems (Stryker, Mahwah, NJ, USA) were used in this study (Figure 3.5). Each system consisted of an Exeter™ Femoral Stem and an Orthinox™ Head which were made of cobalt-28 chromium-6 molybdenum alloy. The Orthinox™ Head consisted of a spherical head placed on the tip of the hip stem to permit simulation of the human ball-and-socket hip joint.

Figure 3.5 Exeter^{TM} Total Hip System (hip stem) used in this experiment

3.3   Specimen Preparation

3.3.1   Femur preparation

In order to incorporate specimens into the mechanical testing system, it was necessary to anchor the femurs at the distal end. This was done by removing the femoral condyles partly with band saw on the lateral and medial sides and then long axis of the femoral shaft was aligned vertically in the sagittal and frontal planes before potting in 88mm X 88mm X 75mm steel chamber using commercially available anchoring cement (Flow-Stone, King Packaged Materials Company, Burlington, ON, Canada) [109], as shown in Figure 3.6.
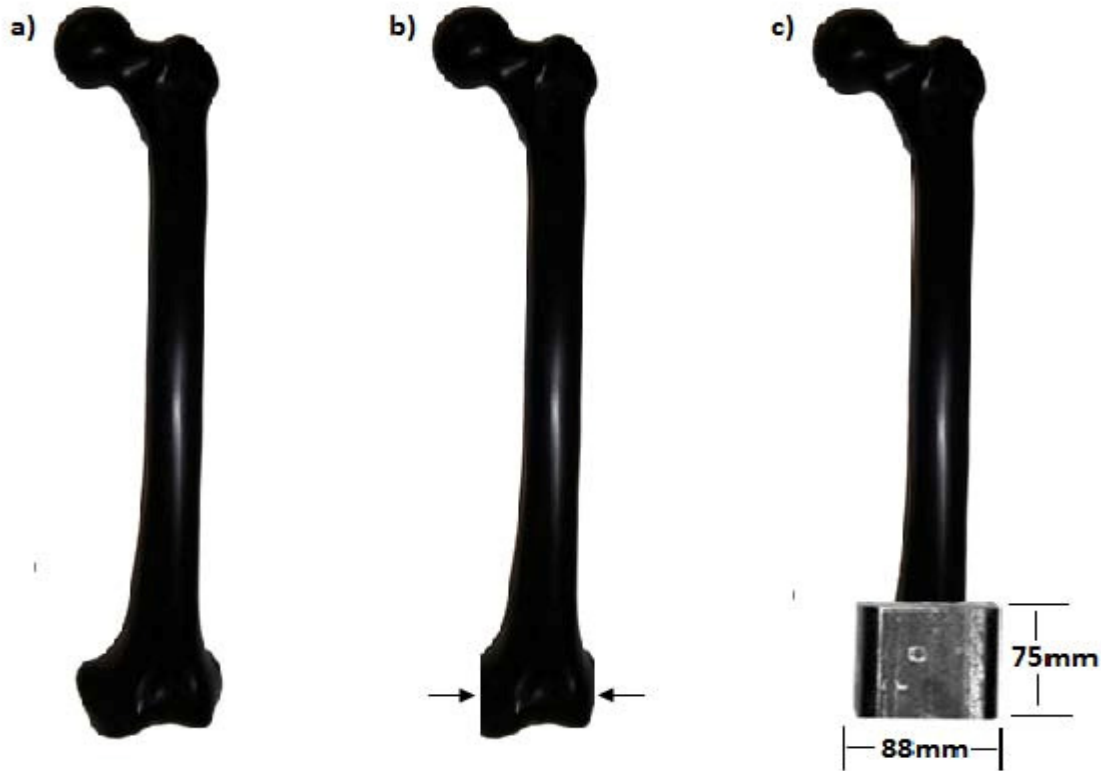
Figure 3.6 Procedure for potting a femur

Once potted, each femur had metallic hip stem installed at the proximal end to mimic total hip arthoplasty surgery. This was done in 3 steps. First, using an industrial band saw, proximal segment of each femur was removed by cutting at approximately 35° angle from the greater to the lesser trochanter. Second, by using a rasping device, the cancellous bone was removed from the incision area. Third, each hip stem was inserted and fixed using polymethyl methacrylate (PMMA) bone cement (Simplex P, Stryker, Mahwah, NJ, USA). The specimens were left for about 15 minutes until the cement was completely solidified. Figure 3.7 illustrates the hip stem implantation procedure.

3.4   Levels of specimen conditions
Synthetic femurs with following two conditions were used in current study.

Level I: Injured Femurs with Hip Stem

The injured femurs implanted with hip stem and having 5 mm gap, clinically mimicked a femoral mid shaft fracture repaired with bone plate. The transverse cut was made at mid-shaft level, by using an industrial band saw, approximately 200 mm proximal to the cement potting chamber.
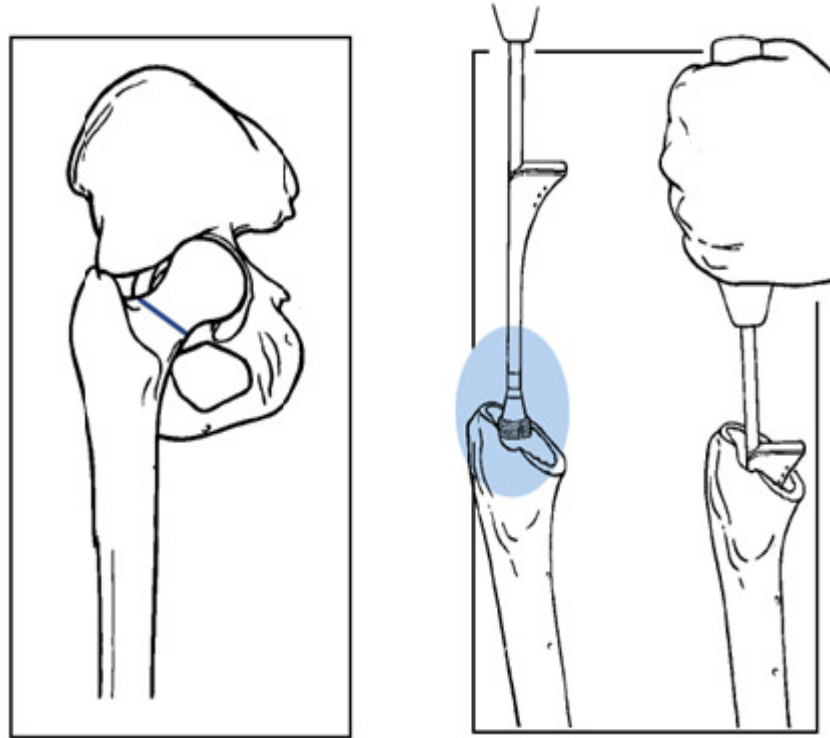
Figure 3.7 Exeter hip stem implantation procedure [110]

Level II: Healed femurs with Hip Stem

The healed femurs with hip stem mimicked complete union at the fracture site. Once the healed femurs were tested a transverse cut was made at mid-shaft to prepare specimen for Level I condition. Clinically healing occurs after fracture, but in this study healed femurs were tested prior to injured femurs.

3.5   Construct Designs

Two types of constructs were used in this study, as shown in Figure 3.8. The difference in both constructs was in terms of bone plate. In Construct 1, commercially available titanium plate (Zimmer Inc., USA) and for Construct 2 carbon fibre/epoxy, (commercially known as T700-M21) plate was used. However, in both designs, plates were installed by 4 unicortical screws and 4 bicortical screws at the proximal and distal end of femur.

Figure 3.8 Two conditions of testing (a) Injured femur with titanium bone plate; (b) Injured femur with carbon/epoxy bone plate

3.6   Static Axial Stiffness Test

The axial compression tests were performed on TESTRESOURCES 800 LE machine (TESTRESOURCES Shakopee, MN, USA). For axial compression each specimen was secured at its potted distal end by an industrial swivel vice (Figure 3.9). The proximal end of the femur was inserted into a stainless steel rectangular block 140 mm x 60 mm x 60 mm, with a sphere of 30 mm dia. cut into it. The swivel vice was tilted at 7° to simulate the proximal anatomical orientation of the femurs with hip stem implantation. The femoral ball was able to rotate inside the cup in order to simulate natural hip articulation. The cup and ball of the hip stem were assumed to be frictionless. Due to the anatomical orientation of the femur, the axial load was applied away from the axis of the femoral shaft. Because of this, axial loading was in fact a combination of axial compression and bending [62].

33

Figure 3.9 Experimental set-up for axial compression test of femur with 7° inclination

Compressive loading was applied vertically at a rate of 5mm/min with a linear preload of 100 N, to avoid slippage between femoral head and rectangular block. The testresources machine was programmed to reach a maximum displacement of 1mm. Stiffness was defined as the slope of the load vs. displacement curve. The stiffness was calculated as an average of three tests performed on each specimen. The same procedure was used for all specimens.

3.7   Dynamic Axial Stiffness Test

Dynamic axial stiffness test were performed similar to the axial test. The femur was preloaded to 100 N, then using load control the femur was loaded up to 800 N and then cycled between a range of 400 N and 1200 N (Figure 3.10). This loading scheme was chosen to represent a contralateral toe-off gait with the use of a walker, studies reveal that patients with total hip replacement and femoral shaft fracture and using a walker have femoral head forces about one times the body weight [111]. The stiffness was calculated as an average of three tests performed on each specimen. The same procedure was used for all specimens.
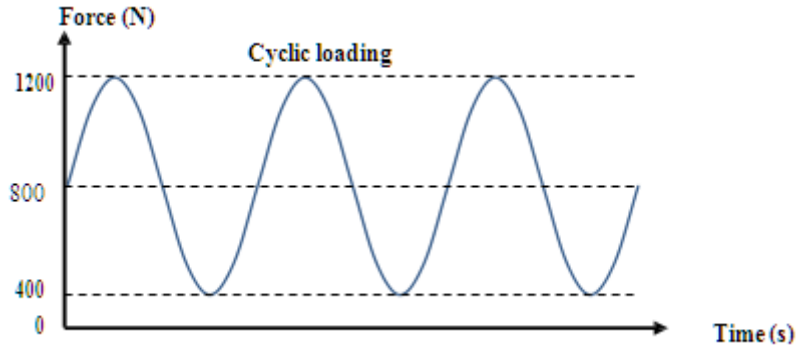
Figure 3.10 Cyclic loading application

3.8 Lock-in Thermography Experiments

Infrared thermography was used for both the constructs to measure the surface temperature of cortical bone and bone plates, in order to analyze the heat flow pattern. The experiments were carried out by SC5000 Series Silver 420 Camera, shown in Figure 3.11 (Flir Systems, Oregon, USA) at an ambient temperature of 26.3^0C. The technical data of IR camera is given in Table 3.2.

Figure 3.11 FLIR SC5000 Silver 420 Camera

The testresources 800 LE mechanical tester supplied a cyclic load to the specimens which was synchronized with the IR camera with the help of a signal generator. The cyclic average load of 800 N was applied to all the specimens at the frequency of 5 Hz. According to the studies, to maintain adiabatic conditions frequency of the loading should exceed 3 Hz [112, 113]. For femur, the thermoelastic coefficient $K_m = 1.16 \times 10^{-5}$/MPa for the synthetic cortical bone was used based on the cortical density $\rho = 1640$ kg/m^3 [114, 115]. Altair LI software (Cedip Infrared Systems) was used to process the temperature variations. Thermographic data was

acquired after 400 cycles so as to ensure that the body had reached 'quasi' steady state conditions, that is, dynamic loading temperatures had stabilized [116, 117].

Parameters	Values
Spectral Response (Wavelength)	3.6 µm − 5.1 µm
Subwindow	160 x 120 pixels / 80 x 60 pixels / 64 x 8 pixels
Frame Rate	5 Hz to 170 Hz full Frame
Image Capture	Snapshot Integrate then Read mode (ITR)
Number of Pixels	320 x 256 pixels
Pitch	30 µ m x 30 µm
Cooling Type	Integral stirling Cooler
Cooling Time	< 7mn @ 25°C ambient
Frame Rate Resolution	1 Hz step
Resolution	1 MPa
Power Supply	12 VDC / 5A
Power Consumption	50W in cool down mode, 30W in steady state mode
Digital video	USB / Cam LINK
Analogue Video	PAL (50 Hz) or NTSC (60 Hz)
Remote Control	USB / Cam LINK
Overall dimension (mm)	310 x 141 x 159
Weight	3.8 kg
Operational Temperature range	-20°C + 55°C

Table 3.2 Technical data of FLIR SC5000 Silver 420 Camera

IR camera was used to record the surface temperature of the specimen by taking the infrared signals. A 0 – 5V signal, corresponding to the load and frequency, was extracted from the loading machine, filtered and amplified through the signal generator, and input to the IR camera. The system synchronized these IR signals with the loading signals. Lock-in system of the camera

acquired the lock-in reference signal from the loading machine to perform the frequency domain processing of the data. The lock-in system obtained four signal values S_1, S_2, $S_{3 \text{ and }}$ S_4 in every pixel of the image. From these values, the system calculated a phase value (Φ), according to the following basic equation:

$$\Phi = \arctan \left(\frac{S_1 - S_3}{S_2 - S_4} \right) \quad \textbf{(3.1)}$$

Using the Φ values obtained with the above equation, the system produced a phase image. Thermo-elastic stress analysis used in the IR analysis was based on the principle that when a body is compressed, its temperature increases. When the pressure is released, it returns to its original shape and temperature. The thermo-elastic equation used by the camera to generate stress fields is given below:

$$\Delta T = T \, \frac{\alpha}{\rho C_p} \, \Delta\sigma \quad \textbf{(3.2)}$$

Where ΔT is change in the temperature, T is ambient temperature, α is the coefficient of thermal expansion, ρ is the density, C_p is the specific heat capacity, and $\Delta\sigma$ is change in the stress. This equation assumed adiabatic condition i.e. no significant heat loss. The Altair Li uses an algorithm similar to that of the least mean square method to extract the AC signal, that is, the average surface stress, from correlating the dynamic thermal signal and the dynamic reference signal. The DC value of the temperature which corresponds to non-harmonic heating is discarded. Images of anterior, posterior, lateral and medial view respectively were captured using the IR camera.

During the experiments, the IR camera was used to record the oscillating surface temperature of the object by taking a series of IR images, on which every pixel represented the average temperature of the matching spot. The camera generated stress maps while averaging the applied force on the sinusoidal waveform.

3.9   Finite Element Analysis

A 3D model of the Fourth Generation Composite Femur was used which was developed and validated in previous studies [87]. SolidWorks CAD software (SolidWorks Corp., Dassault Systèmes, Concord, MA, USA) was used to modify these models to simulate the two construct designs used in the experimental study. The models were then exported to ANSYS Workbench

version 12(ANSYS Inc., Canonsburg, USA) for the finite element analysis conducted in this study. FE analysis was done at 3000 N applied load. The load of 3000 N represents 4 times body weight for a 75 kg person. The axial stiffnesses for Stage 1 to 4 were calculated by dividing virtual axial load of 3000 N by maximum directional displacement of the force application point on the proximal aspect of the femoral head. The behaviour of FE model was assumed to be linear; therefore, the approach to calculate stiffness was equivalent to using slope of the force vs. displacement graph. The detailed information was entered to simulate the model which resembled the testing procedure followed in the experimental study.

After the initial analysis, the stress maps for Stages 1 to 4 for femur and hip implant, in particularly for femur of Constructs 1 and 2 were examined closely to assess the effect of two different materials and draw comparison between FE analysis and IR thermography.

3.9.1 Synthetic femur, bone plate and hardware

Six distinct combinations of models simulating Stage 1 (intact femur), Stage 2 (femur with hip stem, Stage 3 Construct 1 (injured femur with hip stem and titanium plate), Stage 3 Construct 2 (injured femur with hip stem and carbon/epoxy plate), Stage 4 Construct 1 (healed femur with hip stem and titanium plate) and Stage 4 Construct 2 (healed femur with hip stem and carbon/epoxy plate) were developed. Carbon/epoxy plate was modeled as thin surface to simulate the geometry of a lamina. The bone plates were attached to the simulated femurs shown in Figure 3.12. Bone screws were then applied to secure the bone plate on to the femur model. The combinations of screws and cables were identical to that of the experimental study.

Upon the completion of bone plate assembly, a fracture of 5 mm gap at the femoral mid-shaft was created. All models were evaluated to detect for any interferences between components. This was to ensure the alignment of the femur during simulation. The femur models were considered for two fracture fixation methods incorporating titanium and carbon/epoxy bone plates.

3.9.2 Material properties

The models of periprosthetic femurs fixed with two different types of bone plates consisted of various components made with different materials. The material properties used in the finite element model are discussed in this section.

Synthetic Bone Model

The mechanical properties of the large left Composite Femur were provided by the manufacturer (Pacific Research Laboratories, Vashon, WA, USA). Many prior studies have assumed the behavior of synthetic femurs to be linearly elastic and homogeneous when comparing FE (finite element) and experimental results [77, 81-83]. Since the goal of the current study was to biomechanically evaluate the performance of carbon/epoxy bone plate as a femur fixation method, the same assumption was considered. The material properties of synthetic bone are listed in Table 3.3.

	Cortical Bone	Cancellous Bone
Density (g/cm3)	1.64	0.20
Young's Modulus (GPa)	16.7	0.155
Ultimate Compressive Strength (MPa)	157	6.0
Poisson's Ratio	0.46	0.3
Elasticity Model	Linear elastic	Linear elastic
Isotropy	Isotropic	Isotropic

Table 3.3 Material property of synthetic bone [75, 105]

Bone Plate and Screws

The metal bone plate was made of titanium and screws (both unicortical and bicortical) were made of 316L medical grade stainless steel as provided by Zimmer Inc., USA. The material properties for titanium and 316L stainless steel were obtained from the standardized values provided by the American Iron and Steel Institute (AISI). The range of Poisson's ratio was between 0.220 and 0.346 for the stainless steel in general [60]. For this study, the approximate average value of 0.3 was chosen. The composite bone plate was manufactured by autoclave technique and the material properties for carbon/epoxy resin were provided by the manufacturer Hexcel, USA. The material for composite bone plate was quasi-isotropic; therefore the out of plane properties, in particular shear modulus, young's modulus and poison's ratio were assumed, as the composite was a thin laminate and majority of the load was axial compression in the experimental study. The material

properties of titanium, 316 stainless steel and carbon/epoxy are listed in Table 3.4, Table 3.5 and Table 3.6.

Density (g/cm^3)	4.5
Tensile Ultimate Strength (MPa)	220
Tensile Yield Strength (MPa)	140
Young's Modulus (GPa)	116
Poisson's Ratio	0.34
Elasticity Model	Linear elastic
Isotropy	Isotropic

Table 3.4Material property of titanium[59]

Density (g/cm^3)	8.0
Tensile Ultimate Strength (MPa)	560
Tensile Yield Strength (MPa)	235
Young's Modulus GPa	193
Poisson's Ratio	0.3
Elasticity Model	Linear elastic
Isotropy	Isotropic

Table 3.5 Material property of 316L stainless steel [60, 118]
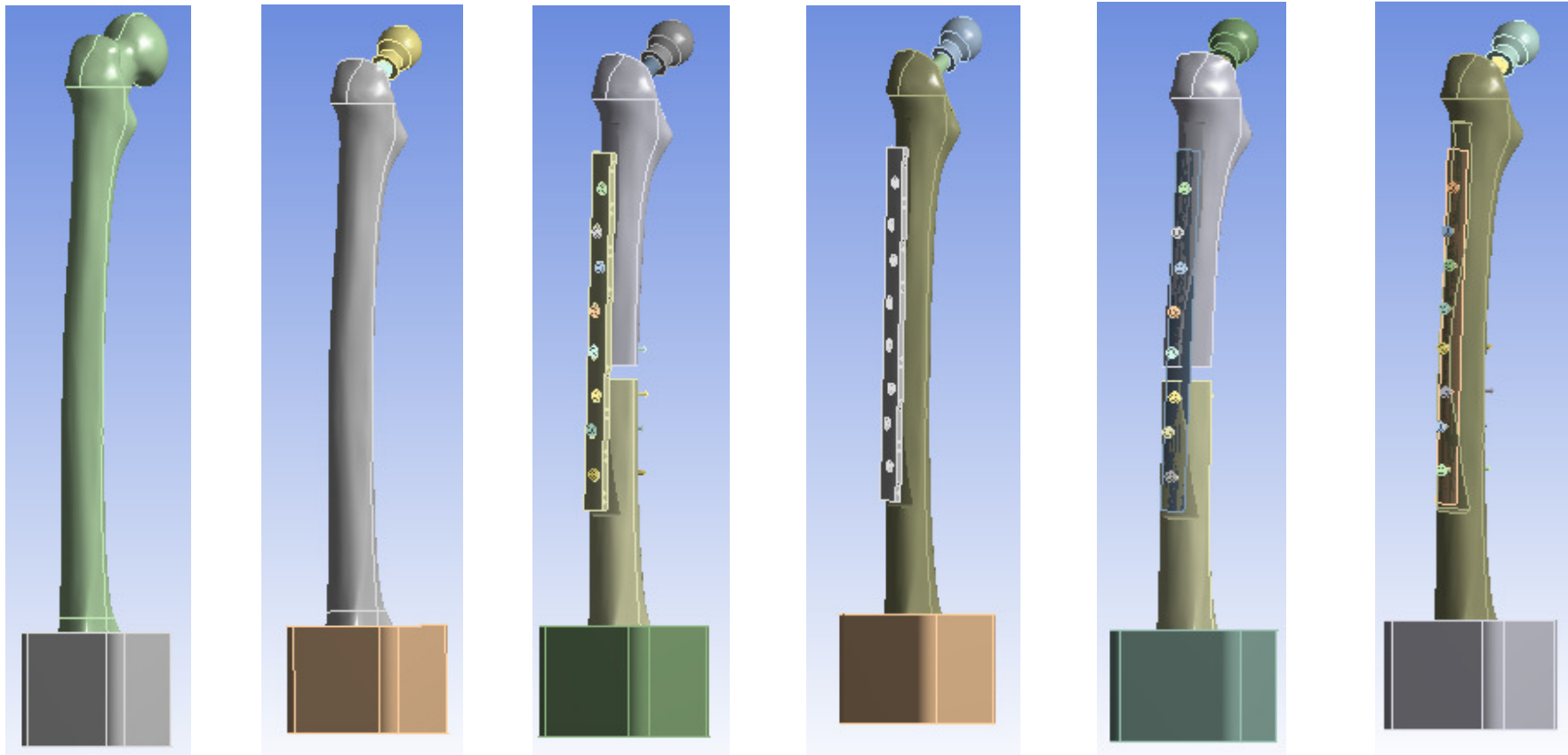
Figure 3.12 Six synthetic femur models: (a) Stage 1 (Intact femur) (b) Stage 2 (femur with hip stem) (c) Stage 3 Construct 1 (injured femur with titanium plate) , (d) Stage 3 Construct 2(healed femur with titanium plate), (e) Stage 4 Construct 1 (injured femur with carbon/epoxy plate), (f) Stage 4 Construct 2 (healed femur with carbon/epoxy plate). Note that all constructs have identical fixation designs proximal and distal to the fracture gap by employing 4 unicortical and 4 bicortical screws respectively.

Hip Stem and Femoral Ball

In this experimental study, hip stem along with the femoral ball, was implanted into the proximal end of femur to simulate total hip replacement (THR). This consisted of a femoral ball commercially called Orthinox™ Head and hip stem, called Exeter™ Femoral Stem. As per manufacturer's manual, both were made of cobalt-chromium-molybdenum (CoCrMo) [70]. Due to its relatively high strength and corrosion resistance CoCrMo alloy is commonly used in hip joint implants [119]. Table 3.7 lists the material properties used in the FE simulation.

Modulus of elasticity, E_{11} (GPa)	142
Modulus of elasticity, E_{22} (GPa)	8.4
Modulus of elasticity, E_{33} (GPa)	8.4
Shear modulus, G_{12} (GPa)	4.6
Shear modulus, G_{13} (GPa)	4.6
Shear modulus, G_{23} (GPa)	3.6
Poisson's ratio, $\nu 12$	0.33
Poisson's ratio, $\nu 13$	0.33
Poisson's ratio, $\nu 23$	0.02
Density (g/cm3)	1.58
Ply thickness (mm)	0.26
Ply orientation	$[90,45,0,-45,90,45,0,-45]_s$

Table 3.6 Material property of Carbon/epoxy resin

Density (g/cm^3)	8.28
Young's Modulus (GPa)	210
Poisson's Ratio	0.31
Yield Strength (MPa)	872
Ultimate Tensile Strength (GPa)	1.172
Elongation to Fracture	12%
Elasticity Model	Linear elastic
Isotropy	Isotropic

Table 3.7 Material property of cobalt-chromium-molybdenum alloy [119-121]

Bone Cement for Hip Stem Implantation

In this experimental study, surgical Simplex P bone cement (Stryker, Mahwah, NJ, USA) was used in order to implant hip stem to mimic periprosthetic femur. The bone cement used was polymethylmethacrylate (PMMA) [89]. Table 3.8 lists the mechanical properties used for PMMA.

Density (g/cm^3)	1.19
Young's Modulus (GPa)	2.45
Poisson's Ratio	0.38
Ultimate Tensile Strength (MPa)	62
Elasticity Model	Linear elastic
Isotropy	Isotropic

Table 3.8 Material Properties of PMMA [122, 123]

Anchoring Block

The square steel chamber with anchoring cement (Flow-stone, King Packaged Materials Company, Burlington, ON, Canada) was used to rigidly fix all the synthetic femurs at their distal end. For flexibility and to simulate experimental conditions as closely as possible, the material property of concrete was applied to the anchoring block. The material property of concrete was taken from the material library that came in ANSYS software (Table 3.9).

Density (g/cm^3)	2.30
Young's Modulus (GPa)	30.0
Poisson's Ratio	0.18
Compressive Ultimate Strength (MPa)	41.0
Tensile Ultimate Strength (MPa)	5.0
Elasticity Model	Linear elastic
Isotropy	Isotropic

Table 3.9 Material properties of anchoring concrete

3.9.3 Elements and Nodes for Finite Element (FE) Modeling

The CAD models of Stage 1, Stage 2, Stage 3 Construct 1, Stage 3 Construct 2, Stage 4 Construct 1 and Stage 4 Construct 2 were imported into ANSYS Workbench 12.0 for finite element analysis (FEA). In order to simulate closely to the experimental scenario, all components accept carbon/epoxy plate were modeled with SOLID 187 tetrahedral elements, having 10 nodes with 3 degrees of freedom at each node. SOLID 187 elements have been used in previous studies and are more optimal then mapped meshing or hexagonal meshing due to their stress stiffening, large deflection and large strain capabilities [62, 124]. For carbon/epoxy plate, SHELL 181 quadrilateral element was used, having 4 nodes with 6 degrees of freedom at each node. It is well suited for modeling of orthotropic thin laminated composites with layered configuration [125]. SHELL 181 has also capabilities of nonlinear analysis that is largely attributed with the analysis of contacts in this study.

3.9.4 Elements for Assembly of components in Finite Element (FE) modeling

The assembly of all components including femur-bone plate, femur-PMMA, femur-screws, femur-cancellous and so on were all done in SolidWorks and the models as a whole, were checked for interference, if any. The models were then exported into ANSYS for finite element analysis. The structural analysis module in ANSYS Workbench, generated contacts automatically between assembled surfaces. CONTA174 is 3D 8 node element that is automatically generated for surface to surface analysis and was used in this study between solid elements. It is used in association with TARGET170, 3D target element and can be used for rigid-flexible and flexible-flexible surface analysis. In this study, all the assembled surfaces except carbon/epoxy plate and cortical bone of femur were modeled with CONTA174 and TARGET170 elements [126]. CONTA175 is a 2D or 3D contact element that can be used between two surfaces, or between a node and a surface or between line and a surface. This element in association with TARGET170 was used to model contact analysis between carbon/epoxy plate and cortical bone [126]. All the contact elements in this study were set to bonded except for the contact surface between bone plate and cortical bone which was set to no separation. The same methods as discussed above have been used in prior studies for FE models involving fracture fixation with total hip replacement [75, 127-130]. Figure 3.13 shows description of some of the contact elements for Stage 3 Construct 2.
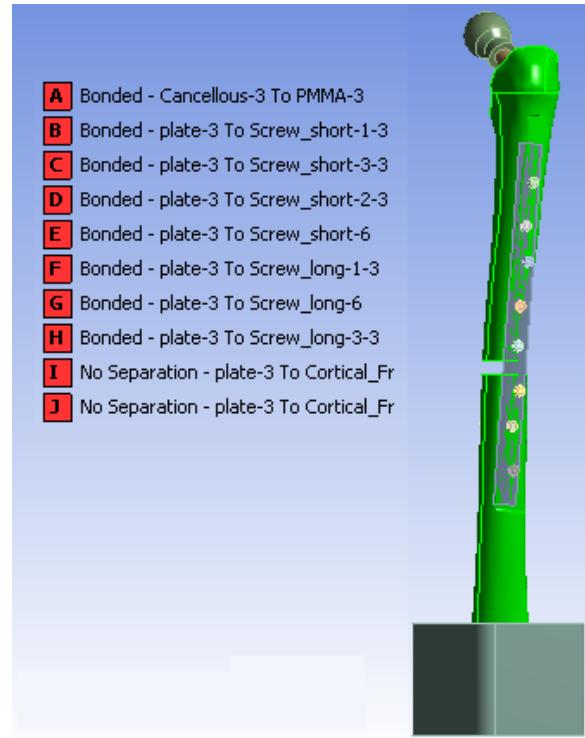
Figure 3.13 Description of contacts used for Stage 3 Construct 2

3.9.5 Boundary Conditions

In order to mimic experimental scenario, anchoring cement block was constrained at 3 faces as shown in Figure 3.14. A force of 3000 N, representing 4 times body weight for a 75 kg person and simulating clinical-level loading analysis was applied to the tip of femoral ball at a 7° angle to replicate the adduction angle used in experiments. The same boundary conditions were used for all models.

3.9.6 Meshing and Convergence

ANSYS used SOLID187 (tetrahedral) elements to generate meshes for Stage 1, Stage 2, Stage 3 Construct 1 and Stage 4 Construct 1. SHELL 181 (quadrilateral) elements to generate mesh for carbon/epoxy bone plate. The results for the mesh were refined using *Relevance* setting in ANSYS Workbench. The mesh relevance for all specimens was set to 80%. Table 3.10 shows the total number of nodes and elements used for Stage 3 and Stage 4. The stress concentrations areas, contributing towards maximum stress, like holes; edges and sharp corners for each specimen were refined by using *Sphere of Influence* tool. Figure 3.15 show the meshing results for Stage 3 and Stage 4 for Constructs 1 and 2 respectively.

45
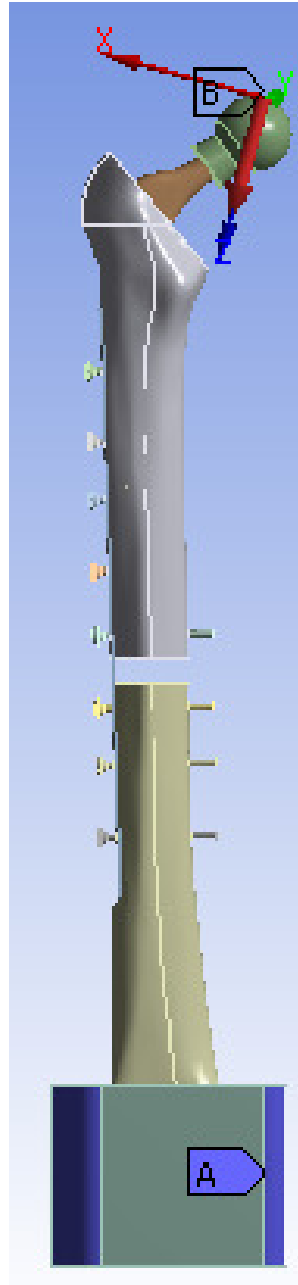
Figure 3.14 Sample boundary Conditions for Stage 3 Construct 2, same for all models

	Specimen Conditions			
	Stage 3 Construct 1	Stage 3 Construct 2	Stage 4 Construct 1	Stage 4 Construct 2
Number of Nodes	115,506	87,380	213,681	110,110
Total Number of Elements	67,489	50,865	200,326	65,739

Table 3.10 Meshing set-up applied to Models for Stage 3 and Stage 4
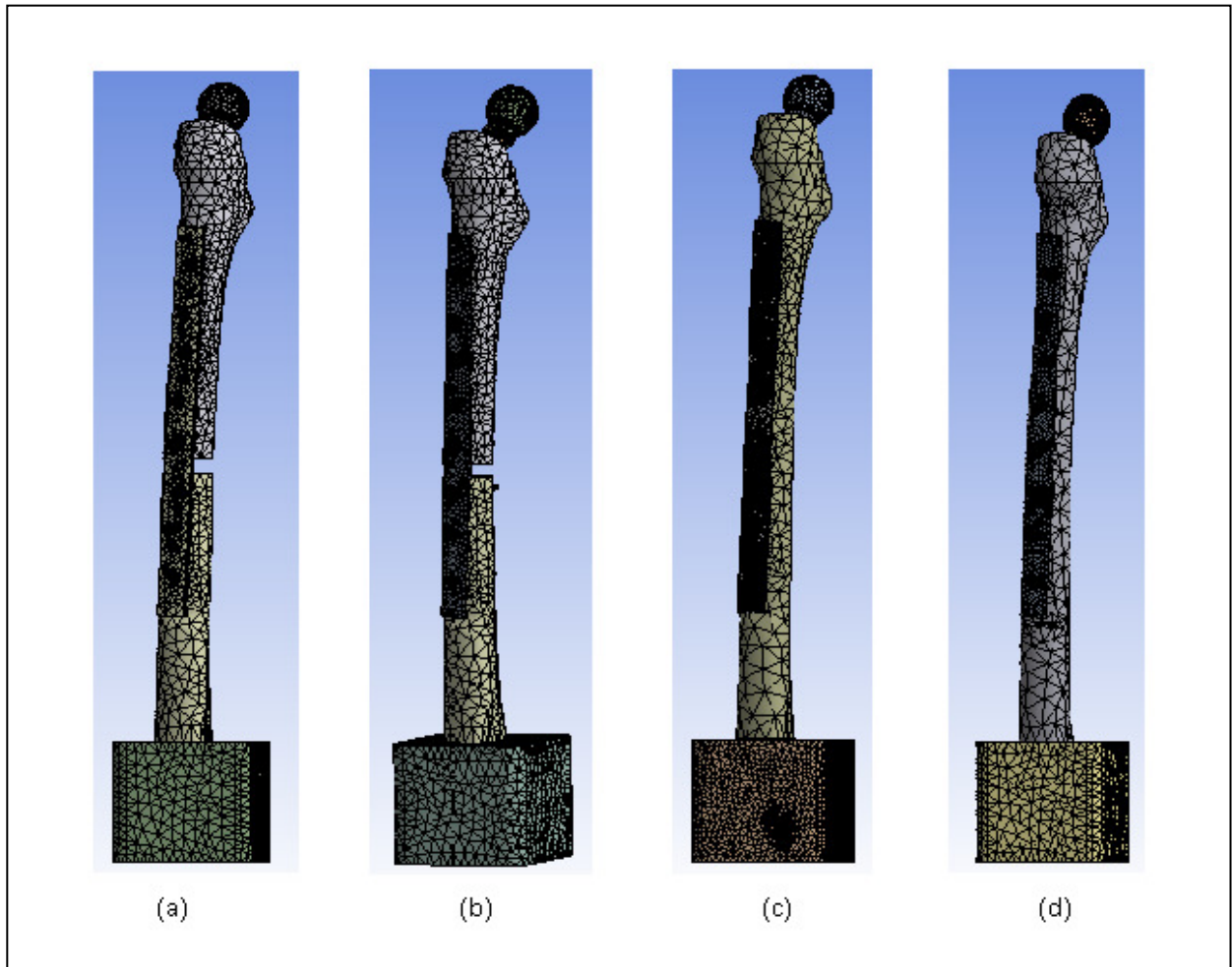
Figure 3.15 Mesh applied to simulation models for (a) Stage 3 Construct 1, (b) Stage 3 Construct 2. (c) Stage 4 Construct 1, (d) Stage 4 Construct 2.

CHAPTER 4. RESULTS

4.1   Axial Stiffness Tests

Stiffness for all the cases was calculated from the graph of force vs. displacement. According to Table 4.1, Static stiffness of Construct 1 level I, an injured femur with metal plate, was 597.6 N/mm (Appendix: A1). Similarly static stiffness of injured femur with composite plate was 532.1 N/mm (Appendix: A2), static stiffness of healed femur with metal plate was 1704.4 N/mm (Appendix: A3) and healed femur with carbon/epoxy bone plate was 1660.3 N/mm (Appendix: A4). Dynamic Stiffness under average load of 800 N for injured femur with metal plate was 697.9 N/mm, injured femur with carbon/epoxy bone plate was 625.3 N/mm, healed femur with metal plate was 2070.4 N/mm and healed femur with carbon/epoxy plate was 2010 N/mm. The loading condition for all the specimens was kept in the linear elastic region to avoid plastic deformation, as can be seen from the value of linearity coefficient R^2, which was above 0.9 for all the cases. Equation 4.1 was used to calculate the difference between static and dynamic stiffness for all the cases. The difference between static and dynamic stiffness for four different conditions is shown in Table 4.1 and the average difference between all these values was 19%.

$$\% Difference = \left(\frac{StaticStiffness - DynamicStiffness}{StaticStiffness} \right) \times 100 \qquad \textbf{(4.1)}$$

Specimen Configuration	Stiffness (N/mm)		% Difference
	Static	**Dynamic Average Load of 800 N**	
Construct 1 Level I (Injured femur with metal plate	597.6	697.9	17%
Construct 1 Level II (Healed femur with metal plate)	1704.4	2070.4	21%
Construct 2 Level I (Injured femur with carbon/epoxy plate)	532.1	625.3	18%
Construct 2 Level II (Healed femur with carbon/epoxy plate)	1660.3	2010	21%

Table 4.1 Axial Stiffness Results

4.2   IR Stress Maps

Error! Reference source not found. shows the IR stress maps for average dynamic loading of 800 N. The injured femurs with metallic plate and composite plate (Construct 1 Level I and Construct 2

Level I) were only investigated by IR thermography. As fractured femur, clinically being the worst case scenario therefore IR thermography investigation was limited Level I specimens only.

Figure 4.1 IR Stress images of injured and healed femur under an average load of 800 N. Stress scale do not include max. or min. stress values.

Stress maps for anterior, posterior, medial and lateral sides for the femur were captured. The images were similar irrespective of the views of femur. The scale of images showed positive and negative values which corresponded to tensile and compressive stresses respectively. The images were captured only for the proximal half of the femur above the fracture line, as clinically, proximal portion of femur is of much interest in the field of biomechanics due to the hip joint. Overall, the proximal portion of the femur experienced tension on the anterior and posterior side. A similar trend was seen on the lateral side as well. However, on the medial side, mostly compressive stresses were observed.

4.3   Comparison of IR stress results for Construct 1 and Construct 2

4.3.1   IR surface stresses synthetic femur

A comparison of IR stress results for Construct 1 and 2 was done to assess the behavior of different constructs under same loading conditions. Five positions on the IR stress maps were probed for anterior, posterior and lateral sides of the femur for both the constructs. Positions on the anterior and posterior side were chosen near the bone plate, in order to investigate the effect of metal and composite bone plates. However, positions on the medial and lateral sides were chosen along the midline. Figure 4.2, shows the positions probed for IR stresses.

Anterior Side
Results for the thermographic stresses for the anterior side are shown in Table A3-1 (Appendix 3). As can be seen from the bar graph, Figure 4.3, for both constructs, stresses experienced by all the positions were in tension. Position 1 near the proximal end of the femur experienced more stress and then steadily decreased from top to bottom until a rapid rise near the fracture site. It was also observed that Construct 2 showed higher stress values at positions probed as compared to Construct 1. Equation 4.2 was used to calculate the difference for each probed position from 1 to 5 between Construct 1 and 2. Table A3-1 shows the calculated difference for each position probed. The overall difference between Construct 1 and 2 for anterior side was calculated to be 24.54 %.
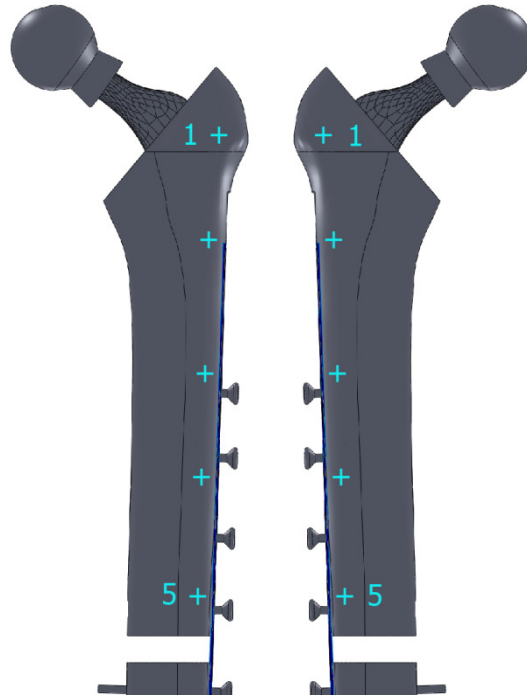
Figure 4.2 Positions probed for anterior and posterior sides of the femur for Construct 1 and Construct 2

$$\% \, Difference = \left(\frac{Construct\ 1\ position - Construct\ 2\ position}{Construct\ 1\ position} \right) \times 100 \quad \textbf{(4.2)}$$
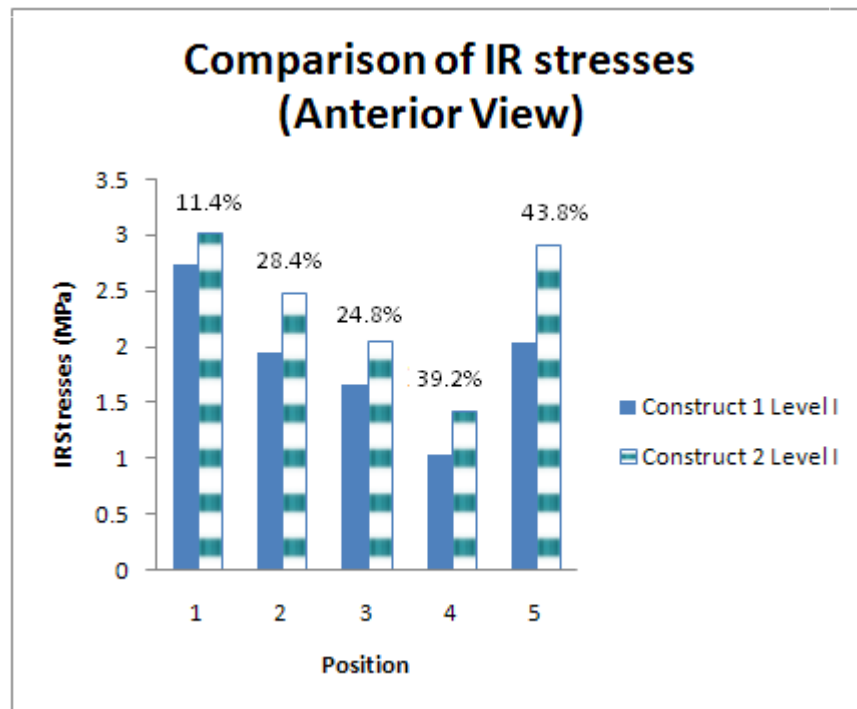
Figure 4.3 Bar Graph with percentage difference for Anterior Surface Stresses for Construct 1 & Construct 2

Posterior Side

In the posterior side the trend was similar to that of anterior side. Results for the thermographic stresses are shown in Table A3-2 (Appendix 3). As can be seen from the bar graph, Figure 4.4, for both constructs, position 1 near the proximal end of the femur experienced more stress and then steadily decreased from top to bottom until a rapid rise near the fracture site. It was also observed that Construct 2 showed higher stress values at positions probed as compared to Construct 1. Equation 4.2 was used to calculate the difference. The difference for each probed position from 1 to 5 between Construct 1 and 2 calculated was 14.6%, 26.9%, 38.4%, 56.6% and 32.9% respectively. The overall difference between Construct 1 and 2 for posterior side was calculated to be 33.88 %.

Figure 4.4 Bar Graph with percentage difference for Posterior Surface Stresses for Construct 1 & Construct 2

Medial Side

The trend was quite different in the medial side as compared to anterior and posterior side. Results for the thermographic stresses are shown in Table A3-3(Appendix 3). All positions experienced compression. As can be seen from the bar graph Figure 4.5, for both the constructs, position 1 near the proximal end of the femur experienced more stress and then steadily decreased from top to bottom. Equation 4.2 was used to calculate the difference. It was also observed that there was not much difference between Construct 2 and Construct 1, for each probed position from 1 to 5 the

difference calculated was -6.8%, 1.3%, -0.9%, 0.3% and 1% respectively. The overall difference between Construct 1 and 2 for medial side was calculated to be -1.02%. In this case, the negative sign indicates that femur with carbon/epoxy experience more stress at point 1 and 3, with maximum difference at point 1 which is close to the distal end of the hip implant.
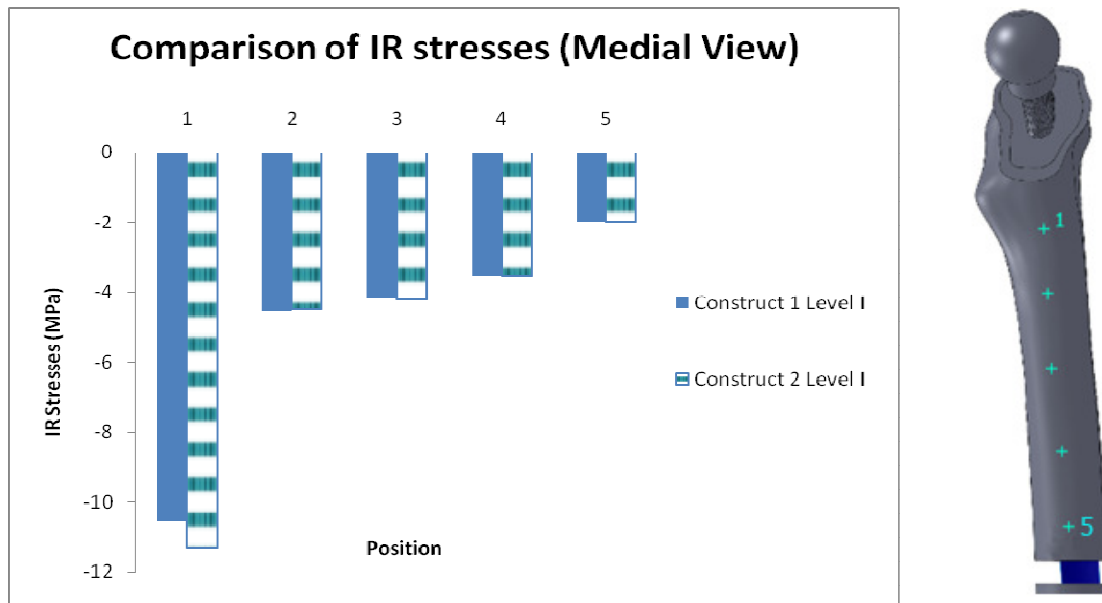
Figure 4.5 (a) Bar Graph for Medial Surface Stresses for Construct 1 & Construct 2 (b) Positions probed

Lateral Side

Results for the thermographic stresses are shown in Table A3-4 (Appendix 3). In this case only 3 positions were probed due to the presence of bone plate. As shown in Figure 4.6(b). All positions experienced tension. As can be seen from the bar graph Figure 4.6(a), for both the constructs, position 1 near the proximal end of the femur experienced more stress and then steadily decreased from top to bottom until a rapid rise near the bone plate. It was also observed that there was not much difference at position 1 between Construct 1 and 2; however the difference increases for position 2 whereas for position 3 there was considerable increase in difference. As shown in Figure 4.6 (a) for Construct 2 near the bone plate femur experienced more stress as compared to Construct 1. Equation 4.2 was used to calculate the difference. The difference for each probed position from 1 to 3 between Construct 1 and 2 calculated was 4.6%, 32.9%, and 41.9% respectively. The overall difference between Construct 1 and 2 for posterior side was calculated to be 26.47 %.

4.3.2 IR surface stresses for Titanium and Carbon/epoxy bone plate

A comparison of IR stresses for titanium and carbon/epoxy bone plates was done to assess the behavior of both the plates under same loading conditions. Six positions on the IR stress maps were probed covering total length of the plates. The positions probed were along the midline of both the plates as shown in Figure A3-1 (Appendix 3).

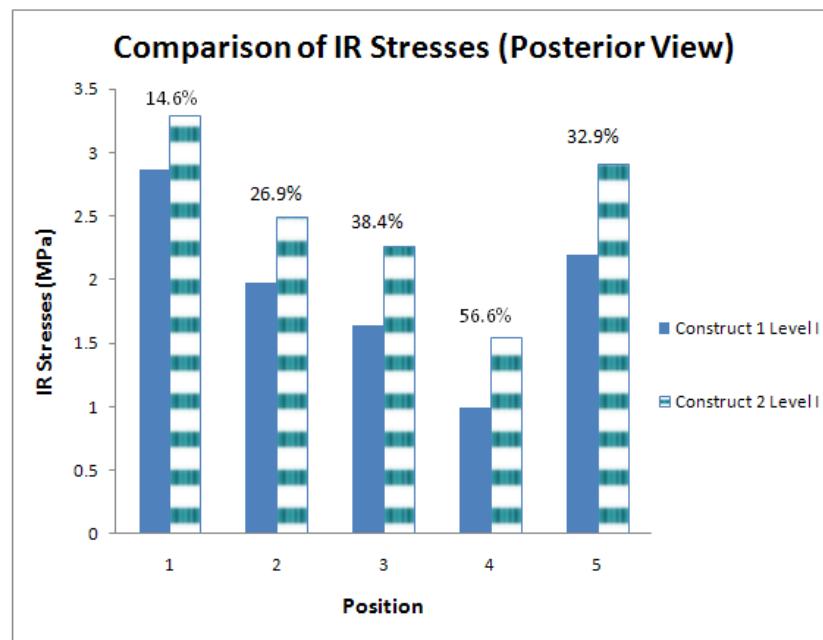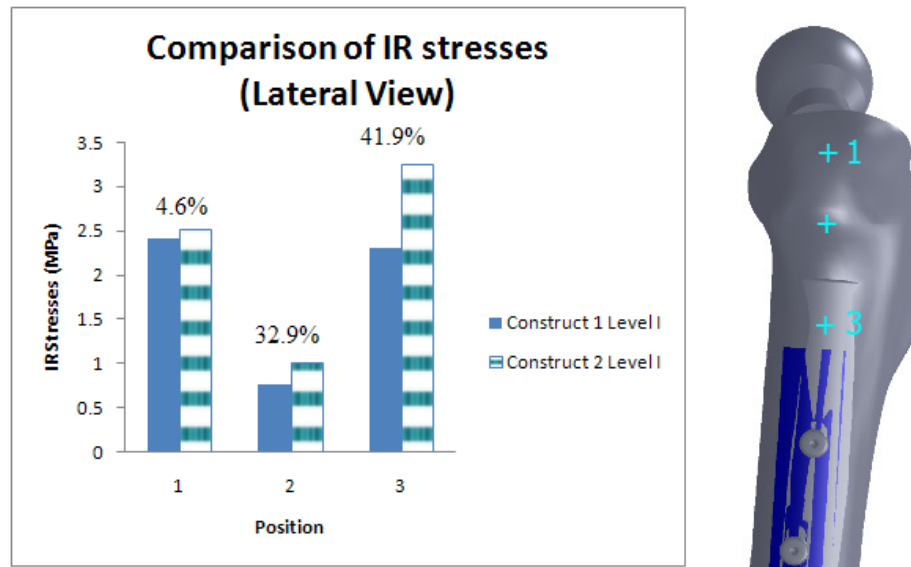**Figure 4.6 (a) Bar graph with percentage difference for lateral surface stresses for Construct 1 & 2, (b) Positions probed**

Results for the thermographic stresses of titanium and carbon/epoxy bone plate for six probed positions are shown in Table 4.2. As can be seen from the bar graph Figure A3-2 (Appendix 3), all positions experienced tension, the pattern of stress distribution was similar in both the plates. IR Stresses steadily increased from the top of the plate near the proximal end of the femur till the mid shaft, where maximum stresses were observed due to the presence of the fracture, and then there was a gradual decrease in IR stresses till the bottom of the plate near distal end of the femur. Equation 4.2 was used to calculate the difference. The difference for each probed position from 1 to 6 between titanium and carbon/epoxy bone plate calculated was 16.6%, 25.6%, 12.3%, 13.8% and 25.7% respectively. The overall difference between titanium and carbon/epoxy bone plate was calculated to be 18.8 %.

	Stresses from IR Camera (MPa)		
Position	Titanium	Carbon/epoxy	% Difference
1	7.33	6.11	16.6%
2	10.41	7.75	25.6%
3	11.04	9.68	12.3%
4	81.33	70.1	13.8%
5	8.22	6.11	25.7%

Table 4.2 Comparison of surface stresses from IR camera for titanium & carbon/epoxy bone plate

4.4   Finite element analysis results

4.4.1   FE Axial stiffnesses at 3000 N

Axial stiffnesses for Stage 1 to 4 calculated at 3000 N of virtual axial load are shown in Table 4.3. As it can be seen, there was a noticeable rise in stiffness from Stage 1 (1553 N/mm) to Stage 2 (1677 N/mm), mimicking a change from an intact femur to a femur with hip stem implantation. This was pursued by a significant decrease to the stiffness of Stage 3 Construct 1 (687 N/mm), simulating a mid shaft femoral fracture in the presence of a hip stem and a fracture metal plate. This followed by a noticeable drop to the lowest overall stiffness value of Stage 3 Construct 2 (610 N/mm), There was an abrupt increase to the highest overall stiffness value of Stage 4 Construct 1 (1965 N/mm), simulating healing of fracture with the metal plate and hip stem. Finally, there was a decrease in the stiffness of Stage 4 Construct 2 (1908 N/mm), mimicking healing of fracture with carbon/epoxy plate. In comparison to Stage 1, there was an increase of 8% for Stage 2, drop of 55.7% and 60.7% for Stage 3 (Construct 1 and 2 respectively) and a rise of 26.5% and 22.8% for Stage 4 (Construct 1 and 2 respectively).

FEA Axial stiffnesses at 3000 N (N/mm)					
Stage 1	Stage 2	Stage 3 Construct 1	Stage 3 Construct 2	Stage 4 Construct 1	Stage 4 Construct 2
Intact femur	Femur with hip stem	Injured femur with metal plate	Injured femur with carbon/epoxy plate	Healed femur with metal plate	Healed femur with carbon/epoxy plate
1553	1677	687	610	1965	1908

Table 4.3 FE Axial stiffnesses for Stage 1 to 4 at 3000 N

4.4.2 FE surface stress maps for the femur at 3000 N

The maximum von mises stresses were determined in the FE analysis for Stage 1 to 4 at 3000 N of axial load applied. The surface stress maps were obtained for femur, implant, bone plate and screws.

Stage 1

The surface stress maps for Stage 1 (Intact femur) for anterior, lateral and medial views are shown in Figure 4.7. There was uniform stress distribution observed throughout femur, in all views with peak stresses at the top of femoral head (point of application of force) and femoral neck in the medial view with a maximum value of 80.7 MPa.
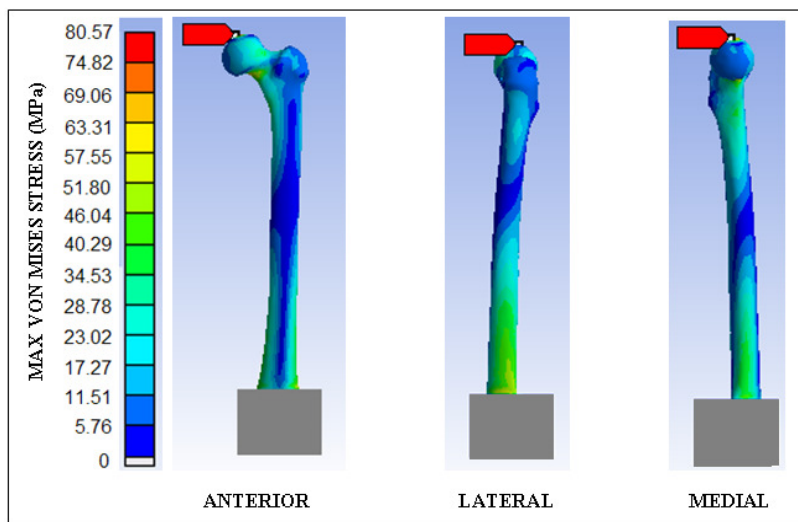
Figure 4.7 Stage 1 surface stress maps (Anterior, lateral and medial views)

Stage 2

In comparison with Stage 1, femur with hip stem, the stress distribution was uniform and showed peak stress value of 30.94 MPa distal to the hip implant near the tip in the medial view. This shows the metal hip implant taking most of the load with stress concentration near its distal end. Figure 4.8 shows surface stress maps for anterior, lateral and medial views.
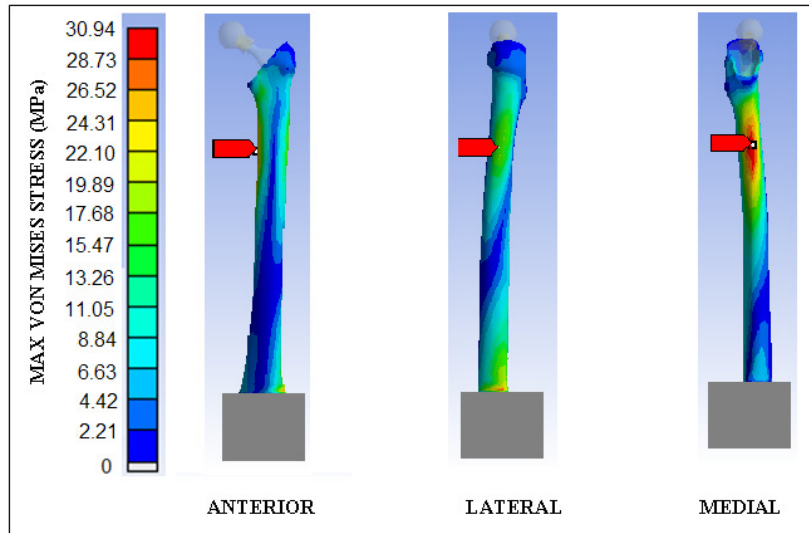
Figure 4.8 Stage 2 surface stress maps (Anterior, lateral and medial views)

Stage 3

In Stage 3(injured femur), there were two construct designs. For Construct 1 (metal plate), there were low stresses observed in the proximal portion of femur above the fracture line, however, peak stresses, with a maximum value of 62.2 MPa, were observed in the distal portion of femur near the end of bone plate in the lateral view. The trend in Construct 2 (carbon/epoxy plate) was similar, but increase in peak stresses, with a maximum value of 101.7 MPa in the distal portion of femur. This increase in peak stresses may be attributed to the load transfer from bone plate to femur in case of carbon/epoxy bone plate. Figure 4.9 and Figure 4.10 shows the surface stress maps for Construct 1 and 2.

Stage 4

In Stage 4 (healed femur), uniform stress distribution was observed in the femur. For Construct 1, peak stresses were observed near the top of the metal plate in the lateral view, however, Construct 2 showed peak stresses near the tip of the hip stem. Figure 4.11 and Figure 4.12 shows the surface stress maps for Construct 1 and 2.
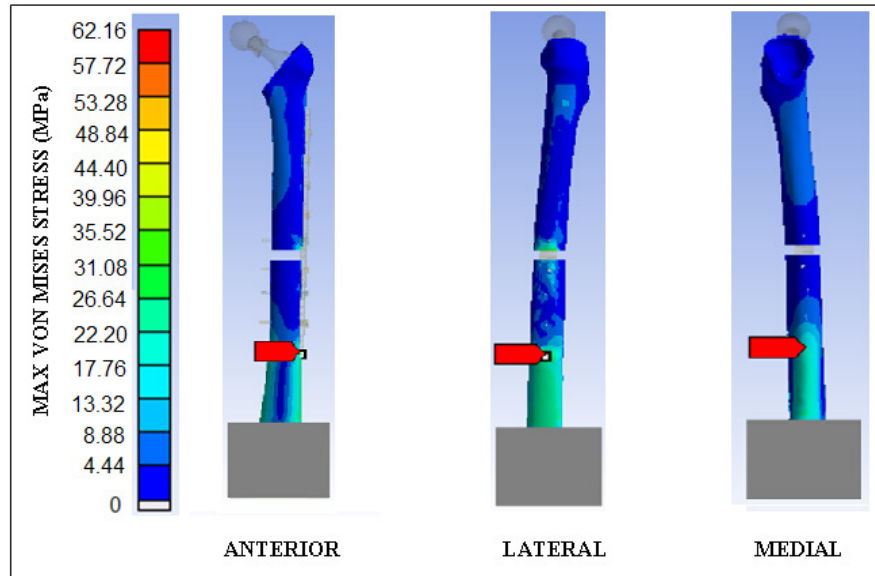
Figure 4.9 Stage 3 Construct 1 surface stress maps (Anterior, lateral and medial views)

In order to evaluate the performance of carbon/epoxy bone plate, Stage 2 (femur with hip stem), was considered as a baseline and it was found that Stage 4 Construct 2 (healed femur with carbon/epoxy plate) showed a decrease of 14.35% in peak stresses.

4.4.3 FE surface stress maps for the hip implant at 3000 N

FE stress maps for the hip implant for Stage 2 to 4 are shown in Figure 4.13. It was observed that the peak stresses for all the stages were found in neck of the hip implant. For Stage 2, peak stress was found to be 471.8 MPa, followed by Stage 3 with 383.6 MPa and 326.2 MPa for Construct 1
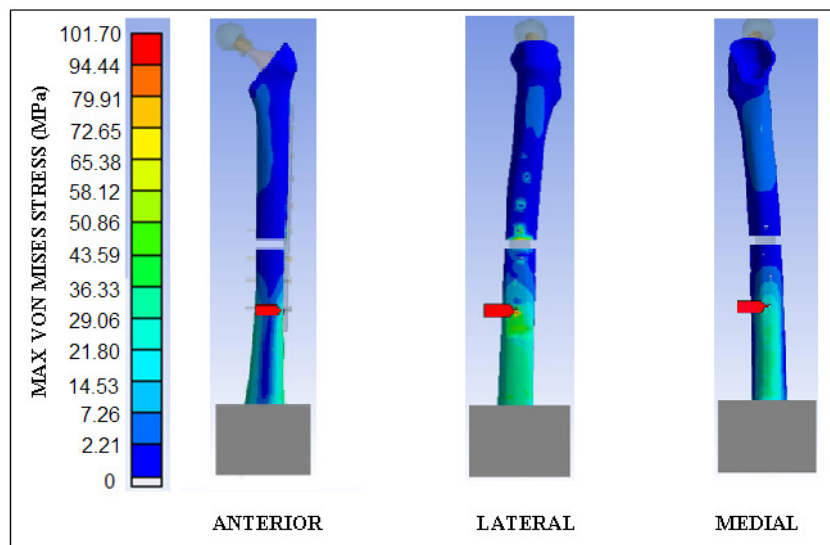
Figure 4.10 Stage 3 Construct 2 surface stress maps (Anterior, lateral and medial views)

58
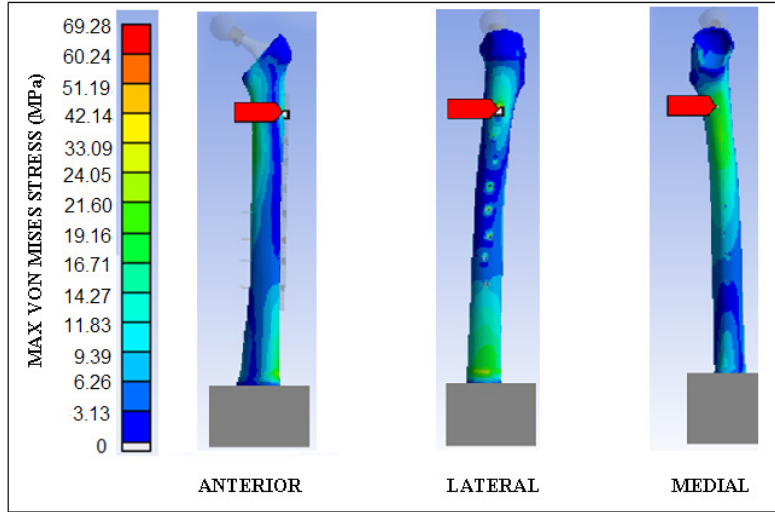
Figure 4.11 Stage 4 Construct 1 surface stress maps (Anterior, lateral and medial views)

and 2 respectively. For Stage 4, it was observed to be 435.8 MPa and 373.8 MPa for Construct 1 and 2 respectively. Equation 4.3 was used to calculate the difference between Construct 1 and 2.

$$\% \, Difference = \left(\frac{Construct \, 1 \, position - Construct \, 2 \, postion}{Construct \, 1 \, position} \right) \times 100 \qquad (4.3)$$

4.4.4 FE surface stress maps for Construct 1 and Construct 2 at 3000 N

Femoral shaft fractures being the worst case scenario, therefore, comparison of Stage 3 (Construct 1 and 2) was done to assess the behavior of different constructs under same loading conditions. Positions probed were similar to as discussed in section 4.3.1 for anterior and posterior sides of the femur.
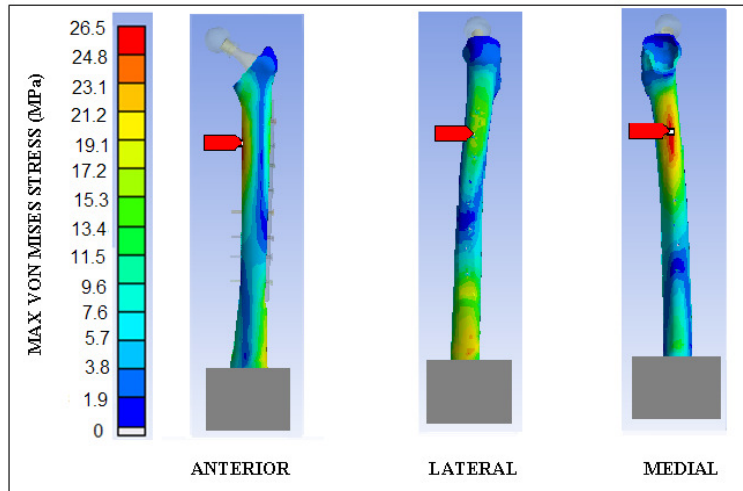
Figure 4.12 Stage 4 Construct 2 surface stress maps (Anterior, lateral and medial views)

59

Anterior Side

Results for the FE surface stresses for the anterior side are shown in Table A4- 1 (Appendix A4). As can be seen from the bar graph Figure 4.14, for both the constructs, stresses experienced by all the positions were in tension. Position 1 near the proximal end of the femur experienced more stress and then steadily decreased from top to bottom until a rapid rise near the fracture site. Since the presence of less stiffness plate, femur of Construct 2 showed a noticeable increase in stresses as compared to Construct1. The difference for each probed position from 1 to 5 between Construct 1 and 2 calculated was 6.5%, 29.5%, 22.7%, 45.6% and 33.5% respectively. The overall difference between Construct 1 and 2 for anterior side was calculated to be 27.6 %.

Posterior Side

The posterior side of femur followed similar stress distribution to that of anterior side. Results for the FE surface stresses are shown in Table A4- 2 (Appendix 4). As can be seen from the bar graph, Figure 4.15 tension was experienced by femur for both the constructs. Position 1 near the proximal end of the femur experienced more stress and then steadily decreased from top to bottom until a rapid rise near the fracture site. In this case also, femur of Construct 2 showed a noticeable increase in stresses as compared to Construct1. The difference for each probed position from 1 to 5 between Construct 1 and 2 calculated was 20.2%, 26.2%, 44.3%, 57.7% and 31% respectively. The overall difference between Construct 1 and 2 for anterior side was calculated to be 35.9 %.
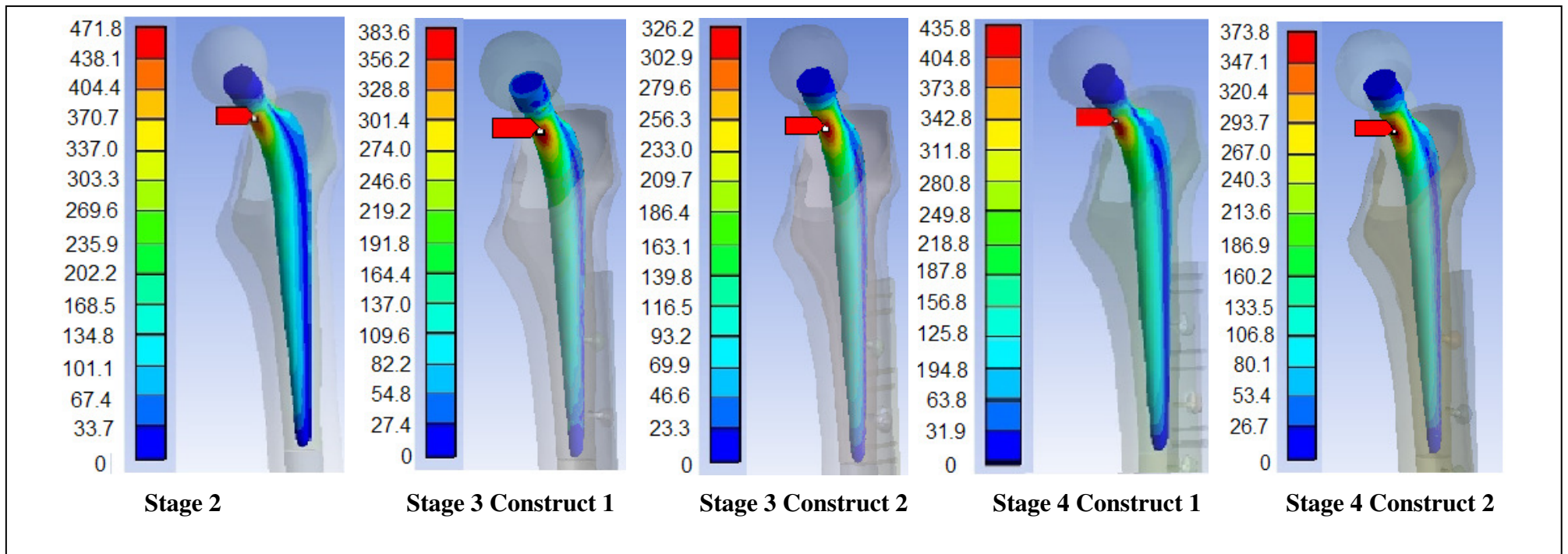
Figure 4.13 Surface stress maps of hip implant (Stage 2 to 4)

The figure shows five stress map columns labeled:

Stage 2	Stage 3 Construct 1	Stage 3 Construct 2	Stage 4 Construct 1	Stage 4 Construct 2

Stage 2 scale values:
471.8, 438.1, 404.4, 370.7, 337.0, 303.3, 269.6, 235.9, 202.2, 168.5, 134.8, 101.1, 67.4, 33.7, 0

Stage 3 Construct 1 scale values:
383.6, 356.2, 328.8, 301.4, 274.0, 246.6, 219.2, 191.8, 164.4, 137.0, 109.6, 82.2, 54.8, 27.4, 0

Stage 3 Construct 2 scale values:
326.2, 302.9, 279.6, 256.3, 233.0, 209.7, 186.4, 163.1, 139.8, 116.5, 93.2, 69.9, 46.6, 23.3, 0

Stage 4 Construct 1 scale values:
435.8, 404.8, 373.8, 342.8, 311.8, 280.8, 249.8, 218.8, 187.8, 156.8, 125.8, 194.8, 63.8, 31.9, 0

Stage 4 Construct 2 scale values:
373.8, 347.1, 320.4, 293.7, 267.0, 240.3, 213.6, 186.9, 160.2, 133.5, 106.8, 80.1, 53.4, 26.7, 0

61

Figure 4.14 Bar Graph with percentage difference for Anterior Surface Stresses for Construct 1 &Construct 2
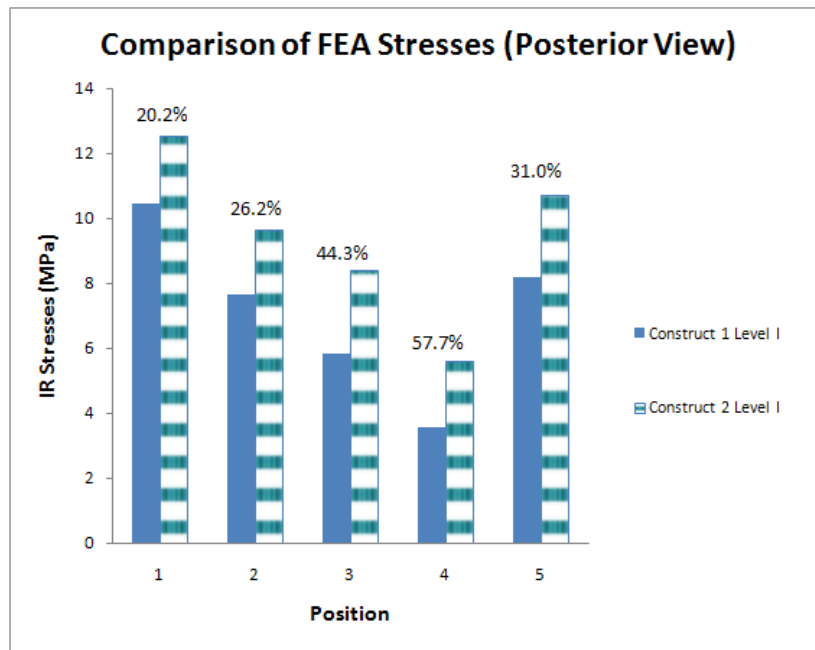
Figure 4.15 Bar Graph with percentage difference for Posterior Surface Stresses for Construct 1 & Construct 2

4.5   Validation of the Finite Element Model

4.5.1   Evaluation of Axial static stiffness values

The axial static stiffness values predicted by the finite element model were compared to the experimental static stiffness results to determine whether the finite element analysis software can be used to predict the axial static stiffness of particular construct. Results are shown in Table 4.4.

		Axial Static Stiffness (N/mm)	
		Construct 1	Construct 2
Level I	Experiment	597.6	532.1
	FE	687	610
	Difference	13%	12.8%
Level II	Experiment	1704.4	1660.3
	FE	1965	1908
	Difference	13.3%	12.9%
$\%Difference = \left(\dfrac{FE\ Stiffness - Experimental\ Stiffness}{FE\ Stiffness}\right) \times 100$			

Table 4.4 Comparison of predicted and measured axial static stiffness values

The finite element analysis software predicted the axial static stiffness of Level I and Level II for Construct 1 and 2 to within 13% of the experimental results. The axial static stiffness predicted by the finite element model was slightly overestimated, but overall appeared in good agreement with majority of the observed experimental data Therefore the finite element model appears to have been successful in predicting the stiffness of the constructs for all levels. Possible explanations for the high measured stiffness in all levels are examined later in the discussion section.

4.5.2   Comparison of IR stress maps with FEA stress maps

The comparison between IR and FEA stress maps for Level I (injured femur) for the anterior and posterior sides is shown in Table 4.5 and Table 4.6 respectively. Assuming linear behavior of FEA model, the FEA stress maps were reduced linearly from calculated value of 3000 N to 800 N for comparison with IR stress maps. It can be seen that FE model compared reasonably well with the IR stress maps.

$$\% \, Difference = \left(\frac{IR \, Stress - FEA \, Stress}{IR \, Stress} \right) \times 100 \qquad (4.4)$$

	Comparison of IR and FEA stress maps (Anterior Side)					
	IR Stresses (MPa)	FEA Stresses (MPa)	% Difference	IR Stresses (MPa)	FEA Stresses (MPa)	% Difference
Position	Construct 1 Level I	Construct 1 Level I		Construct 2 Level I	Construct 2 Level I	
1	2.72	2.81	3.48	3.03	3.00	1.03
2	1.94	1.97	1.80	2.49	2.56	2.71
3	1.65	1.55	5.87	2.06	1.91	7.49
4	1.02	1.01	1.31	1.42	1.47	3.20
5	2.03	2.23	9.87	2.92	2.98	2.00

Table 4.5 Comparison of IR and FEA stress maps (Anterior Side)

	Comparison of IR and FEA stress maps (Posterior Side)					
	IR Stresses (MPa)	FEA Stresses (MPa)	% Difference	IR Stresses (MPa)	FEA Stresses (MPa)	% Difference
Position	Construct 1 Level I	Construct 1 Level I		Construct 2 Level I	Construct 2 Level I	
1	2.87	2.78	2.98	3.29	3.35	1.72
2	1.97	2.04	3.45	2.5	2.57	2.90
3	1.64	1.56	5.13	2.27	2.25	1.09
4	0.99	0.95	4.26	1.55	1.49	3.56
5	2.19	2.18	0.50	2.91	2.85	1.91

Table 4.6 Comparison of IR and FEA stress maps (Posterior Side)

Equation 4.4 was used to calculate the difference. It can be seen from Table 4.5 and Table 4.6 that the FEA stress maps are in good agreement with IR stress maps. However, explanation of the results is done in discussion section.

CHAPTER 5. DISCUSSION

5.1 General Findings from Current Study

This study evaluated the mechanical performance of a quasi-isotropic carbon/epoxy laminate (T700-M21) by comparing it to a commercially available metallic bone plate known as Zimmer, in an injured (femoral mid shaft fracture of 5 mm) and healed femur in the presence of a total hip stem. Lock-in infrared thermography was implemented to generate a comprehensive three-dimensional surface stress mapping of two synthetic femurs under cyclic axial loading conditions. For the worst case scenario, only Level I (injured femur) with Construct 1 (metal plate) and Construct 2(carbon/epoxy plate) was investigated with IR thermography. The results showed that the femur of Construct 2 experienced more stresses as compared to Construct 1 with an overall difference of 29.2% in the anterior and posterior sides that is accounted for because carbon/epoxy is less stiff than titanium. This is the first study that tries to comprehensively evaluate the performance of an injured femur with two different bone plate designs, using lock-in thermography and comparison with FEA analysis.

5.2 Comparison of Current Results with Previous Studies

There are no prior studies of carbon/epoxy bone plate as a method of femoral shaft fixation in the presence of the hip stem. However, there are several studies on synthetic femurs with different fracture fixation methods; the following points of comparison are worth noting.

5.2.1 Axial Stiffness

Present FE axial stiffness for Stage 1, 1553 N/mm, was similar to prior experimental studies on intact synthetic femurs in a range of 1290 N/mm to 1900 N/mm [62, 131-134]; but higher than intact human femurs ranging from 757 to 1360 N/mm [62, 69]. FE axial stiffness of Stage 2, 1677 N/mm, was much lower than one study of synthetic femur with a total hip stem yielding 3160 N/mm [132]. The experimental average static axial stiffnesses of Level I for metal and carbon/epoxy bone plates of 597.6 N/mm and 532.1 N/mm compared reasonably well to an earlier study that achieved in a range of 500 N/mm to 1000 N/mm [132], and much lower than one study that achieved 1110 N/mm [103]. However, studies reveal that axial stiffness from a variety of other similar plated periprosthetic fixations in synthetic and human femurs can range from 304 to

5000 N/mm [103, 104, 135, 136]. The experimental average dynamic axial stiffness for Level I for Construct 1 and 2 of 697.9 N/mm and 625.3 N/mm compared well with one study that achieved in a range of 600 – 800 N/mm [132] and higher than one study that achieved 464 N/mm and 390 N/mm [137]. However, there are no prior studies for experimental axial stiffnesses of healed periprosthetic fractures using plate fixation. As a baseline, experimental static average axial stiffness of 1660.3 N/mm, Level II (healed femur) with carbon epoxy plate was higher as compared to previous experimental average data for synthetic femurs as well as human cadaveric femurs. The studies revealed values of synthetic femurs with hip stem in a range of 1230 N/mm to 1543 N/mm [62, 70, 71, 131, 133, 138]. Although, for one study of an intact synthetic femur with the same material properties, the average static axial stiffness calculated was 1347.9 N/mm, which was 23.2% lower than carbon/epoxy plate. This difference may be attributed to the presence of hip stem and carbon/epoxy bone plate as compared to the intact synthetic femur [139]. The differences in results are attributed to variations in experimental conditions, such as proximal load application method, distal fixation method, femur orientation, material properties, and so forth.

The overall experimental dynamic axial stiffness was at an average of 19% greater compared to that of overall axial static stiffness (Table 4.1). There are no prior studies to report the changes in static to dynamic loading based on current loading conditions. In one study, carried out on human cadaveric femurs, it was observed that dynamic stiffness was higher than static stiffness by about 20% [140]. However, the difference in axial static and dynamic stiffnesses is attributed to the increase in loading rate from static to dynamic loading and shows the viscoelastic nature of synthetic femurs [42].

5.2.2   IR Stress Maps

There are no prior studies that have investigated similar stress patterns under the same loading conditions for injured femurs with hip stem. However, stress patterns for an average dynamic load of 800 N seem to agree significantly with one prior study of an intact synthetic femur along the anterior and posterior areas of the proximal femur, especially with respect to the femoral shaft, where stresses were seen in tension which decreased steadily along the femoral shaft for Level I (injured femur for Construct 1 and 2) [139]. IR surface stress maps of Level I for Construct 1 and

2(Figure 4.3 and Figure 4.4) agree significantly with FEA stress maps for the anterior and posterior sides (Figure 4.14 and Figure 4.15). This confirms that carbon/epoxy bone plate experiences less stress than metal plate resulting in more load transferred to the femur, which can obviously increase compressive stresses, reduce bone resorption and hip implant loosening.

In the current study, the pattern of stresses for both the constructs were the same, and the highest stresses were seen in the medial and posterior region of the femur as seen from Figure 4.4 and Figure 4.5 and the maximum stress was recorded in the medial region near the proximal end of the femur. This could be attributed to the fact that bone plate in both constructs shared some load which is why the proximal portion of the femur experienced compressive stress. For the posterior side, the presence of peak stresses is due to the fact that the axial loading is not the only type of force present during the dynamic load [62]. Further investigation is required, as no prior studies suggest this phenomenon.

5.3 Clinical and Practical Implications

Stress shielding was related to changes in overall experimental axial static stiffness for Level I (injured femur) for Construct 1 and 2. According to stress shielding theory, high stiffness metal implants carry an increased proportion of stresses as compared to what bone carries thus lowering stresses on the femur and increasing the chances of bone resorption leading to implant loosening [141, 142]. Going from Construct 1 to Construct 2 (Level I), there was a drop in static stiffness of 11% (Table 4.1) followed by an overall difference in IR surface stresses for femur (Level I) of 29.2% (Figure 4.3 and Figure 4.4) in the anterior and posterior sides and an overall difference of 25.48% between IR stresses for titanium and carbon/epoxy bone plate (Table 4.2). It was observed that femur of Construct 1(Level I) carried decrease proportion of stresses to what femur of Construct 2 (Level I) carried. Similarly, metal plate carried increased proportion of stresses to what carbon/epoxy plate carried. This can be attributed to increase in amount of stress shielding for metal plate compared to carbon/epoxy plate. Similar trend for stress shielding was seen in FEA analysis as well. Going from Stage 3 Construct 1 to Stage 3 Construct 2, there was a drop in axial static stiffness of 11% (Table 4.3) followed by an overall increase in peak bone stresses of 64% after replacing titanium plate with carbon/epoxy bone plate (Figure 4.9 and Figure 4.10). It was observed that femur of Construct 1 carried decrease proportion of stresses to what femur of

Construct 2 carried. This can be attributed to metal plate carrying increased proportion of load as compared to carbon/epoxy plate, resulting in an increase in amount of stress shielding for metal plate compared to carbon/epoxy plate.

In this study a metal hip stem was used and had increased stress shielding compared to the composite bone plate. The composite plate, just like a prior composite hip implant, has shown promising results that replicates the performance of the natural femur better than the standard metallic hip implants. A previous study on a hip stem made from a composite CF/PEEK (Carbon Fibre-Reinforced Polyether-Ether-Ketone) and a previous investigation on the same composite hip stem examined currently [148, 149] showed that these materials can potentially reduce stress shielding by increasing the load transfer to the host femur in comparison to metallic hip implants. This also confirmed that the composite hip stems absorbed less stress than the metallic hip stems. As a result, more loads would be transferred to the host femur, which can obviously reduce bone resorption and subsequent implant loosening.

The IR stress maps for both the constructs showed maximum peak stress in the femur, near the tip of the metal hip implant as seen in the medial view (Figure 4.5Figure 4.2 and Table A3-3), which may greatly increase the risk of bone fracture in this area [8, 47, 143-145]. The FEA stress maps suggest that stress fracture for Stage 2, femur with hip stem, has a high probability of occurring near the tip of metal hip implant (Figure 4.8). Similarly for Stage 4 Construct 2, the peak stresses were observed in the proximal portion of femur near the tip of the hip implant (Figure 4.12), which greatly increased the risk for bone fracture in this area. In both the cases, the region near the tip of the hip implant is prone to fracture failure. Clinically, the poor bone stock arising from severe osteopenia or osteoporosis may not permit the hip implant to be anchored firmly, thereby causing the site of implant failure, loosening, or migration to be in the distal region where the implant is in direct contact with the bone.

The application and use of IR thermography in the field of biomechanics has been validated by strain gauge measurements in number of studies [139, 146]. Therefore, IR thermography has the capability of providing accurate measurements and can be used in isolation without strain gauges in biomechanical testing of synthetic bones undergoing dynamic loading conditions [147].

The major benefits of IR thermorgraphy include that it is a non destructive technique and therefore does not damage the surface of the testing specimen. It can be easily used in isolation, once the specimen is calibrated experimentally using strain gauges, and it has the ability to generate a full three-dimensional stress map simulating actual experimental loading conditions which is not possible with strain gauges unless every point on the surface is covered. The other benefits include minimal setup and testing time and the testing of specimens is done under cycling loading conditions depicting real life clinical conditions that bones experience. However, IR stress maps may not remove completely the requirements for FEA, but could provide assistance for biomechanical researchers in refining and improvement of orthopaedic devices. Specifically, IR thermography can measure surface stresses, but FEA can also obtain sub surface stresses in the interior of an object.

5.4   Limitation/Sources of Error and Future Work

Only the proximal portion of the femur was imaged using IR thermography. However, in the biomechanical studies of hip joints, proximal portion of the femur is of great interest; therefore, the IR camera captured images of the proximal region of femur only. Camera can be positioned to provide a complete map of the femur to investigate the stresses in the distal end of the femur. In this study, sinusoidal loads were applied with an average load of 800 N, simulating one times the BW of a person and for a limited number of cycles. This was to ensure no permanent damage occurred and all surface views can be captured at all load levels. However, using increased cyclic loads at an average load of up to 3 or 4 times BW can be applied to simulate a full clinical level scenario.

Strain gauges were not used in this study to validate the results of IR thermography, however, strain gauges can only provide local stress and strain, and therefore, other experimental techniques should be used for comparison of results for IR thermography. Techniques such as brittle coating, photoelastic coating, and ultrasound techniques and so on can be used to measure measured experimental stresses [150, 151].

A synthetic, rather than a cadaveric femur, was used. Synthetic femurs are easier to obtain, less expensive, environmental friendly, easier storage and above all reduced specimen-to-specimen variability in physical properties [69, 152]. They have also shown similar results for cortical and cancellous screw pullout stress relative to human femurs, as well as having potential failure patterns

at the neck when tested intact or with a hip stem [66, 68, 153-155]. There are many studies in which synthetic femurs were used for fixation of femoral shaft fractures, but prior validation against cadaveric femurs did not included total hip implants or fracture plates [75, 82, 131-133].

In the FE analysis, the model for the synthetic femur was assumed to be linear and isotropic. This may not truly simulate human femur, which is non-linear, anisotropic, and visco-elastic. The use of cadaveric femurs may have provided a more realistic evaluation. However, prior studies have effectively used linearly isotropic FE models of long bones with respect to experiments on synthetic and human bones [19, 62, 75, 82, 128, 129].

IR thermography has been incorporated by several studies in analyzing stress patterns on human bones. However, due to limited advances in thermographic technology, qualities of images were poor and inconsistent [114].

In the current study, dynamic loading was carried out at 5Hz because adiabatic conditions can be achieved with a frequency greater then 3Hz. However, in biomechanical studies, normal human walking gait is often replicated as using frequencies between 1 to 3Hz [42, 156-157]. The use of higher frequency may result in increase in the magnitude of stresses measured on the surface of the femur.

The specimens used in experimental tests were limited to linear elastic limit. Fatigue failure should also be considered in order to understand more comprehensively the behavior of synthetic femurs and bone plates under dynamic loading conditions simulating long-term use by a patient.

Only two synthetic femurs were tested for the current study which could be increased to a number of specimens so that a more thorough statistical comparison could be carried out. However, the aim of current study was not to asses specimen-to-specimen variability among synthetic femurs, but to evaluate the performance of carbon/epoxy bone plate in an injured and healed femur using same synthetic femur and comparing it to another synthetic femur with metal plate. Moreover, similar prior studies have also used single specimen strategy [87].

The FEA model as compared to experimental results, predicted an increase in axial static stiffnesses for Level I and Level II of about 13% (Table 4.4). This may be attributed to the effect of slippage in

experimental analysis. However, the value of coefficient of correlation (R^2) was higher than 0.9 for all tests, this showed that model remained within linear elastic limit.

The femoral head of the implant was covered with tape so that slippage could be avoided between the rectangular cup indenter and the femoral head when load was applied by the Testresources machine. However, the presence of peak stresses on the posterior side, can be due to the twisting and bending forces on the femoral ball, and may be due to the effect of slippage, which can be minimized but cannot be eliminated. The acetabular cup indenter could have been used to avoid slippage, as the prior studies have used the same geometry to minimize slippage [139, 146].

The FEA stress maps showed a good agreement with IR stress maps (Table 4.5 and Table 4.6) and can be a good tool in validating IR results. However, though the stress maps for IR and FEA were similar, but the nature of loading was different in both the cases. IR stress maps were due to cyclic loading and the other due to static loading. IR stress maps were three dimensional; whereas FE stress maps were two dimensional. So comparison in this case cannot be justified. FEA with cyclic loading may have justified this scenario.

CHAPTER 6. CONCLUSION

The present study used IR thermography and finite element analysis (FEA) for the evaluation of carbon fibre/epoxy plate as fracture fixation method to minimize stress shielding and bone resorption.

IR thermography was used to produce three dimensional stress maps of Level I (injured femur) and Level II (healed femur) under cyclic loading reflecting the walking gait cycle of healthy human subjects. For Level I, Construct 1 (metal plate), representing the immediate post surgical scenario, yielded high stiffness and femur experienced relatively less stresses as expected. This attributed to the fact that the metal plate carried most of the load due to "stress shielding". Femur of Level I Construct 2 yielded low stiffness and high bone stress as compared to Construct 1. At Level II, healed femur showed similar pattern but an overall substantial rise in stiffness for both the constructs. It was observed that overall dynamic stiffness values for all specimens were significantly higher as compared to static stiffness values, with an overall difference of 19%. The analysis of the two fracture fixation methods incorporated both static and dynamic conditions, simulating standing and walking/running activities of humans.

FEA analysis provided a more realistic clinical approach by observing the effect of 3000 N axial load on synthetic femur. FEA incorporated a quantified approach analyzing stress maps for an intact femur through to full fracture healing followed by a femoral mid shaft fracture in the presence of a total hip stem. At Stage 1, the intact femur, experienced peak stresses proximal to the femoral head with a uniform stress pattern. Stage 2 and Stage 3, showed the effect of stress shielding, as metal hip stem, metal plate carried most of the load. For Stage 4, the femur with metal plate experienced low stresses due to the effect of stress shielding.

This study also highlighted the adverse effect of high stresses during entire surgical process from intact stage to the fracture healing stage.

APPENDICES

APPENDIX 1: Static Stiffness Tests

Figure A1-1 to Figure A1-4 shows static stiffness graphs for different Construct 1 and 2. Stiffness for all these specimens were obtained from an average of three tests. The numerical values shown on the axes are based on the Testresources testing machine's coordinate system. The value of R^2 shows the degree of linearity and the equation gives the slope and the intercept of the line. Results indicate that there was a good correlation between experiments and line of best fit.
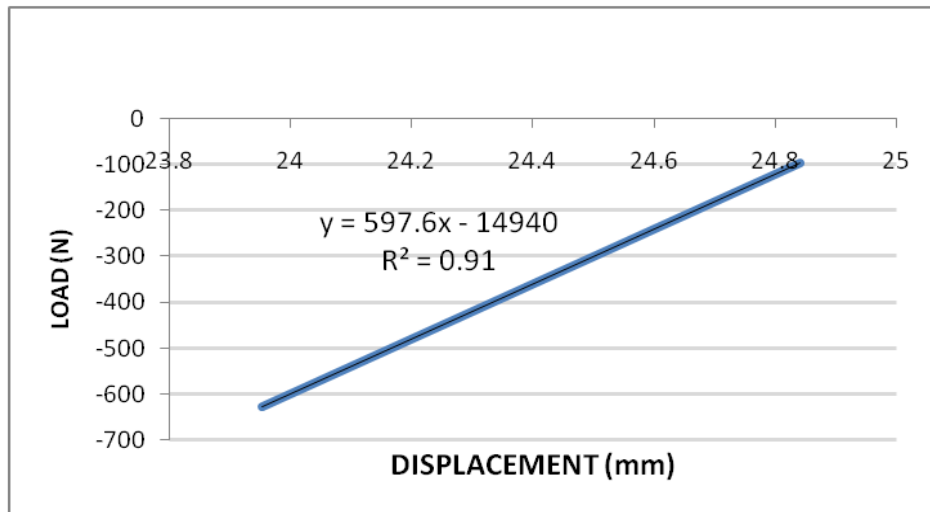
Figure A1-1 Static Stiffness Construct 1 Level I
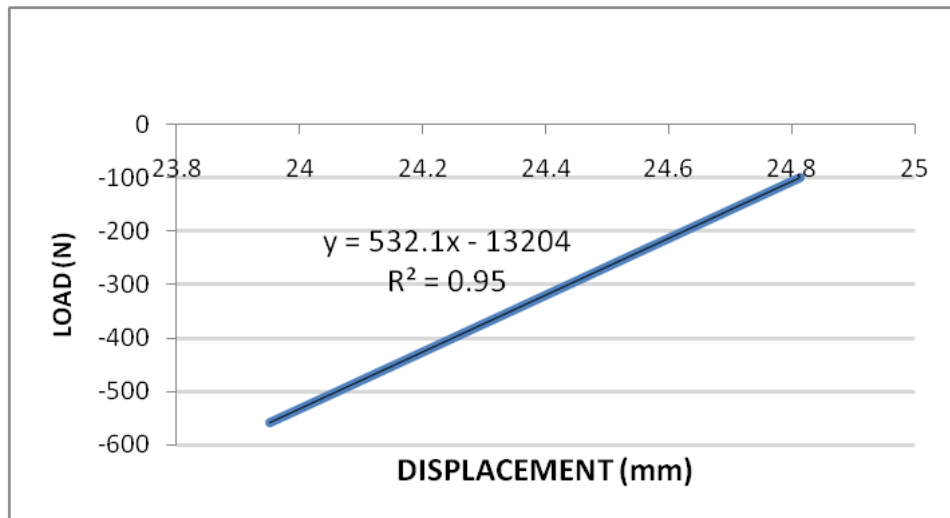
Figure A1 2 Static Stiffness Construct 2 Level I
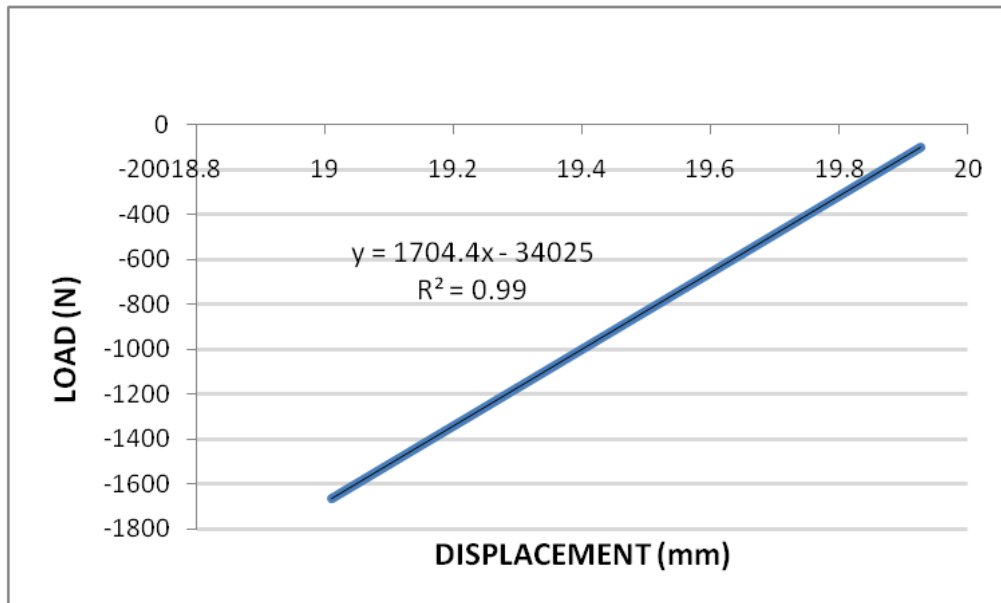
Figure A1-3 Static Stiffness Construct 2 Level II
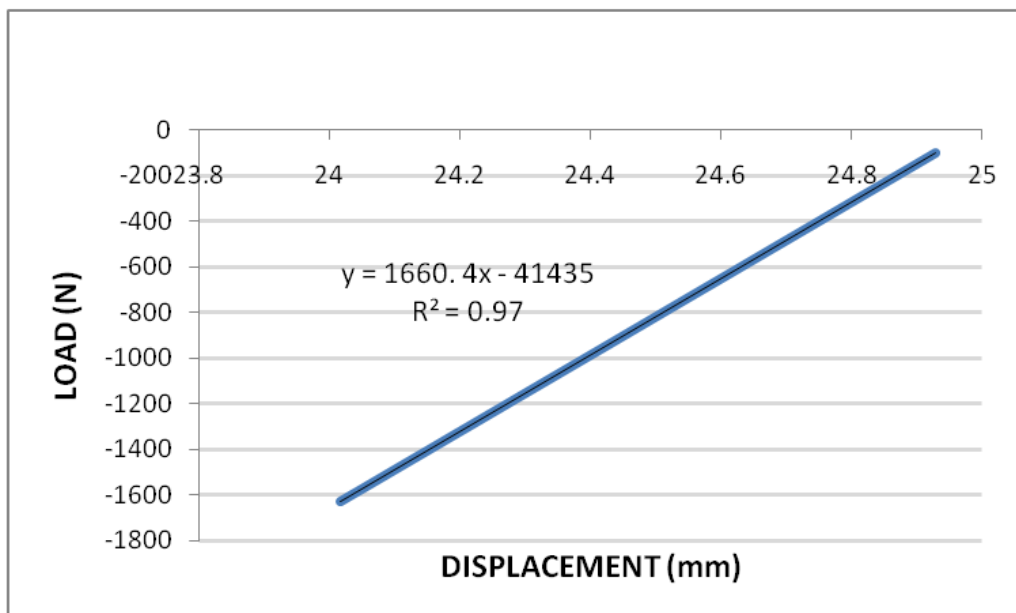
Figure A1-4 Static Stiffness Construct 2 Level II

APPENDIX 2: Dynamic Stiffness Tests

Figure A2-1 to Figure A2-4 showed static stiffness graphs for different constructs. Stiffness for all these specimens were obtained from an average of three tests. The numerical values shown on the axes are based on the Testresources testing machine's coordinate system. The value of R^2 shows the degree of linearity and the equation gives the slope and the intercept of the line. Results indicate that there was a good correlation between experiments and line of best fit.
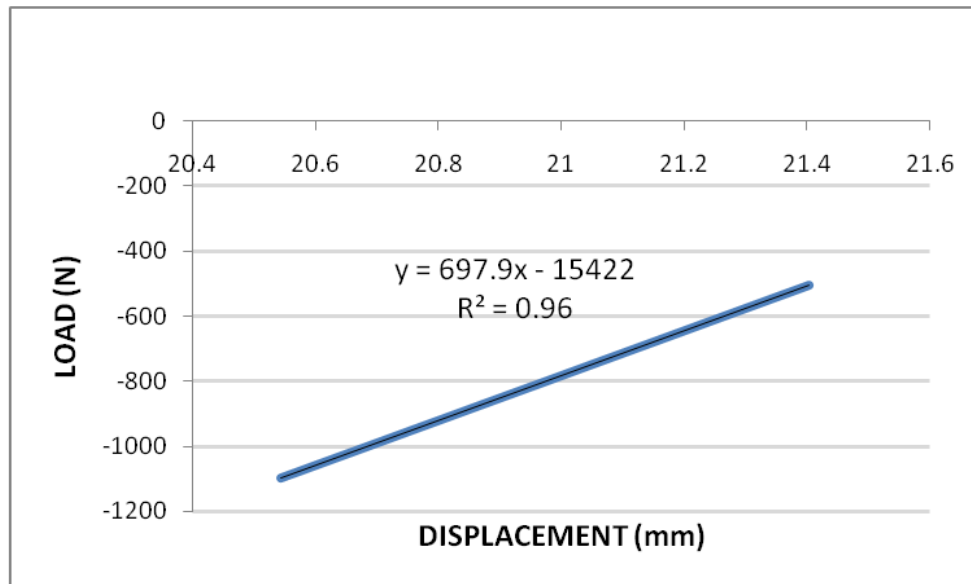
Figure A2-1 Dynamic Stiffness for Construct 1 Level I

The equation shown on the graph:
$$y = 697.9x - 15422$$
$$R^2 = 0.96$$
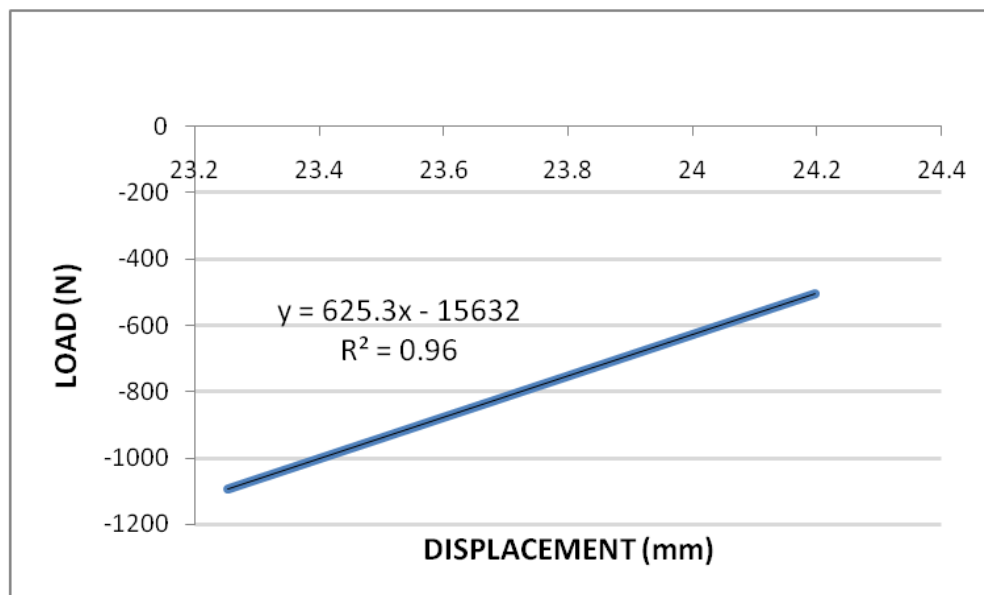
Figure A2-2 Dynamic stiffness Construct 2 Level I

The equation shown on the graph:
$$y = 625.3x - 15632$$
$$R^2 = 0.96$$
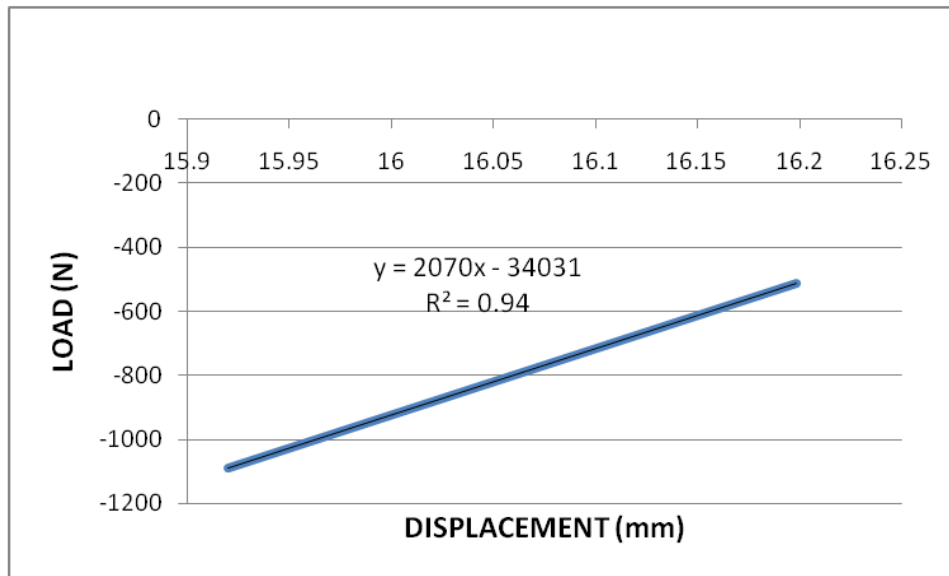
Figure A2-3 Dynamic Stiffness Construct 1 Level II
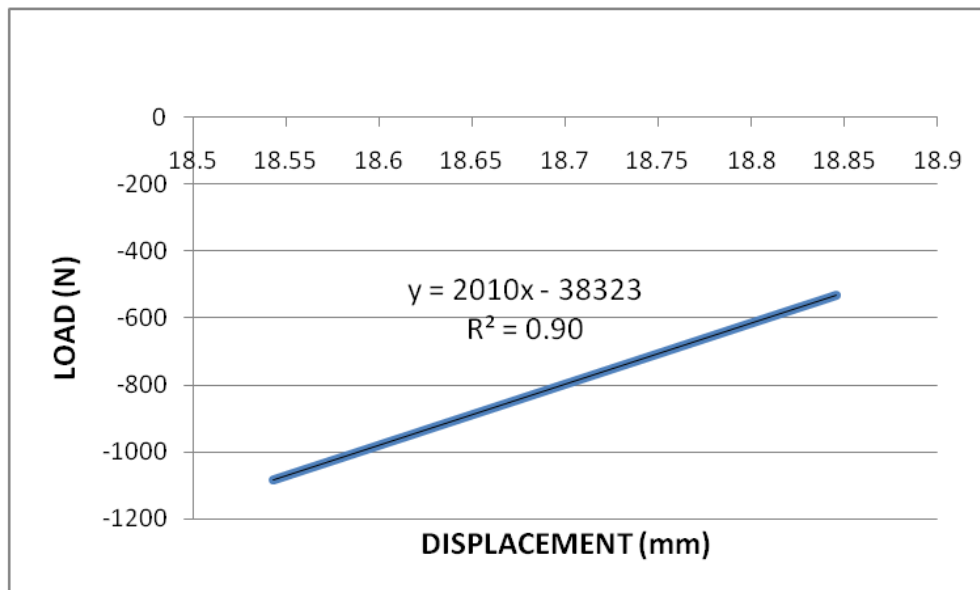
Figure A2-4 Dynamic Stiffness Construct 2 Level II

APPENDIX 3: IR Surface Stresses for Construct 1 and Construct 2

Anterior Surface Stresses

Table A3-1 gives the comparison of surface stresses from IR camera for positions 1 to 5 for Construct 1 and 2. It was observed that the difference between stresses for Construct 1 and 2 was significant with an overall difference of 24.54%.

Stresses from IR Camera (MPa)			
Position	Construct 1 Level I	Construct 2 Level I	% Difference
1	2.72	3.03	11.40
2	1.94	2.49	28.35
3	1.65	2.06	24.85
4	1.02	1.42	39.22
5	2.03	2.92	43.84

Table A3-1 Comparison of Anterior surface stresses from IR camera for Construct 1 and 2

Posterior Surface Stresses

Table A3-2 gives the comparison of surface stresses from IR camera for positions 1 to 5 for Construct 1 and 2. It was observed that the difference between stresses for Construct 1 and 2 was significant with an overall difference of 33.88%.

	Stresses from IR Camera (Mpa)		
Position	Construct 1 Level I	Construct 2 Level I	% Difference
1	2.87	3.29	14.6
2	1.97	2.5	26.9
3	1.64	2.27	38.4
4	0.99	1.55	56.6
5	2.19	2.91	32.9

Table A3-2 Comparison of Posterior surface stresses from IR camera for Construct 1 and 2

Medial Surface Stresses

Error! Reference source not found. gives the comparison of surface stresses from IR camera for positions 1 to 5 for Construct 1 and 2. It was observed that the difference between stresses for Construct 1 and 2 was not significant with an overall difference of -1.02. %.

	Stresses from IR Camera (Mpa)		
Position	Construct 1 Level I	Construct 2 Level I	% Difference
1	-10.57	-11.29	-6.8
2	-4.54	-4.48	1.3
3	-4.17	-4.21	-0.9
4	-3.55	-3.54	0.3
5	-2	-1.98	1.00

Table A3-3 Comparison of Medial surface stresses from IR camera for Construct 1 and 2

Lateral Surface Stresses

Table A3-4 gives the comparison of surface stresses from IR camera for positions 1 to 3 for Construct 1 and 2. It was observed that the difference between stresses for Construct 1 and 2 was not significant with an overall difference of 26.47 %.

	Stress from IR Camera (Mpa)		
Position	Construct 1 Level I	Construct 2 Level I	% Difference
1	2.41	2.52	4.6%
2	0.76	1.01	32.9%
3	2.29	3.25	41.9%

Table A3-4 Comparison of Lateral surface stresses from IR camera for Construct 1 and 2

Bone Plate Surface Stresses

Table A3-4 shows the bar graph for the IR stresses between titanium and carbon/epoxy bone plates. Six positions on the IR stress maps were probed for comparison of surface stresses. It was observed that the overall difference between IR stresses for titanium and carbon/epoxy bone plates was 25.48%

Figure A3-1 Positions probed for titanium and carbon/epoxy plate
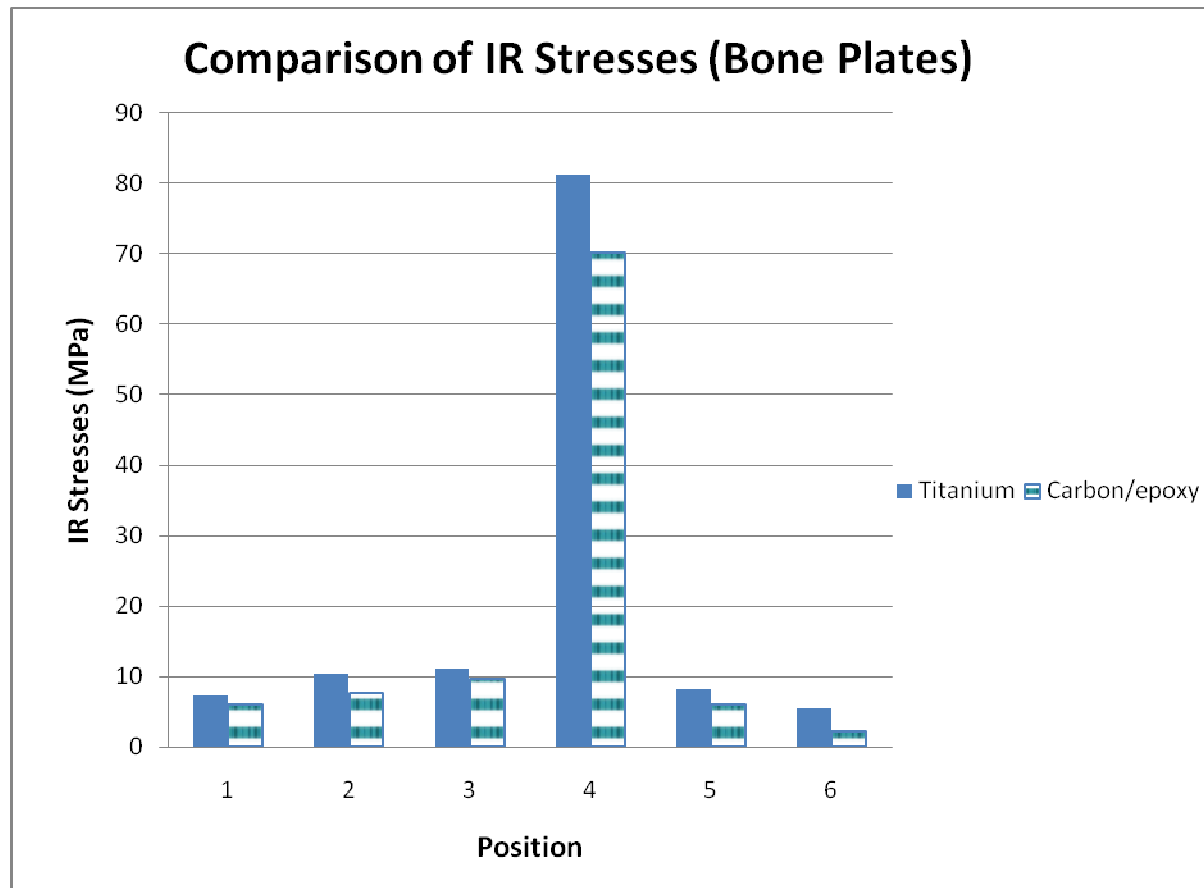
Figure A3-2 Bar Graph for IR Stresses for Construct 1 and Construct 2

APPENDIX 4: FEA Surface Stresses for Construct 1 and Construct 2

Anterior Surface Stresses

Table A4- 1 gives the comparison of FEA surface stresses for positions 1 to 5 for Construct 1 and 2. It was observed that femur of Construct 2 experienced 27.6% more stresses as compared to femur of Construct 1.

Position	Stresses from FEA (MPa)		% Difference
	Construct 1 Level I	Construct 2 Level I	
1	10.555	11.2453	6.5
2	7.4058	9.5903	29.5
3	5.8244	7.1467	22.7
4	3.7749	5.4954	45.6
5	8.3638	11.169	33.5

Table A4- 1 Comparison of Anterior surface stresses from FEA for Construct 1 and 2

Posterior Surface Stresses

Table A4- 2 gives the comparison of FEA surface stresses for positions 1 to 5 for Construct 1 and 2. It was observed that femur of Construct 2 experienced 35.9% more stresses as compared to femur of Construct 1.

Position	Stresses from FEA (Mpa)		% Difference
	Construct 1 Level I	Construct 2 Level I	
1	10.4414	12.5491	20.2
2	7.6426	9.6468	26.2
3	5.8343	8.4194	44.3
4	3.5543	5.6054	57.7
5	8.1712	10.704	31.0

Table A4- 2 Comparison of Anterior surface stresses from FEA for Construct 1 and 2

Table A4-3 FE Axial stiffnesses for Stage 1 to 4 at 3000 N

REFERENCES

[1] US Department of Transportation. Transportation statistics annual report 2010. Available at: www.bts.gov. Accessed June 28, 2012.

[2] American Academy of Orthopaedic Surgeons. Thighbone [Femur) Fracture. 2011; Available at: http://orthoinfo.aaos.org/topic.cfm?topic=A00521. Accessed June 28, 2012.

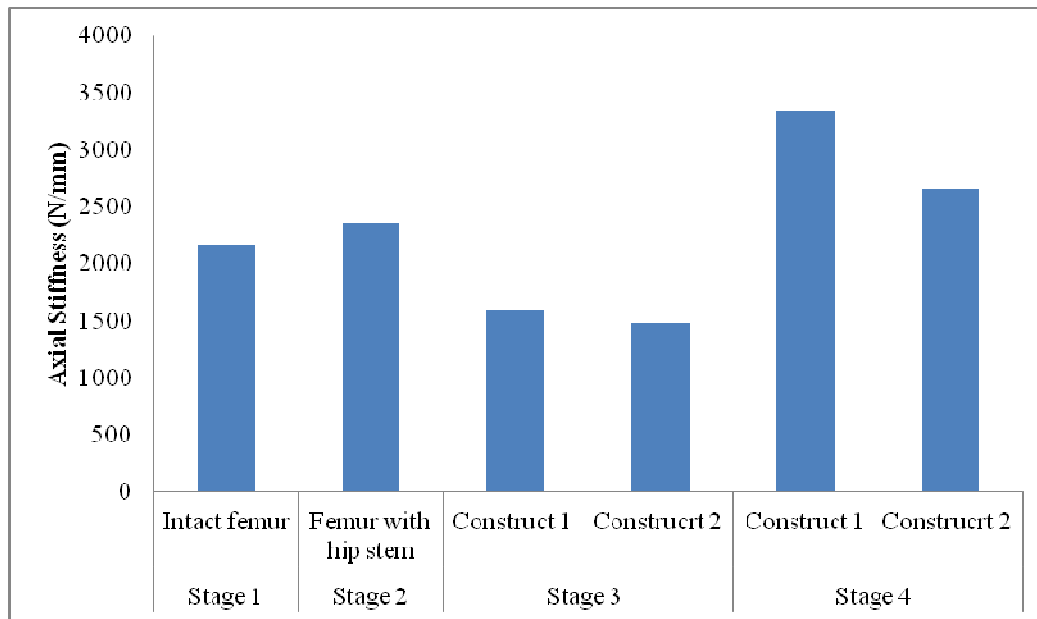[3] The Burden of Musculoskeletal Diseases in the United States: 2008; Available at: http://www.boneandjointburden.org/chapter_downloads/index.htm. Accessed June 28, 2012.

[4] National Osteoporosis Foundation: Available at: http://www.nof.org/. Accessed June 28, 2012.

[5] Canadian Institute for Health Information [CIHI]. 2012; Available at: http://www.cihi.ca/CIHI-ext-portal/internet/EN/TabbedContent/types+of+care/specialized+services/joint+replacements/cihi021 359. Accessed June 28, 2012.

[6] Carr BC, Goswami T. Knee implants – Review of models and biomechanics. Materials and Design, vol. 30, pp. 398-413, 2009.

[7] Scott R, Turner R, Leitzes S, Aufranc O. Femoral fractures in conjunction with total hip replacement. Journal of Bone and Joint Surgery, vol. 57, issue. 4, pp. 494-501, 1975.

[8] Dennis MG, Simon JA, Kummer FJ, Koval KJ, DiCesare PE. Fixation of periprosthetic femoral shaft fractures occurring at the tip of the stem: a biomechanical study of 5 techniques. The Journal of Arthroplasty, vol. 15, Issue 4, 2000.

[9] Ogden WS, Rendall JF. Fractures beneath hip prostheses: a special indication for parham bands and plating. Orthop Trans., vol.70, issue. 2, 1978.

[10] Thakur AJ. The Elements of Fracture Fixation, 2nd edition. New Delhi: Reed Elsevier India Private Limited 2007.

[11] American Academy of Orthopaedic Surgeons. Pediatric Thighbone (Femur) Fracture. 2011; Available at: http://orthoinfo.aaos.org/topic.cfm?topic=A00424. Accessed June 28, 2012.

[12] Ramakrishna S, Mayer J, Huang ZM. An Introduction to Biocomposites, Series on Biomaterials and Bioengineering – London: Imperial College Press, vol. 1, 2004.

[13] American Academy of Orthopaedic Surgeons. Total Knee Replacement. 2012; Available at: http://orthoinfo.aaos.org/topic.cfm?topic=A00389. Accessed June 28, 2012.

[14] Hayes WC, Snyder B. Towards a quantitative formulation of Wolff's law in trabecular bone, in "Mechanical Properties of Bone". The Joint ASME-ASCE Applied Mechanics, Fluids Engineering and Bioengineering Conference. Colorado: AMD, vol. 45, 1981.

[15] Wikipedia: The Free Encyclopedia. Osteoporosis. 2012; Available at: http://en.wikipedia.org/wiki/Osteoporosis. Accessed June 28, 2012.

[16] Cheng JCY, Tse PYT, Chow YYN. The place of the dynamic compression plate in femoral shaft fractures. Injury, vol. 16, pp. 529-534, 1985.

[17] Lewandowska–Szumieł M, Komender J, Chłopek J. Interaction between carbon composites and bone after intrabone implantation. Journal of Biomedical Materials Research, vol. 48, pp. 289-296, 1999.

[18] Reddy JN, Chao WC. Finite-element analysis of laminated bimodulus composite-material plates. Computers and Structures, vol. 12, pp. 245-251, 1980.

[19] Cheal EJ, Spector M, Hayes WC. Role of loads and prosthesis material properties on the mechanics of the proximal femur after total hip arthroplasty. Journal of Orthopaedic Research, vol. 10, pp. 405-422, 1992.

[20] Cheung G, Zalzal P, Bhandari M, Spelt JK, Papini M. Finite element analysis of a femoral retrograde intramedullary nail subject to gait loading. Medical Engineering and Physics, vol. 26, pp. 93-108, 2004.

[21] McNamara BP, Cristofolini L, Toni A, Taylor D. Relationship between bone-prosthesis bonding and load transfer in total hip reconstruction. Journal of Biomechanics, vol. 30, pp. 621-630, 1997.

[22] Taylor ME, Tanner KE, Freeman MAR, Yettram AL. Stress and strain distribution within the intact femur: compression or bending?. Medical Engineering and Physics, vol. 18, pp. 122-131, 1996.

[23] Wang CJ, Brown CJ, Yettram AL, Procter P. Intramedullary femoral nails: one or two lag screws? A preliminary study. Medical Engineering and Physics, vol. 22, pp. 613-624, 2000.

[24] Wang CJ, Yettram AL, Yao MS, Procter P. Finite element analysis of a Gamma nail within a fractured femur. Medical Engineering and Physics, vol. 20, pp. 677-683, 1998.

[25] University of Minnesota. "Anatomy Tutorial - Anatomic Positions, Atlas of Human Cardiac Anatomy, Regents of the University of Minnesota. 2010; Available at: http://www.vhlab.umn.edu/atlas/anatutorial/anatutorial1.shtml. Accessed June 28, 2012.

[26] Wikiversity. Anatomical terminology. 2012; Available at: http://en.wikiversity.org/wiki/Anatomical_terminology. Accessed June 28, 2012.

[27] Wikipedia. Femur. 2012; Available at: http://en.wikipedia.org/wiki/Femur. Accessed June 28, 2012.

[28] Encyclopaedia Britannica I. Human evolution. 2012; Available at:
http://www.britannica.com/EBchecked/topic/275670/human-evolution. Accessed June 28, 2012.

[29] Sawchuk and Padiak. Femur labels, Anthropology: the University of Toronto at Scarborough.
2004; Available at: http://reel.utsc.utoronto.ca/mboyer/Sawchuk/images/bones_LOWres/.
Accessed 28, 2012.

[30] Wikipedia: The Free Encyclopedia. Bone. 2012; Available at:
http://en.wikipedia.org/wiki/Bone. Accessed June 28, 2012.

[31] Greenwald AS, Haynes DW. Weight-bearing areas in the human hip joint. The Journal of
bone and joint surgery, vol. 54, issue. 1, pp. 157-163, 1972.

[32] Kempson GE, Spivey CJ, Swanson SAV, Freeman MAR. Patterns of cartilage stiffness on
normal and degenerate human femoral heads. Journal of Biomechanics, vol. 4, issue. 6, pp. 597-
608, 1971.

[33] Robert EK. Hip and Knee Surgery: A Patient's Guide to Hip Replacement, Hip Resurfacing,
Knee Replacement, & Knee Arthroscopy: Oxford University Press. 2008

[34] Wikipedia: The Free Encyclopedia. Hip. 2012; Available at:
http://en.wikipedia.org/wiki/Hip_(anatomy). Accessed June 28, 2012.

[35] Advanced Technology Hip Surgery. Total Hip Replacement Surgery 2003; Available at:
http://www.hipsurgery.co.il/english/introduction.htm. Accessed June 28, 2012.

[36] Huiskes R, Weinans H, Grootenboer HJ, Dalstra M, Fudala B, Slooff TJ. Adaptive bone-
remodeling theory applied to prosthetic-design analysis. Journal of Biomechanics, vol. 20, pp.
1135-1150, 1987.

[37] American Academy of Orthopaedic Surgeons. Knee Implants. 2010; Available at:
http://orthoinfo.aaos.org/topic.cfm?topic=A00221. Accessed June 28, 2012.

[38] ACL Solutions. Anatomy of the Knee. 2011; Available at:
http://www.aclsolutions.com/anatomy.php. Accessed June 28, 2012.

[39] Wikipedia: The Free Encyclopedia. Gait (human). 2012; Available at:
http://en.wikipedia.org/wiki/Gait_(human). Accessed June 28, 2012.

[40] Gary EW, and Gary LB. Encyclopedia of Biomaterials and Biomedical Engineering, Informa
Healthcare USA Inc., pp. 3110, 2008

[41] Seedhom BB, Wallbridge NC. Walking activities and wear of prostheses. Annals of the
Rheumatic Diseases, vol. 44, pp. 838-843, 1985.

[42] Nordin M, Frankel V. Basic biomechanics of the musculoskeletal system, 3rd ed., Lippincott Williams and Wilkins, Philadelphia, 2001.

[43] Motion Ranges of Hip Joint. Available at: http://people.emich.edu/pbogle/PHED_200/overheads/ch7_art/07_39.jpg. Accessed June 28, 2012.

[44] Dave Thompson's lecture notes. Conventions for naming parts of the gait cycle," University of Oklahoma Health Sciences Centre. 2002; Available at: http://moon.ouhsc.edu/dthompso/gait/terms.htm. Accessed June 28, 2012.

[45] Cullinance DM. Biomechanics of Bone, Principles of Bone Biology, 2nd edition, San Diego: Academic Press, vol. 1, pp. 17-32, 2002

[46] Sanders R. Trauma; Core Knowledge in Orthopedics. Scitech Book News Inc., 2008.

[47] Cooke PH, Newman JH. Fractures of the femur in relation to cemented hip prostheses. Journal of Bone and Joint Surgery (Br.), vol. 70-B, pp. 386-389, 1988.

[48] Serocki JH, Chandler RW, Dorr LD. Treatment of fractures about hip prostheses with compression plating. The Journal of Arthroplasty, vol. 7, pp. 129-135, 1992.

[49] Somers JF, Suy R, Stuyck J, Mulier M, Fabry G. Conservative treatment of femoral shaft fractures in patients with total hip arthroplasty. The Journal of Arthroplasty, vol. 13, pp. 162-171, 1998.

[50] Elstrom J, Virkus W, Pankovich A. Fractures of the Femoral Shaft, Handbook of Fractures, 3rd edition. New York, McGraw-Hill, Ch. 19, p293-303, 2006.

[51] Carter DR, Spengler DM. Biomechanics of fracture, Bone in clinical orthopedics, 2nd edition. New York: AO Publishing, Ch. 8, p261-285, 2002.

[52] Uhthoff HK, Poitras P, Backman DS. Internal plate fixation of fractures: short history and recent developments. Journal of Orthopaedic Science, vol. 11, issue 2, pp. 118-126, 2006.

[53] RadDaily.com. Orthopedic Hardware: Basic Components, 2012; Available at: http://www.raddaily.com/whitepaperarticle.php?articleTitle=Orthopedic+Hardware. Accessed June 28, 2012.

[54] Woo SL, Akeson W H, Coutts RD, Rutherford L, Doty D, Jemmott GF, Amiel D. A comparison of cortical bone atrophy secondary to fixation with plates of larger differences in bending stiffness. Journal of Bone and Joint Surgery, vol. 58, issue. 2, pp. 190-195, 1976.

[55] Beaupre G S, Carter DR, Orr TE, Csongradi J. Stresses in plated long-bones: the role of screw tightness and interface slipping, Journal of Orthpaedic Research, vol. 6, issue. 1, pp. 39-50, 1988.

[56] Saidpour SH, 2006. Assessment of carbon fibre composite fracture fixation plate using finite element analysis. Annals of Biomedical Engineering, vol. 34, pp. 1157-1163, 2006.

[57] Fan F, Xiu K, Duan H, Zhang M. Biomechanics and histological evaluation of the application of biodegradable poly-L-lactic cushion to the plate internal fixation for bone fracture healing. Clinical Biomechanics, vol. 23, supplement 1, pp. S7-S16, 2008.

[58] MatWeb MPD. Cobalt, Co. 2012; Available at: http://www.matweb.com/search/DataSheet.aspx?MatGUID=4602449fc566494ab3efa286e8827c99&ckck=1. Accessed June 28, 2012.

[59] MatWeb MPD. Titanium, Ti. 2012; Available at: http://www.matweb.com/search/DataSheet.aspx?MatGUID=66a15d609a3f4c829cb6ad08f0dafc01&ckck=1. Accessed June 28, 2012.

[60] MatWeb MPD. Overview of materials for Stainless Steel. 2012; Available at: http://www.matweb.com/search/DataSheet.aspx?MatGUID=71396e57ff5940b791ece120e4d563e0. Accessed June 28, 2012.

[61] Zdero R, McConnell AJ, Peskun C, Syed KA, Schemitsch EH. Biomechanical measurements of torsion-tension coupling in human cadaveric femurs. Journal of Biomechanical Engineering, vol. 133, issue. 1, 2011.

[62] Papini M, Zdero R, Schemitsch EH, Zalzal P. The biomechanics of human femurs in axial and torsional loading: comparison of finite element analysis, human cadaveric femurs, and synthetic femurs. Journal of Biomechanical Engineering, vol. 129, issue. 1, pp. 12-19, 2007.

[63] McConnell AJ, Zdero R, Syed KA, Peskun C, Schemitsch EH. The biomechanics of ipsilateral intertrochanteric and femoral shaft fractures: A comparison of 5 fracture fixation techniques. Journal of Orthopaedic Trauma, vol. 22, issue. 8, pp. 517-524, 2008.

[64] Zdero R, McConnell AJ, Peskun C, Syed KA, Schemitsch EH. Biomechanical measurements of torsion-tension coupling in human cadaveric femurs. Journal of Biomechanical Engineering, vol. 133, issue. 1, 2011.

[65] Zdero R, Shah S, Mosli M, Schemitsch EH. The effect of load application rate on the biomechanics of synthetic femurs. Proceedings of the Institution of Mechanical Engineers.Part H, Journal of Engineering in Medicine, vol. 224, issue. 4, pp. 599-605, 2010.

[66] Zdero R, Olsen M, Bougherara H, Schemitsch EH. Cancellous bone screw purchase: a comparison of synthetic femurs, human femurs, and finite element analysis. Proceedings of the Institution of Mechanical Engineers.Part H, Journal of Engineering in Medicine, vol. 222, issue. 8, pp. 1175-1183, 2008.

[67] Zdero R, Shah S, Mosli M, Bougherara H, Schemitsch EH. The effect of the screw pull-out rate on cortical screw purchase in unreamed and reamed synthetic long bones. Proceedings of the

Institution of Mechanical Engineers. Part H, Journal of Engineering in Medicine, vol. 224, pp. 503-513, 2010.

[68] Zdero R, Elfallah K, Olsen M, Schemitsch EH. Cortical screw purchase in synthetic and human femurs. Journal of Biomechanical Engineering, vol. 131, issue. 9, pp. 94503-94510, 2009.

[69] Cristofolini L, Viceconti M, Cappello A, Toni A. Mechanical validation of whole bone composite femur models. Journal of Biomechanics, vol. 29, pp. 525-535, 1996.

[70] Cristofolini L, Viceconti M. Mechanical validation of whole bone composite tibia models. Journal of Biomechanics, vol. 33, pp. 279-288, 2000.

[71] Davis ET, Olsen M, Zdero R, Papini M, Waddell JP, Schemitsch EH. A biomechanical and finite element analysis of femoral neck notching during hip resurfacing. Journal of Biomechanical Engineering; vol. 131, issue. 4, 2009.

[72] Martens M, van Audekercke R, de Meester P, Mulier JC. The mechanical characteristics of the long bones of the lower extremity in torsional loading. Journal of Biomechanics, vol. 13, pp. 667-676, 1980.

[73] Cristofolini L, Viceconti M. Development and validation of a technique for strain measurement inside polymethyl methacrylate. The Journal of Strain Analysis for Engineering Design, vol. 35, pp. 21-33, 2000.

[74] Martens M, Van Audekercke R, Delport P, De Meester P, Mulier JC. The mechanical characteristics of cancellous bone at the upper femoral region. Journal of Biomechanics, vol. 16, pp. 971-983, 1983.

[75] Bougherara H, Zdero R, Miric M, Shah S, Hardisty M, Zalzal P, Schemitsch EH. The biomechanics of the T2 femoral nailing system: a comparison of synthetic femurs with finite element analysis. Proceedings of the Institution of Mechanical Engineers, Part H: Journal of Engineering in Medicine, vol. 223, issue. 3, pp. 303-314, 2009.

[76] Bougherara H, Zdero R, Shah S, Niric M, Papini M, Zalzal P, Schemitsch EH. A biomechanical assessment of modular and monoblock revision hip implants using FE analysis and strain gage measurements, Journal of Orthopaedic Surgery and Research, vol. 5, issue. 1, 2010.

[77] Cristofolini L, Juszczyk M, Taddei F, Viceconti M. Strain distribution in the proximal human femoral metaphysis. Proceedings of the Institution of Mechanical Engineers.Part H, Journal of Engineering in Medicine, vol. 223, pp. 273-288, 2009.

[78] Brekelmans WAM, Poort HW, Slooff TJJH. A New Method to Analyse the Mechanical Behaviour of Skeletal Parts. Acta Orthopaedica, vol. 43, pp. 301-317, 1972.

[79] Cheal EJ, Hayes WC, Lee CH, Snyder BD, Miller J. Stress analysis of a condylar knee tibial component: influence of metaphyseal shell properties and cement injection depth. Journal of

Orthopaedic Research : official publication of the Orthopaedic Research Society, vol. 3, pp. 424-434, 1985.

[80] Cheal EJ, Hayes WC, White AA, Perren SM. Stress analysis of a simplified compression plate fixation system for fractured bones. Computers and Structures, vol. 17, pp. 845-855, 1983.

[81] Huiskes R, Chao EY. A survey of finite element analysis in orthopedic biomechanics: the first decade. Journal of Biomechanics, vol. 16, pp. 385-409, 1983.

[82] Cheung G, Zalzal P, Bhandari M, Spelt JK, Papini M. Finite element analysis of a femoral retrograde intramedullary nail subject to gait loading. Medical Engineering and Physics, vol. 26, pp. 93-108, 2004.

[83] Taylor ME. Finite element analysis of the resurfaced femoral head. Proceedings of the Institution of Mechanical Engineers. Part H, Journal of Engineering in Medicine, vol. 220, pp. 289-297, 2006.

[84] Taylor ME, Tanner KE, Freeman MA, Yettram AL. Stress and strain distribution within the intact femur: compression or bending?. Medical Engineering & Physics, vol. 18, pp. 122-131, 1996.

[85] van Rietbergen B, Weinans H, Huiskes R, Odgaard A. A new method to determine trabecular bone elastic properties and loading using micromechanical finite-element models. Journal of Biomechanics, vol. 28, pp. 69-81, 1995.

[86] Bougherara H, Zdero R, Miric M, Shah S, Hardisty M, Zalzal P, Schemitsch EH. The biomechanics of the T2 femoral nailing system: a comparison of synthetic femurs with finite element analysis. Proceedings of the Institution of Mechanical Engineers, Part H: Journal of Engineering in Medicine, vol. 223, pp. 303-314, 2009.

[87] Bougherara H, Zdero R, Mahboob Z, Dubov A, Shah S, Schemitsch EH. The biomechanics of a validated finite element model of stress shielding in a novel hybrid total knee replacement. Proceedings of the Institution of Mechanical Engineers. Part H, Journal of Engineering in Medicine, vol. 224, pp. 1209-1219, 2010.

[88] Chen YS, Hung YY, Ng SP, Huang YH, Liu L. Review and comparison of shearography and active thermography for nondestructive evaluation." Materials Science and Engineering R: Reports, vol. 64, issue. 5-6, pp. 73-112, 2009.

[89] Bremond P. Lock-in themography, a tool for NDE and online NDT control in the aircraft industry: Benefits of new Technologies Testing, Expo, Hamburg, 2005.

[90] Biot MA. Thermoelasticity and Irreversible Thermodynamics. Journal of Applied Physics, vol. 27, pp. 240-253, 1956.

[91] Ghosh KK, Karbhari VM. A critical review of infrared thermography as a method for non-destructive evaluation of FRP rehabilitated structures. International Journal of Materials and Product Technology, vol. 25, pp. 241-241, 2006.

[92] Liu J, Dai J, Wang Y. Research on lock in thermography for aerospace materials of nondestructive test based on image sequence processing. Proceedings of SPIE - The International Society for Optical Engineering, vol. 7375, 2009.

[93] McLaughlin PV, McAssey EV, Deitrich RC. Non-destructive examination of fibre composite structures by thermal field techniques. NDT and E International, vol. 13, pp. 56-62, 1980.

[94] Titman DJ. Applications of thermography in non-destructive testing of structures. NDT and E International, vol. 34, pp. 149-154, 2001.

[95] McLaughlin, P.V. Jr. Defect detection and quantification in laminated composites by EATF (Passive) thermography. Review of Progress in Quantitative Nondestructive Evaluation, Williamsburg, Virginia (United States), vol. 7B, pp. 1125-1132, 1987.

[96] Ball RJ, Almond DP. The detection and measurement of impact damage in thick carbon fibre reinforced laminates by transient thermography. NDT and E International, vol. 31, issue. 3, pp. 165-173, 1998.

[97] Wang Z, Liu J, Dai J. Lock-in thermography for evaluation of destruction area and determination of depth. Proceedings of SPIE - The International Society for Optical Engineering, vol. 6723, pp. 67231F, 2007.

[98] Bai W, Wong BS. Evaluation of defects in composite plates under convective environments using lock-in thermography. Measurement Science and Technology, vol. 12 142, 2001.

[99] Ibarra-Castanedo C, Piau J-, Guilbert S, Avdelidis N, Genest M, Bendada A, Maldague XPV. Comparative study of active thermography techniques for the nondestructive evaluation of honeycomb structures. Research in Nondestructive Evaluation, vol. 20, issue. 1, 2009.

[100] Maldague XPV, Springer-Verlag. Nondestructive evaluation of materials by infrared thermography, Springer-Verlag, 207 pages, 1993.

[101] Maldague XPV, Marinetti S. Pulse phase infrared thermography. Journal of Applied Physics, vol. 79, issue. 5, 2694, 1996.

[102] Bai W, Wong BS. Non-destructive Evaluation of Aircraft Structure Using Lock-in Thermography. Nondestructive Evaluation of Aging Aircraft, Airports, and Aerospace Hardware IV, vol. 3994, pp. 37-46, 2000.

[103] Bergmann G, Deuretzbacher G, Heller M, Graichen F, Rohlmann A, Strauss J, Duda GN. Hip contact forces and gait patterns from routine activities. Journal of Biomechanics, vol. 34, issue. 7, pp. 859-871, 2001.

[104] Bergmann G, Graichen F, Rohlmann A. Hip joint loading during walking and running, measured in two patients. Journal of Biomechanics, vol. 26, issue. 8, pp. 969-990, 1993.

[105] Pacific Research Laboratories Inc. Large left fourth generation femur. 2012; Available at: http://www.sawbones.com. Accessed June 28, 2012.

[106] Robinson AF, Dulieu-Barton JM, Quinn S, Burguete RL. Paint coating characterization for thermoelastic stress analysis of metallic materials. Measurement Science and Technology, vol. 21, issue. 8, pp. 5502-5512, 2010.

[107] Jennings J., Kirkpatrick L., Mukherjee A. Cable-Ready Cable Grip System Bone Plate. Michigan, USA: Pioneer Laboratories 1997.

[108] Zimmer® Inc. Cable-Ready® Bone Plate: Abbreviated Surgical Technique, USA. 2010; Available at: http://www.zimmer.co.uk/web/enus/pdf/cable_ready_bone_plate_abbreviated_surgical_technique. pdf. Accessed June 28, 2012

[109] Flow-Stone Anchoring Cement. Available at: http://consumer.kpmindustries.com/documents/FlowStone.pdf. Accessed June 28, 2012.

[110] Stryker Inc. U. Stryker Howmedica Osteonics. "Exeter; total hip system," [Product brochure], 2001

[111] Davy DT, Kotzar GM, Brown RH, Heiple KG, Goldberg VM, Heiple J,K G., Berilla J, Burstein AH. Telemetric force measurements across the hip after total arthroplasty. The Journal of Bone and Joint Surgery, vol. 70, issue. 1, pp. 45-50, 1988.

[112] Bremond P. New developments in thermoelastic stress analysis by infrared thermography, IV Conferencia Panamericana De END, Buenos Aires, 2007.

[113] Dulieu-Barton JM, Quinn S, Eyre C, Cunningham PR. Development of a temperature calibration device for thermoelastic stress analysis. Advances in Experimental Mechanics, vol. 1-2, pp. 197-204, 2004.

[114] Hyodo K, Inomoto M, Ma WW, Miyakawa S, Tateishi T, Wada H. Thermoelastic femoral stress imaging for experimental evaluation of hip prosthesis design., JSMEC, vol. 44, issue. 4, pp. 1065-1071, 2001.

[115] Vanderby Jr. R, Kohles SS. Thermographic stress analysis in cortical bone, Journal of Biomechanical Engineering, vol. 113, issue. 4, pp. 418-422, 1991.

[116] Altair LI Software. Available at: http://www.flir.com/uploadedFiles/Thermography/Products/Software_and_Accessaries/FlirAltairL I_LR_09.08.pdf. Accessed June 28, 2012.

[117] Gupta R, Breitenstein O. Unsteady-state lock-in thermography - applications to shunts in solar cells. QIRT Journal, vol. 4, issue. 1, pp. 85-105, 2007.

[118] MatWeb MPD. AISI Type 316L Stainless Steel. 2012; Available at: http://www.matweb.com/search/DataSheet.aspx?MatGUID=1336be6d0c594b55afb5ca8bf1f3e042. Accessed June 28, 2012.

[119] Varano R. Structure-property investigation of Co-Cr-Mo alloys used in metal-metal total hip replacements 1998

[120] Carpenter Technology Corporation. Technical Datasheet: BioDur® CCM Plus® (Micro-Melt®) Alloy. 2012; Available at: http://cartech.ides.com/datasheet.aspx?I=101&TAB=DV_DS&E=9&SKEY=101.7.2974071%3Ad3357c12-f9a3-4c94-86f2-e9c3d9b5fb7b&CULTURE=en-US. Accessed June 28, 2012.

[121] Medley JB, Krygier JJ, Bobyn JD, Chan FW, Lippincott A, Tanzer M. Kinematics of the MATCO hip simulator and issues related to wear testing of metal-metal implants. Proceedings of the Institution of Mechanical Engineers.Part H, Journal of Engineering in Medicine vol. 211, pp. 89-99, 1997.

[122] Material Property Database. "Material: PMMA," Massachusetts Institute of Technology, Available at: http://www.mit.edu/~6.777/matprops/pmma.htm. Accessed June 28, 2012.

[123] MATBASE. Data Table For: Polymers: Commodity Polymers: PMMA. 2009; Available at: http://www.matbase.com/material/polymers/commodity/pmma/properties. Accessed June 28, 2012.

[124] ANSYS INC. Element Release 12.0, SOLID187: 3-D 10-Node Tetrahedral Structural Solid. 2009; Available at: http://www1.ansys.com/customer/content/documentation/120/ans_elem.pdf. Accessed June 28, 2012.

[125] ANSYS Release 11.0, Documentation for ANSYS, SHELL 4-Node Finite Strain Shell. Available at: http://www.kxcad.net/ansys/ANSYS/ansyshelp/Hlp_E_SHELL181.html. Accessed June 28, 2012

[126] ANSYS INC. Element Release 12.0, CONTA174 Element Description. 2009; Available at: http://www1.ansys.com/customer/content/documentation/120/ans_elem.pdf. Accessed June 28, 2012.

[127] Cheal EJ, Hayes WC, White AA, Perren SM. Stress analysis of compression plate fixation and its effects on long bone remodeling. Journal of Biomechanics, vol. 18, pp. 141-150, 1985.

[128] Dubov A, Kim SYR, Shah S, Schemitsch EH, Zdero R, Bougherara H. The biomechanics of plate repair of periprosthetic femur fractures near the tip of a total hip implant: the effect of cable-screw position. Proceedings of the Institution of Mechanical Engineers.Part H, Journal of Engineering in Medicine, vol. 225, pp. 857-865, 2011.

[129] Schemitsch EH, Kim SYR, Dubov A, Bougherara H, Zdero R, Shah S. The biomechanics of plate fixation of periprosthetic femoral fractures near the tip of a total hip implant: cables, screws, or both?. Proceedings of the Institution of Mechanical Engineers, Part H: Journal of Engineering in Medicine, vol. 225, pp. 845-856, 2011.

[130] Mihalko WM, Beaudoin AJ, Cardea JA, Krause WR. Finite-element modelling of femoral shaft fracture fixation techniques post total hip arthroplasty. Journal of Biomechanics, vol. 25, pp. 469-476, 1992.

[131] Zdero R, Walker R, Waddell JP, Schemitsch EH. Biomechanical evaluation of periprosthetic femoral fracture fixation. Journal of Bone and Joint Surgery, vol. 90, issue. 5, pp. 1068-1077, 2008.

[132] Talbot M, Zdero R, Schemitsch EH. Cyclic loading of periprosthetic fracture fixation constructs. Journal of Trauma, vol. 64, issue. 5, pp. 1308-1312, 2008.

[133] Talbot M, Zdero R, Garneau D, Cole PA, Schemitsch EH. Fixation of long bone segmental defects: A biomechanical study. Injury, vol. 39, issue. 2, pp. 181-186, 2008.

[134] Heiner AD, Brown TD. Structural properties of a new design of composite replicate femurs and tibias. Journal of Biomechanics, vol. 21, pp. 773-781, 2001.

[135] Paul JP. Forces transmitted by joints in the human body. Proc Inst Mech Eng Part H: Journal of Engineering Medicine, vol. 181, issue. 3 J, pp. 8-15, 1967.

[136] Crowninshield RD, Johnston RC, Andrews JG, Brand RA. A biomechanical investigation of the human hip. Journal of Biomechanics, vol. 11, issue. 1-2, pp. 75-85, 1978.

[137] Dennis MG, Simon JA, Kummer FJ, Koval KJ, Di Cesare PE. Fixation of periprosthetic femoral shaft fractures: A biomechanical comparison of two techniques. Journal of Orthopaedic Trauma, vol. 15, issue. 3, pp. 177-180, 2001.

[138] Gardner MP, Chong ACM, Pollock AG, Wooley PH. Mechanical evaluation of large-size fourth-generation composite femur and tibia models. Annals of Biomedical Engineering, vol. 38, issue. 3, pp. 613-620, 2010.

[139] Shah S, Bougherara H, Schemitsch EH, Zdero R. Biomechanical stress maps of an artificial femur obtained using a new infrared thermography technique validated by strain gages. Medical Engineering and Physics, 2012.

[140] Larsson S, Elloy M, Hansson L. Fixation of trochanteric hip fractures. A cadaver study of static and dynamic loading. Acta Orthop Scand, vol. 58, issue. 4, pp. 365-368, 1987.

[141] Bougherara H, Bureau MN, Yahia L. Bone remodeling in a new biomimetic polymer-composite hip stem. Journal of Biomedical Materials Research Part A, vol. 92, issue. 1, pp. 164-174, 2010.

[142] Lengsfeld M, Burchard R, Günther D, Pressel T, Schmitt J, Leppek R, Griss P. Femoral strain changes after total hip arthroplasty — patient-specific finite element analyses 12 years after operation. Medical Engineering and Physics, vol. 27, pp. 649-654, 2005.

[143] Bethea JS 3rd, DeAndrade JR, Fleming LL, Lindenbaum SD, Welch RB. Proximal femoral fractures following total hip arthroplasty. Clinical Orthopaedics and Related. Research., vol. 170, pp. 95-106, 1982.

[144] Beals RK, Tower SS. Periprosthetic fractures of the femur. Analysis of 93 fractures. Clinical Orthopaedics and Related. Research, vol. 327, pp. 238-246, 1996.

[145] Zenni EJ Jr., Pomeroy DL, Caudle RJ. Ogden plate and other fixations for fractures complicating femoral endoprostheses. Clinical Orthopaedics and Related. Research, vol 231, pp. 83-90, 1988.

[146] Bougherara H, Rahim E, Shah S, Dubov A, Schemitsch EH, Zdero R. A preliminary biomechanical assessment of a polymer composite hip implant using an infrared thermography technique validated by strain gage measurements. Journal of Biomechanical Engineering, vol. 133, issue. 7, 074503, 2011.

[147] Zdero R, Bougherara H. Orthopaedic biomechanics: A practical approach to combining mechanical testing and finite element analysis, Chapter 7 in Finite Element Analysis, D. Moratal., Intech Education and Publishing, Vienna, 2010.

[148] Akay M, and Aslan N. Numerical and Experimental Stress Analysis of a Polymeric Composite Hip Joint Prosthesis, Journal of Biomedical Materials Research, vol. 31, pp. 167-182, 1996.

[149] Bougherara H, Klika V, Marisik F, Bureau MN, and Yahia LH. Design of a Biomimetic Polymer-Composite Hip Prosthesis, Journal of Biomedical Materials Research, Part A, vol. 82, no. 1, pp. 27–40, 2007.

[150] Gdoutos EE, Raftopoulos DD, Baril JD. A critical review of the biomechanical stress analysis of the human femur, Biomaterials, vol. 3, issue. 1, pp. 2-8, 1982.

[151] Cristofolini L, Cappello A,Toni A. Experimental errors in the application of photoelastic coatings on human femurs with uncemented hip stems, Strain, vol. 30, issue. 3, pp. 95-102, 1994.

[152] Sawbones, Vashon, WA, USA, . 2012; Available at: www.sawbones.com/catalog/pdf/us_catalog.pdf. Accessed June 28, 2012.

[153] Zdero R, Rose S, Schemitsch EH, Papini M. Cortical screw pullout strength and effective shear stress in synthetic third generation composite femurs. Journal of Biomechanical Engineering, vol 129; no. 2, pp. 289-293 2007.

[154] Nicayenzi B, Shah S, Schemitsch EH, Bougherara H, Zdero R. The biomechanical effect of changes in cancellous bone density on synthetic femur behaviour. Proceedings of the Institution of Mechanical Engineers.Part H, Journal of Engineering in Medicine, vol. 225, pp. 1050-1060, 2011.

[155] Davis ET, Olsen M, Zdero R, Waddell JP, Schemitsch EH. Femoral neck fracture following hip resurfacing: The effect of alignment of the femoral component. J Bone Joint Surg Br, vol. 90, issue. 11, pp. 1522-1527, 2008.

[156] Welk GJ, Differding JA, Thompson RW, Blair SN, Dziura J, Hart P. The utility of the Digi-Walker step counter to assess daily physical activity patterns. Medicine and Science in Sports and Exercise, vol. 32, issue. 9 SUPPL., pp. S481-S488, 2000.

[157] Edwards WB, Taylor D, Rudolphi TJ, Gillette JC, Derrick TR. Effects of stride length and running mileage on a probabilistic stress fracture model. Medicine and Science in Sports and Exercise, vol. 41, issue. 12, pp. 2177-2184, 2009.